Interlayer Charge Transfer in van der Waals Heterostructures Formed by Transition Metal Dichalcogenide Monolayers

By

Frank Ceballos

Submitted to the graduate degree program in the Department of Physics and Astronomy and the Graduate Faculty of the University of Kansas
in partial fulfillment of the requirements for the degree of
Doctor of Philosophy.

Committee members

Dr. Hui Zhao, Chairperson

Dr. Siyuan Han

Dr. Judy Wu

Dr. Wai-Lun Chan

Dr. Franklin (Feng) Tao

Date defended: April 21, 2017

The Dissertation Committee for Frank Ceballos certifies
that this is the approved version of the following dissertation :

Interlayer Charge Transfer in van der Waals Heterostructures Formed by Transition Metal Dichalcogenide Monolayers

Dr. Hui Zhao, Chairperson

Date approved: April 21, 2017

Abstract

Since the discovery of graphene and its outstanding chemical, optical, and mechanical properties, other layered materials have been fiercely hunted for through physical and chemical means. Thanks to their van der Waals interaction, acting as weak glue, different types of layered materials can be stacked without considering their lattice mismatch. The properties of the resulting multilayer structures can be tuned by choice of the materials, layer thicknesses, sequence in which they are arranged, the relative orientation between the layers, and by external electrical, mechanical, and optical controls. This opens the possibility for a large array of applications across many different fields. With the vision to obtain the ability to precisely engineer materials with desired properties, using two-dimensional materials as Lego-blocks, early studies have shown that research in van der Waals stacked two-dimensional materials to be rich in discoveries and still on its early stages due to their abundant diversity. In order to characterize, understand, and improve the properties of van der Waals stacked two-dimensional materials, we first introduce and discuss the noninvasive laser spectroscopy techniques utilized to study them. To correctly interpret the data and to understand the limits of our ultrafast laser spectroscopy system, the dynamics the photocarriers undergo after the pump photoexcitation is examined. Next, the van der Waals stacked two-dimensional materials are introduced by order complexity. First, we discuss the results obtained from bilayers of MoS_2–$MoSe_2$ and $MoSe_2$–WS_2, which set the groundwork needed to understand more complex structures. We then move on to discuss trilayer MoS_2–WS_2–$MoSe_2$ and are able to time resolve the electron transfer process as electrons relocate from the $MoSe_2$ into the MoS_2 layer. Finally, in the spirit

of trying to engineer a new ultrathin material with a high absorption of light in the visible regime as well as extended the photocarrier lifetimes, we fabricated a set of samples that grew in complexity as additional layers were added. It was discovered that in our more complex multilayer structure WSe_2–$MoSe_2$–WS_2–MoS_2, that the absorbance peaked at 50% with about just 2.5 nm of material. Moreover, the photocarrier lifetimes were extended up to a few nanoseconds. With all these we show that van der Waals stacked two-dimensional materials can be engineered layer by layer with the resulting stack having desired properties.

This dissertation includes previously published authored material.

To my wonderful family.

Acknowledgements

The work of this thesis has been carried out at the Ultrafast Laser group in The University of Kansas during 2014-2017. This group is led by Dr. Hui Zhao, my committee chairman, and a wonderful adviser that has provided me with resources, ideas, an incredible amount of patience, and exceptional guidance throughout different projects during my years in The University of Kansas. Thank you Dr. Siyuan Han, Dr. Judy Wu, Dr. Wai-Lun Chan, and Dr. Franklin Tao for agreeing to serve on my committee. I will like to thank Nardeep Kumar, for introducing me to the lab and teaching me the experimental techniques as well as pointing out different ways to trace and correct faults in the experimental setups. Additionally, I will like thank to both Qiannan Cui and Jiaqi He, two labmates that provided me with additional guidance from which I have greatly benefited from. I will like to acknowledge Matthew Z. Bellus who showed me how to fabricate two-dimensional materials and multilayer samples. I will also like to thank Samuel D. Lane for sticking along with me during the summer of 2015 and accompanying me in the MoS_2–WS_2–$MoSe_2$ three-layer project. I will also like to thank Peymon Zereshki for being part of my last project. Finally, I will like to mentioned Dr. Shudi Pan and Xinwu who have given me a great deal of joy and friendship. To everyone who has been part of this journey, I will like to thank you.

Contents

1 Introduction **1**

1.1 The Rise of Mankind 1

1.2 The Rise of Graphene 2

1.3 Two-Dimensional Materials Beyond Graphene 3

1.4 Two-dimensional van der Waals Multilayer Heterostructures 5

1.5 Organization of the Dissertation 10

2 Spectroscopy Techniques and Carrier Dynamics **12**

2.1 Photoluminescence Spectroscopy 12

2.2 Absorption Spectroscopy 14

2.3 Time Resolved Pump-Probe Spectroscopy 15

2.4 Time-Domain Photocarrier Dynamics 22

2.4.1 Thermalization and Energy Relaxation 23

2.4.2 Exciton Formation 24

2.4.3 Exciton-Exciton Annihilation 26

2.4.4 Exciton Recombination 27

2.5 Spatially Resolved Pump-Probe Spectroscopy 30

2.5.1 Photocarrier Diffusion 30

3 Vertically Stacked Two-dimensional Multilayer Structures **36**

3.1 Extended Photocarrier Lifetimes and Charge Transfer Exciton Formation in a MoS_2–$MoSe_2$ Bilayer Heterostructure . . . 37
3.1.1 Experimental Results and Discussion . . . 37
3.2 Spatiotemporal Dynamics of Charge Transfer Excitons in a $MoSe_2$–WS_2 Bilayer Heterostructure . . . 47
3.2.1 Excitonic States in $MoSe_2$–WS_2 heterostructure . . . 47
3.2.2 Probing The Charge Transfer Excitons . . . 52
3.2.3 Dynamics of Charge Transfer Excitons . . . 55
3.2.4 Conclusion on $MoSe_2$–WS_2 Bilayer Heterostructure . . . 56
3.3 Highly Efficient and Ultrafast Charge Transfer in a MoS_2–WS_2–$MoSe_2$ Three-layer Heterostructure . . . 56
3.3.1 Experimental Section . . . 58
3.3.2 Coherent Electron Transport Across a Monolayer . . . 59
3.3.3 Simulation of the Electron Transfer . . . 61
3.3.4 Hole Transfer Across a Semiconducting Monolayer . . . 63
3.3.5 Long Lifetime of Photocarriers . . . 63
3.3.6 Conclusions in MoS_2–WS_2–$MoSe_2$ Three-layer Heterostructure . . . 64
3.4 Separating Electrons and Holes by Monolayer Increments in van der Waals Heterostructures . . . 66
3.4.1 Optical Properties and Exciton Lifetimes of WSe_2, $MoSe_2$, WS_2, and MoS_2 Monolayers . . . 66
3.4.2 Optical Properties of Multilayer Samples . . . 68
3.4.3 Probing the Electron Dynamics . . . 71
3.4.4 Probing the Hole Dynamics . . . 75
3.4.5 Summary . . . 77

4 Summary and Outlook **78**

Appendix **105**

A Sample Fabrication **105**

A.1 Sample Fabrication, Identification, and Annealing Treatment 105

B Estimation of Photocarrier Density in Single and Multilayer Structures **107**

B.1 Calculation of Photocarrier Density in Single Layer Materials 107

B.2 Calculation of Photocarrier Density in Multilayer Samples 109

B.2.1 Thin Film Sample on a Transparent Thick Substrate 109

B.2.2 Multiple Thin Films on a Transparent Thick Substrate 113

C Instrumental Response Time **119**

List of Figures

1.1 (a) Schematic representation of the TMDs layered structure where two layers of chalcogen atoms (shown in yellow) are separated by a layer of metal atoms (shown in purple) which together form a monolayer. The adjacent layers are held together by the weak van der Waals force to form bulk crystal. (b) Top view of the TMDs hexagonal crystal structure where the unit cell is shown by the dashed line. 5

1.2 Number of publications per year for different 2D materials. The data was collected from the ISI web of science. 6

1.3 Schematic representation of a bilayer heterostructure. 7

1.4 In a type II band alignment or ladder band align multilayer heterostructures, electrons (holes) are incline to transfer to the layer with the minimum (maximum) value of the conduction (valence) band energy (indicated by the purple arrows). Shortly after, charge transfer excitons will form across the interface and will recombine at a slower rate (as shown by the red arrow). 9

2.1 Typical photoluminescence spectroscopy setup in reflection geometry. 13

2.2 Typical absorption spectroscopy setup in reflection geometry. 14

2.3 Typical pump-probe experimental setup in reflection geometry. 16

2.4 The orange symbols represent an example of the differential reflection obtained from a WSe_2 monolayer (ML). The black squares in the inset shows the relation between the signal and the exciton density. The solid red line is a linear fit to the data. Such an experimentally established relation is used to convert the measured signal to the exciton density (the blue symbols). 19

2.5 The evolution of photocarriers after instantaneous interband excitation. Reproduced with permission.[78] Copyright 2016, Advanced Functional Materials. 22

2.6 Thermalization and energy relaxation of photocarriers in few-layer MoS_2. Two different relaxation processes can be identified and their physical origins are attributed to carrier thermalization that occurs within the first 20 fs mainly via carrier-carrier scattering and carrier cooling that occurs via carrier-phonon scattering and lasts about 0.6 ps. Reproduced with permission.[84] Copyright 2014, American Chemical Society. 24

2.7 (a) The differential reflection signal from ML $MoSe_2$ measured at different pump fluences. The pump and probe wavelengths as well as the pump fluence are noted in the legend. (b) The peak differential reflection and the signal at 3 ps measured as a function of pump fluence. (c) From the bi-exponential fits (shown as the red curves in (a)), the fast decay constants are extracted and plotted as a function of pump fluence. (d) The relative strength of the fast decay component measured as a function of pump fluence. No dependence is observed in either the fast decay constant or the relative strength of the fast decay with the pump fluence. Reproduced by permission from The Royal Society of Chemistry.[80] 25

2.8 Left column: Exciton density as a function of probe delay for various initial injected densities. At times scales shorter than 100 ps, a fast decay component starts to develop as the initial exciton density increases. The red solid curves are single exponential fits to the data after 150 ps. Right column: The quantity $N_0/N(t) - 1$ is calculated from the data in the left panels as function of the probe delay. The red lines are linear fits. Reprinted with permission.[96] Copyright 2014, American Physical Society. 28

2.9 Schematic representation of transient absorption microscopy measurements of exciton diffusion in 2D semiconductors. A tightly focused pump pulse (blue beam) injects photocarriers and at a later time a probe pulse (red beam) monitors their spatial profile. 31

2.10 Schematic illustration depicting the imaging process of the photoexcited carriers where a pump pulse is scanned relative to a fixed probe beam. 32

2.11 (a) The differential reflection from a 20-layer black phosphorus film measured as function of probe delay and relative probe position. This measurement was obtained by scanning the probe spot relative to the fixed pump spot along the armchair direction for different probe delays. (b) Examples of the spatial profiles at different probe delays. The solid lines are Gaussian fits. (c) From the Gaussian fits shown in (b) and others not shown, the square width of the profile is extracted and plotted as function of probe delay (black squares). The solid red line is a linear fit to the data and displays the linear evolution of the width squared. Reprinted with permission.[108] Copyright 2015, American Chemical Society. 33

2.12 Summary of known exciton and electron-hole pairs diffusion coefficients at room temperature for several 2D materials (solid symbols) and bulk materials (open symbols).[102,108–116] Reproduced with permission.[78] Copyright 2016, Advanced Functional Materials. 34

3.1 Schematic illustrations of Type I, II, and III band alignment in bilayer heterostructures. The valence (conduction) bands are indicated by the green (blue) color. The direction of the electron and hole flow are denoted by the pink arrows. 38

3.2 Quantum well application formed from Type I heterojunctions. 39

3.3 (a) Optical image of MoS_2 ML flake on a transparent substrate. (b) The ML $MoSe_2$ on a Si-SiO_2 substrate. (c) The MoS_2–$MoSe_2$ heterostructure sample fabricated by transferring the MoS_2 ML shown in (a) on top of the $MoSe_2$ ML in (b). (d) The type two band alignment of the conduction band and the valence band predicted from first principles.[62–64] (e) PL spectra generated from MoS_2 ML (blue), $MoSe_2$ ML (red), and the heterostructure region (purple). Reproduced with permission.[45] Copyright 2014, American Chemical Society. 40

3.4 (a) Schematic illustration of the pump–probe configuration used to study the transfer of electrons from $MoSe_2$ to MoS_2 in the heterostructure. Differential signal obtained as function of probe delay in a long (b) and short (c) time scale. The solid black curve in (b) is a single exponential fit. (d) Differential reflection signal at 3.0 ps as function of probe wavelength. (e) Decay constant as a function of pump fluence. These were deduce by repeating the measurement at different fluences and fitting the signals with single exponential curves. An example is shown in (b). (f) Differential reflection signal at 3.0 ps as a function of pump fluence. Reproduced with permission.[45] Copyright 2014, American Chemical Society. 43

3.5 (a) Schematic illustration of the pump–probe configuration used to study the transfer of holes from MoS_2 to $MoSe_2$ in the heterostructure. The differential signal obtained as function of probe delay in a long (b) and short (c) time scale. The purple squares in (b) and (c) show the differential signal obtained from the heterostructure using a 655.0 nm pump and a 790.0 nm probe. The differential reflection signal from a $MoSe_2$ ML is shown as the red circles in (b) and (c). The orange circles in (c) show the differential reflection signal from the heterostructure when a 670.0 nm pump excites both layers while 790.0 nm probe senses the $MoSe_2$. The gray squares in (c) represent the scaled signal obtained from the orange squares. (d) Differential reflection signal at 3.0 ps as function of pump wavelength (purple squares). The gray curve is the PL generated from a MoS_2 ML. (e) Decay constants from the heterostructure (purple squares) and from the $MoSe_2$ ML (red circles) plotted as function of pump fluence. (f) Differential reflection at 3.0 ps for the heterostructure (purple squares) and the $MoSe_2$ ML (red circles) plotted as function of pump fluence. Reproduced with permission.[45] Copyright 2014, American Chemical Society. 45

3.6 (a) Schematic illustration of the $MoSe_2$–WS_2 heterostructure. (b) Microscope images of the sample containing the heterostructure (indicated by the red box) and the individual $MoSe_2$ and WS_2 monolayer regions on the a Si–SiO_2 substrate. Band alignment predicted by first principle calculations,[63] showing 60 and 270 meV conduction and valence band offsets, respectively. (d) Energy diagram of excitons states determined by the photoluminescence spectrum. Reproduced by permission from The Royal Society of Chemistry.[123] 48

3.7 Room Temperature photoluminescence spectra of the $MoSe_2$–WS_2 heterostructure (black) and the individual WS_2 (blue, divided by 23) and $MoSe_2$ (red) monolayers obtained under the same experimental conditions. The pink curves are the two components of a double-Gaussian fit to the 810 nm peak. Reproduced by permission from The Royal Society of Chemistry.[123] 51

3.8 Differential reflection signals measured with 730 nm pump and 810 nm probe pulses from the $MoSe_2$–WS_2 heterostructure (black) and individual $MoSe_2$ (blue) at room temperature. The red and orange curves are signals from individual $MoSe_2$ and WS_2 monolayers, with 395 nm / 790 nm and 385 nm / 620 nm pump/probe wavelengths, respectively. The purple curve shows the signal from the heterostructure sample with 810 nm / 730 nm configuration. The inset shows the results near zero probe delay. Reproduced by permission from The Royal Society of Chemistry.[123] 53

3.9 (a) Differential reflection signals measured at room temperature with 730 nm pump and 810 nm probe pulses from the $MoSe_2$–WS_2 heterostructure with different values of the pump pulse fluence as indicated. The red curves are bi-exponential fits. (b) The magnitude of the differential reflection signal, represented by the signal at a probe delay of 3 ps, as a function of the pump fluence. The inset shows the short (black squares) and long (red circles) time constants obtained from the fits shown in (a). Reproduced by permission from The Royal Society of Chemistry.[123] 54

3.10 (a) Differential reflection signal of the $MoSe_2$–WS_2 heterostructure as a function of the probe delay and probe position at room temperature. The pump and probe wavelengths are 730 and 810 nm, respectively. (b) Examples of the spatial profiles of differential reflection at several probe delays. The solid curves are Gaussian fits. (c) Squared width of the profile deduced from Gaussian fits as a function of the probe delay. The linear fit, as indicated by the red line, corresponds to an exciton diffusion coefficient of 14 cm^2 s^{-1}. Reproduced by permission from The Royal Society of Chemistry.[123] 57

3.11 (a) Schematic illustration of the MoS_2–WS_2–$MoSe_2$ trilayer sample studied. (b) Band alignment of the three-layer sample and the pump–probe configuration, where a pump pulse excited the $MoSe_2$ layer and a probe pulse detects carriers in MoS_2. (c) Photoluminescence spectra of the three-layer (purple) and monolayers of MoS_2 (black), WS_2 (red, divided by 50), and $MoSe_2$ (blue) under steady excitation of 405 nm and 0.5 μW. (d) Differential reflection of a 1.88 eV probe pulse (sensing carriers in MoS_2) after a pump pulse of 1.57 eV injected carriers in $MoSe_2$. The red curves are fits. (e) The gray symbols are differential reflection of a 2.00 eV probe (sensing WS_2 of the three-layer) after a pump pulse of 1.57 eV injected carriers in $MoSe_2$. The purple symbols are measured from a WS_2 monolayer sample with a 3.14 eV pump pulse injecting carriers. The blue symbols are replotted from (d) for comparison. (f) Charge transfer time as a function of injected carrier density. Reprinted with permission.[138] Copyright 2017, American Chemical Society 60

3.12 (a) Schematic diagram of energy levels involved in the excited electron dynamics. (b) Decay of population of excited electron states. Adapted with permission.[138] Copyright 2017, American Chemical Society 62

3.13 (a) Experiment configuration used to study transport of holes from MoS_2 to $MoSe_2$. A 1.88-eV pulse (blue arrow) is used to excite the MoS_2 layer. Holes transferred to $MoSe_2$ are detected by a probe pulse of 1.57-eV (red arrow). (b) Differential reflection signal of the 1.57-eV probe after the three-layer sample is pumped by 1.88 (blue) and 1.75 eV (red) pumps, respectively. (c) The differential reflection signal at a probe delay of 3 ps as a function of the pump photon energy. The two data points corresponding to b are plotted with the corresponding colors. Adapted with permission.[138] Copyright 2017, American Chemical Society 64

3.14 (a) Blue solid symbols show the differential reflection of a 1.88 eV probe after a 1.57 eV pump pulse injected carriers with a peak density of 1.1×10^{10} cm^{-2} in the $MoSe_2$ layer of the three-layer sample. Open symbols represent results from a MoS_2 monolayer, with the same probe, but with a 3.14 eV pump pulse that injects carriers with the same density. The red curves are exponential fits. (b) The differential reflection of a 1.57 eV probe after a 2.00 eV pump pulse injected carriers in the three-layer sample (blue solid symbols) and a $MoSe_2$ monolayer (open symbols) with a density of 9.5×10^{10} cm^{-2}. The red curves are exponential fits. Adapted with permission.[138] Copyright 2017, American Chemical Society . . 65

3.15 (a), (e), (i) and (m): Optical microscopy image of the WSe_2, $MoSe_2$, WS_2, and MoS_2 MLs on a Si–SiO_2 substrate. (b), (f), (j), and (n): Absorbance spectra of WSe_2 (purple), $MoSe_2$ (orange), WS_2 (green), and MoS_2 (blue) MLs. The dashed vertical lines denote previous reported A and B exciton resonances. (c), (g), (k), and (o): Photoluminescence (PL) spectra of the MLs samples measured under the same conditions. (d), (h), (l), and (p): Decay of the transient absorption signal. The solid curves represent bi-exponential fits where the long decay constant extracted are shown in the corresponding panel. 67

3.16 Optical images of the WSe_2 ML (a), WSe_2–$MoSe_2$ (d), WSe_2–$MoSe_2$–WS_2 (g), and WSe_2–$MoSe_2$–WS_2–MoS_2 (j) on quartz substrates. The absorption and PL spectra taken under the same experimental conditions (gray curves) for the WSe_2 ML (b) and (c), WSe_2–$MoSe_2$ (e) and (f), WSe_2–$MoSe_2$–WS_2 (h) and (i), and WSe_2–$MoSe_2$–WS_2–MoS_2 (k) and (l). In the absorption spectra panels, the black curves are composed by summing the individual MLs spectra. The quenching factors for the PL peaks are labeled in the legend and are shown as the non-gray curves. 70

3.17 (a), (d), and (g) Schematics of the pump-probe configuration used to study the transfer of electrons from different layers into the conduction band minimum. (b) and (c) Differential reflection signal (sensing electrons $MoSe_2$) as function of probe delay in a short (b) and long (c) temporal regions. The solid red curve in (b) is the pump-probe cross-correlation function and in (c) is a bi-exponential fit with the long decay constant shown in the figure. (e) and (f) are the same as (b) and (c) but for the three-layer sample (sensing electrons in WS_2). (h) and (i) show the differential reflection signal in the four-layer structure (sensing electrons in MoS_2 layer) in a short (h) and (i) long time scale. The solid red curves are fits. 73

3.18 (a), (d), and (g) Schematics of the pump-probe configuration used to study the transfer of holes from different layers into the valence band maximum. As additional layers are added, the lifetime of the holes was measured in different regimes. The short time scale regime results are shown in (b), (e), and (h) while the long scale regime results are shown in panels (c), (f), and (i). The solid red curves are exponential fits with the extracted lifetime constants shown in the corresponding panel. 76

A.1 Schematic of the multilayer sample preparation procedure. 106

B.1 Schematic of the multiple reflections that occur when light is incident on a thin film placed on a thick substrate. 110
B.2 Schematic of light being reflected from a two thin film system. 114
B.3 Schematic of light being reflected from a k thin film system. 115
B.4 Schematic of the calculations necessary to determined the fraction of absorbed intensity by each layer for a 4-layer thin film system. 117

C.1 Calculation of the pump–probe cross correlation function. 120

List of Symbols and Abbreviations

α	Absorption coefficient
$\Delta R/R_0$	Differential reflection
$\Delta R/R_{sub}$	Differential reflection spectrum
$\Delta T/T_0$	Differential transmission
δ	Acquired phase for every round trip light travels
γ	Exciton–exciton annihilation rate
τ	Exciton or photocarrier lifetime
τ_e	Electron transfer time
$\tilde{n}$	Complex index of refraction
A	Absorbance
D	Diffusion coefficient
d	Sample thickness
e	Euler's number
E_{pulse}	Energy of each pulse
F_{peak}	Pulse peak fluence

f_{rep}	Repetition Rate
I	Transmittance intensity
I_0	Incident intensity
k	Extinction coefficient
N	Photocarrier density
n	Index of refraction
N_{sat}	Photocarrier density that causes the absorption coefficient to decrease by 50%
P	Time averaged laser power
R	Reflection coefficient
r	Fresnel amplitude reflection coefficient
R_Q	Reflectance of the quartz substrate
R_{S+Q}	Reflectance of the sample on quartz
T	Transmission coefficient
t	Fresnel amplitude transmission coefficient
t_{int}	Integration time
w	Full width at half maximum of the photocarrier distribution at a later time
w_0	Full width at half maximum of the initial photocarrier distribution
X_{CT}	Charge transfer exciton
2D	Two-dimensional
3D	Three-dimensional

BBO	Beta barium borate crystal
CB	Conduction band
CCD	Charge-coupled device
fs	Femtosecond
FWHM	Full width at half maximum
h-BN	Hexagonal boron nitride
HOMO	Highest occupied molecular orbital
log10	Log base 10
LUMO	Lowest unoccupied molecular orbital
ML	Monolayer
PDMS	Polydimethylsiloxane
PL	Photoluminescence
ps	Picosecond
SiO_2	Silicon dioxide
TMD	Transition metal dichalcogenide
TRPL	Time-resolved photoluminescence
VB	Valence band

Chapter 1

Introduction

1.1 The Rise of Mankind

On June 8th, 1924, in their attempt to become the first men to reach the peak of Mount Everest, George Mallory and Andrew Irvine were spotted a few hundred meters from reaching the summit of Earth's highest mountain. They disappeared into the clouds in their attempt to make the first ascent and never to return. Whether they reached the mountain top or died within reach of grasping their goal, still remains a mystery.

A year earlier, when a reporter of the New York Times asked George Mallory why climb Everest, he boldly replied "Because it's there." No other three words can better depict the spirit of pure science. We require no extra justification in order to embark into a journey of struggle where the end, the peak of the mountain, is always hidden within the clouds and only by reaching it one conquers the unknown. If one cannot understand that there is something in men that awakens and forces him to challenge the unknown when presented with a mountain like Everest, one won't be able to comprehend the noble reason behind every scientific endeavor. Why travel to Mars? Why explore distant galaxies? Why spend 1.1 billion dollars and countless men hours over a span of 40 years in a project that has no practical benefits simply to confirm Einstein's well accepted 100 year old theory? Why attempt to understand the universe at such a small scale? Questions which sometimes even scientist struggle to satisfactorily answer but can easily be justified with Mallory's

simple yet brilliant answer "Because it's there." It is the expression of our curiosity and thirst for knowledge what has constantly pushed us forward. From the first caveman experimenting with different rocks to the modern man with control over the electric charge, the story of mankind's rise cannot omit the undeniable fact that understanding and controlling the properties of materials is what has provided us with the technological advances we now possess.

1.2 The Rise of Graphene

We have long departed from being satisfied with the natural elements, which had led to development of synthetic methods that yield carefully crafted materials with more controllable properties. For example, molecular beam epitaxy, a method that was developed in 1968 at Bell Laboratories, is a very precise technique for growing highly uniform crystals with low defects. Such thin-film deposition techniques enable the further downscaling of electronic devices and allow for tunable properties which can be exploited in high mobility transistors and solar cells.[1]

Over the past five decades, intensive efforts were invested in isolating single layers of graphite (graphene) which was predicted to possess groundbreaking properties. However, the best results produced materials with 10-50 layers. Additionally, theoretical work from Landau and Lifshitz showed that thermal fluctuations at any finite temperature in low dimensional materials would lead to large displacement of atoms, comparable to their interatomic distances, thus making graphene a highly unstable material.[2] Therefore, as a result of years of failed attempts supported with theory from notable physicist, it was believed by many that the existence of monolayer (ML) graphene was not possible.

It was not until 2004 that graphene was first isolated by Andre Geim's group, at Manchester University.[3] The reported cleaving method (absurdly simple yet revolutionary) for producing one atomic layer thick crystals consisted in rubbing a fresh surface of a layered crystal against another. This produced a great amount flakes, mostly of bulk crystal, but among the results occasionally MLs could be found. Since MLs are transparent to visible light it is key to place them on top of a silicon wafer capped with a layer of silicon dioxide (SiO_2) of the right thickness for optical

contrast identification. The very low yield along with the microscopic size and random shape of the MLs produced by the cleaving method makes it an unsuitable technique for any industrial applications. However, as crude as the technique may be it proved that macroscopic high quality two-dimensional (2D) materials can exist under ambient conditions. As a result, graphene rapidly became a rising star appearing in a large number of articles (currently estimated 24,000 per year) and across many journals. This obsession with graphene is no surprise. After all, this one-atom-thick sheet of carbon has shown to be more conductive than copper,[4] stronger than any other material,[5] transparent and yet impermeable to gases,[6] all which make it an attractive candidate for a large number of applications. As a result of this interest, the fabrication of graphene has evolved from microscopic cleaved flakes to the roll-to-roll production of 30 inch graphene films grown by chemical vapor deposition onto flexible copper substrates demonstrating that 2D crystals can be reliably grown in the large sizes required for industrial applications.[7]

However, graphene devices on standard SiO_2 substrate show inferior properties to the expected properties of intrinsic graphene. This lead to the realization of graphene devices on hexagonal boron nitride (h-BN) substrates, graphene heterostructures made out of mechanically exfoliated graphite and bulk h-BN, which showed improved mobilities and carrier inhomogeneities by an order of magnitude when compared to graphene devices on SiO_2 substrates.[8] Consequently, epitaxial grown graphene and h-BN were stacked on top of each other to produce wafer-scale high performance devices.[9]

1.3 Two-Dimensional Materials Beyond Graphene

An exciting fact is that graphene does not stand alone in 2D land. A whole family of layered materials with strong covalent intralayer bonds and weak van der Waals like coupling between adjacent layers offers to extend the 2D library up to 500 types[10] which includes: the transition metal dichalcogenides (TMDs), transition metal oxides, the already mentioned h-BN with insulating properties, phosphorene which unlike graphene has a bandgap, silicine from which field effect transistors operating at room temperature have been built,[11] germanene (a graphene analogue)

which offers a bandgap,[12] and even superconductors such as $NbSe_2$.[13] TMDs with formula MX_2 (M = Mo, W; X = S, Se, Te) are among the most well studied 2D semiconductors. Their layered structure is formed by two layers of chalcogen atoms separated by a layer of metal atoms as is shown in Figure 1.1a and form a 2D honeycomb lattice just like graphene, see Figure 1.1b. The adjacent layers are weakly coupled by the van der Waals force thus allowing for the mechanical exfoliation of ML TMDs. Additionally, TMDs MLs have been synthesize by chemical vapor deposition and physical vapor transport techniques.[14] Capable of withstanding large amounts of strains without compromising their properties;[15,16] with a transition from indirect to direct bandgap in the visible spectrum as the thickness reaches the ML limit;[17,18] strong photoluminescence;[19–21] valley-selective optical coupling;[22–25] large binding energies of excitons, trions, and biexcitons;[26–29] and strong nonlinear optical responses,[30–33] TMDs offer a new platforms for optoelectronics applications and flexible electronics.[34] By taking advantage of these superior properties and emerging new physical phenomena, these 2D TMDs have been used to fabricate solar cells,[35,36] photodetectors,[35] light-emitting diodes,[36–38] field-effect transistors,[39,40] and integrated circuits.[41,42] Other types of 2D semiconductors have also been discovered and extensively studied. For example, phosphorene, a single layer of phosphorus atoms, has emerged as a promising semiconductor due to its novel and transport properties. Although, these 2D semiconductors are promising platforms as individual materials, their great potential lies in the fact that they can be combined without lattice matching restrictions; therefore, allowing the fabrication of new materials with properties that are engineered at the atomic level.

The research in 2D materials has intensify over the past decade. To demonstrate this, Figure 1.2 shows the number of publications per year for some of the most common 2D materials. Starting with the discovery of graphene in 2004, the research in graphene has exponentially grown, reaching up to 24,000 publications in just 2016 alone. Other 2D materials, such as MoS_2, WS_2, $MoSe_2$, and WSe_2, started to show a similar exponentially-growing interest, after 2010. Since the research in 2D materials is intense as ever and their applicability has expanded to the realm of multilayer heterostructures, the exponential increase in the number of publications for these 2D materials

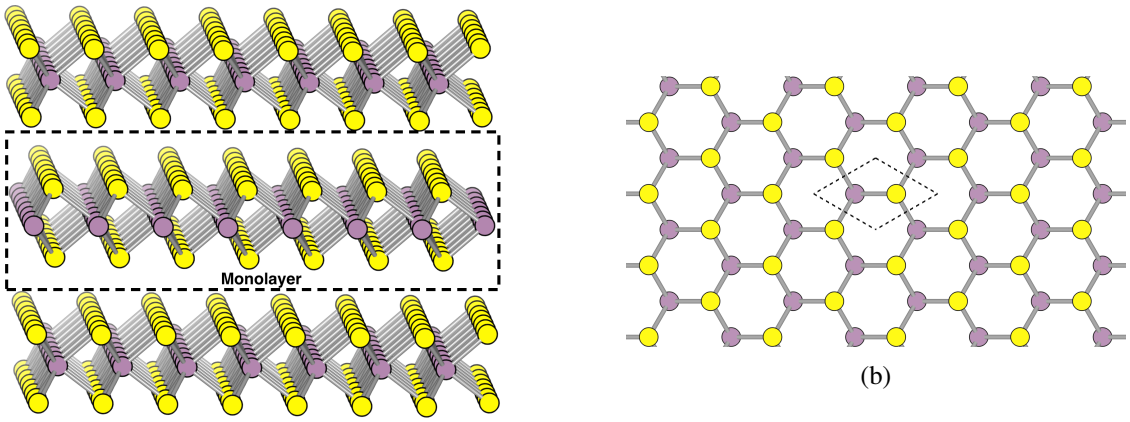

(a) (b)

Figure 1.1: (a) Schematic representation of the TMDs layered structure where two layers of chalcogen atoms (shown in yellow) are separated by a layer of metal atoms (shown in purple) which together form a monolayer. The adjacent layers are held together by the weak van der Waals force to form bulk crystal. (b) Top view of the TMDs hexagonal crystal structure where the unit cell is shown by the dashed line.

shows no sign of wearing off for the next several years. It is interesting to note that the publications in 2016 for MoS_2, six years later since it started to catch the interest of the field, is about the same as those of graphene in 2010, six years after its discovery. Comparatively, the interest in TMDs is growing as fast as the interest in graphene once did.

1.4 Two-dimensional van der Waals Multilayer Heterostructures

Stimulated by these discoveries, significant efforts have been devoted to identifying, fabricating, and characterizing various ML materials. Thanks to their van der Waals interaction, acting as weak glue, different types of layered materials can be reassembled without considering their lattice mismatch to form multilayer heterostructures that are engineered monolayer by monolayer, as shown in Figure 1.3. Although the van der Waals interaction between the stacked layers is weak, the electron orbitals each layer possesses extend out of the plane and affect the adjacent layers.[43] Therefore, the electronic properties of the stacked layers are effectively coupled. The properties of the resulting multilayer heterostructures can be tune by choice of the materials,[44,45] layer thicknesses,[17,18,46,47] sequence in which they are arranged,[48,49] the relative orientation between the

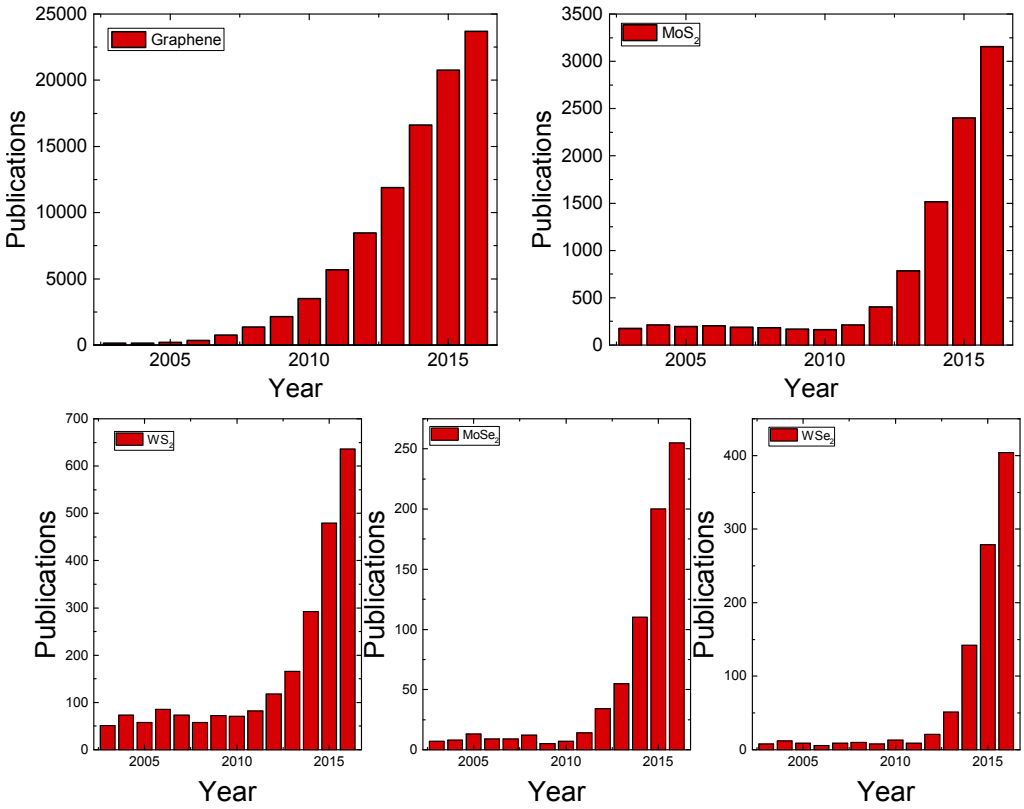

Figure 1.2: Number of publications per year for different 2D materials. The data was collected from the ISI web of science.

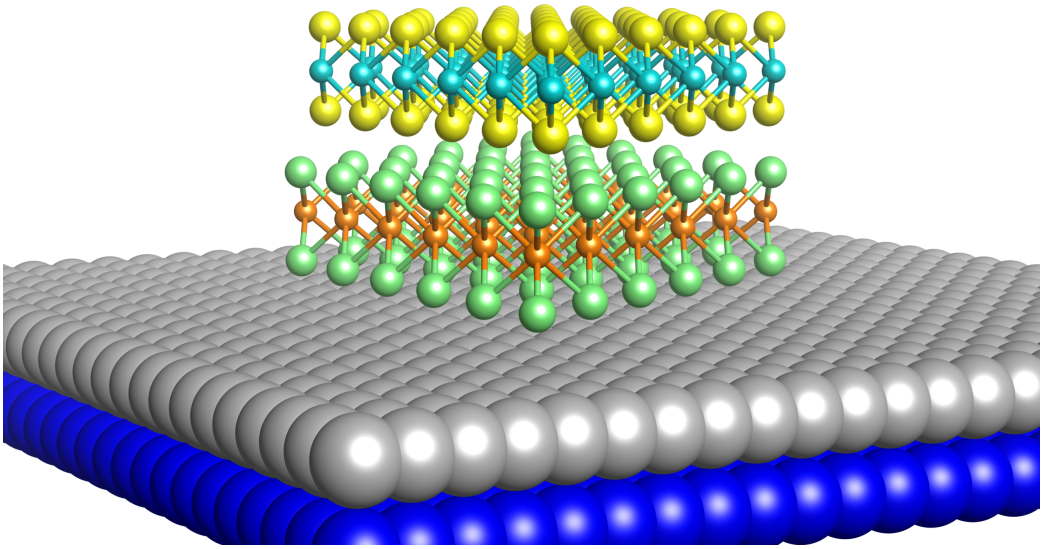

Figure 1.3: Schematic representation of a bilayer heterostructure.

layers,[50–53] and by external electrical,[48] chemical,[54] mechanical,[15,16] and optical[55] controls. This opens the possibility for a large array of applications across many different fields.

These 2D van der Waals multilayer heterostructures can be realized by either manually stacking different layers together[44,45] or directly grown by chemical means.[14,53,56] The resulting assembled structure, that can possibly have superconducting, conducting, semiconducting, and insulating layers, represents a new artificial material which offers a large amount of controls to fine tune its properties. The interface, when assembled properly, can be atomically sharp, thin as two atomic layers, and free of contaminants.[57] So far, most studies of van der Waals heterostructures have focused on combining two different MLs,[56,58–61] which has establish the foundation for understanding multilayer heterostructures.

Based on first-principle calculations, TMD bilayer heterostructures form different types of band alignments.[62–64] Multilayer heterostructures that form type-II band alignment (see Fig 1.4) or ladder band alignment are the focus of this dissertation. Here the bottom of the conduction band (CB) and top of the valence band (VB) reside in different layers. Upon optical excitation in a heterostructure, electrons and holes can be selectively injected into specific layers in the multilayer structure. Normally, the excited photocarriers shortly form direct excitons, electrically neutral quasiparticle

consisting of an electron and hole bounded by their electrostatic Coulomb force, that will live and decay in the layer they were created; however, because of the band alignment, where lower energy states are available and accessible in a different layer, spatial separation of most electrons and holes after photoexcitation will ensue (see Figure 1.4). Consequently, the formation of direct excitons will be limited by the rate in which the charge separates between the layers. Despite the fact that electrons and holes populate different layers, their electrostatic Coulomb force bounds them together to form bound electron-hole pairs (charge transfer excitons) across the interface. As a result, the spatial overlap in the charge transfer exciton's electron and hole wave functions is reduce. This together with the increase in separation in momentum space between the CB minimum and VB maximum gives rise to charge transfer excitons whose lifetimes are longer than those of direct excitons. These results have been experimentally verified by several groups.[45,60,65] So far all the multilayer heterostructures that have been discussed are vertically assembled by manually stacking or growing different layers of 2D materials on top of each other. In these stacked multilayer structures, the current transports out of the plane of the 2D materials. Additionally to the vertical structures, lateral bilayer heterostructures have also been realized. In contrast to the vertical structures, these cannot be manually assembled, the current transports within the plane of the 2D materials, and can only be effectively realized through lateral epitaxial growth.[56,66–71] Moreover, the lattice mismatch between the 2D materials used to form these structures plays a critical role in the formation of seamless high quality interfaces.

For several decades, multilayer structures composed with different three-dimensional (3D) semiconductors have been the basis for light-emitting diodes,[72] diode lasers,[73] and high-speed transistors.[74] In the heart of it all is the p-n junction. Analogously to the 3D multilayer structures, atomically thin p-n junctions have been achieved by creating multilayer structures with p and n doped 2D materials. For example, by putting together ML WSe_2, a p-type 2D semiconductor, and ML MoS_2, a n-type semiconductor, the thinnest possible p-n junctions have now been obtained.[75] Additionally, a vertical field-effect transistor created by sandwiching few-layer MoS_2 between ML graphene and a thin metal ohmic contact was shown to deliver a high current density

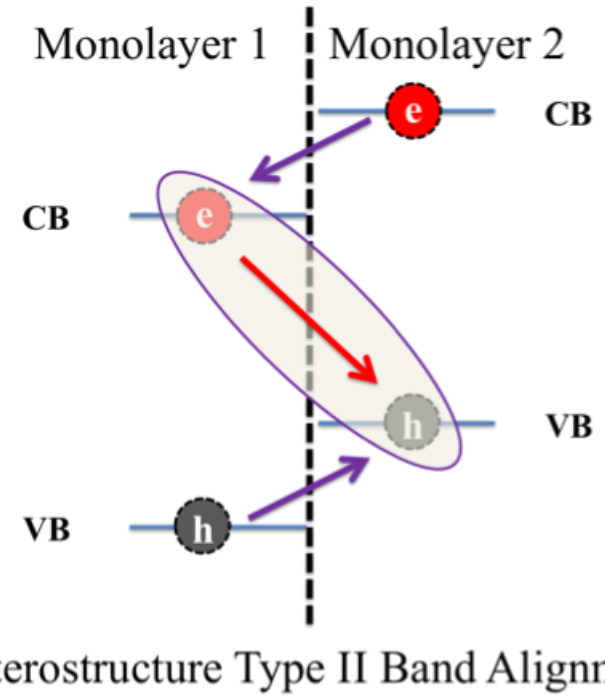

Figure 1.4: In a type II band alignment or ladder band align multilayer heterostructures, electrons (holes) are incline to transfer to the layer with the minimum (maximum) value of the conduction (valence) band energy (indicated by the purple arrows). Shortly after, charge transfer excitons will form across the interface and will recombine at a slower rate (as shown by the red arrow).

of 5,000 A/cm^2 and a room temperature on-off ratio $> 10^3$.[76] Photodetection devices based on 2D van der Waals heterostructures achieving external quantum efficiency greater than 30% have also been demonstrated.[49] To do this, they realized a device consisting of graphene/TMD/graphene where the two graphene electrodes where electrostatically n and p doped thus creating a built in potential. The researchers from Manchester University observed that this made possible to dissociate electron-hole pairs generated in the TMD layer. Using a similar approach, a high-speed photodetection device consisting of graphene/WSe_2/graphene sandwich between hBN showed a photoresponse time as short as 5.5 ps.[77] This ultrafast response time was tunable and depended on the voltage applied as well in the TMD thickness.

1.5 Organization of the Dissertation

The structure of the dissertation is as follows:

In Chapter 2, the noninvasive techniques used to characterized 2D materials as well as the van der Waals stacked 2D materials are reviewed. Photoluminescence and absorption spectroscopy are first introduced. Next, the ultrafast pump–probe technique is discussed in detail. In order to correctly interpret the experimental results extracted with the pump–probe technique, we examine the photocarrier dynamics shortly after the pump excitation and long after the pump excitation. Finally, we discuss how adding precise control of the pump and probe relative position allows us to monitor the evolution of the photocarrier density in real space.

In Chapter 3, the samples studied using the techniques discussed in Chapter 2 are introduced by order of complexity. First the MoS_2–$MoSe_2$ and $MoSe_2$–WS_2 bilayer heterostructures are discussed. Both of these exhibit strong photoluminescence quenching as well as extended photocarrier lifetimes. In the $MoSe_2$–WS_2 bilayer, by adding spatial resolution to our study, it is discovered the charge transfer excitons display a similar in plane transport than that of excitons in TMD monolayers. In the MoS_2–WS_2–$MoSe_2$ three-layer sample, strong photoluminescence quenching was observed as well as photocarrier lifetimes that were extended up to 1 ns. Moreover, by injecting photocarriers into the $MoSe_2$ layer of the heterostructure, we were able to time resolve the electron

transfer between $MoSe_2$ and MoS_2. The deduced electron transfer time of about 1.5 ps and its coherent nature were reproduced by non-adiabatic molecular dynamics calculations. In the spirit of trying to engineer a new material with a high absorption of light in the visible regime as well as extended photocarrier lifetimes, we fabricated a set of samples that grew in complexity as additional layers were added. Seeing that a type II band alignment separated the electron and holes in the bilayer heterostructures and that the charge transfer was still highly effective and ultrafast in the three-layer sample with a ladder band alignment in both the conduction and valence band, the following samples were fabricated: WSe_2 monolayer, WSe_2–$MoSe_2$, WSe_2–$MoSe_2$–WS_2, and WSe_2–$MoSe_2$–WS_2–MoS_2. In these samples as the number of layers was increased, it was observed that their photoluminescence was increasingly quenched, their absorbance increased, and their photocarrier lifetimes significantly extended. All of these was possible due to their individual properties as monolayers and their ordering in the stacking. The WSe_2–$MoSe_2$–WS_2–MoS_2 four-layer sample displayed the strongest quenching, up to 50% absorbance in certain regions of the visible spectrum, and electron and holes lifetimes that were extended up to a few nanoseconds. With this, we have demonstrated that complex van der Waals stacked can be fabricated with desired properties by carefully selecting the constituent layers and their ordering.

We conclude the dissertation by providing a brief summary and pointing the direction in which the field is going. In Appendix A, the fabrication of 2D materials as well as van der Waals stacked structures is described. In Appendix B, the estimation of the photocarrier density in single and multilayer structure is discussed in detail. Finally, in Appendix C, details about the instrumental response function and its calculation are reviewed.

Chapter 2

Spectroscopy Techniques and Carrier Dynamics

In this section, the methods used to study and characterize 2D materials are introduced. The steady-state photoluminescence (PL) and absorption spectroscopy are described in section 2.1 and 2.2, respectively. In section 2.3, the time resolved pump-probe technique is discussed in detail and the photocarrier dynamics are described in section 2.4. Finally, in section 2.5 a variation of the pump-probe technique used to measure the diffusion of photocarriers is discussed. Part of the discussion in section 2.3, section 2.4, and section 2.5 were published in Advanced Functional Materials.[78]

2.1 Photoluminescence Spectroscopy

Steady-state photoluminescence spectroscopy is a contactless technique used to probe the electronic structure of the 2D materials. Usually, a monochromatic light source is directed onto a sample and focused by a 20× or 100× objective lens. If the sample is on a transparent substrate, the light that transmits through it is collected by a second objective lens and guided into a spectrometer equipped with a thermoelectrically cooled charge-coupled device (CCD) camera. Otherwise, the reflected diverging light is collimated by the same objective lens and directed into the spectrometer for data collection, as shown in Figure 2.1. To prevent the unwanted light from being reaching the

detector and affecting the PL measurement, a set of filters are placed before the detector. If the photon energy of the light source, in our measurements this is typically between 1.5 to 3.0 eV, is higher than the bandgap of the material, photocarriers (either electron-hole pairs or excitons) will be generated. Electron-hole pairs generated at high energy levels rapidly relax to the band edge, as it will be discussed in section 2.4, by non-radiative scattering processes such as carrier-carrier and carrier-phonon scattering. Shortly after, excitons are formed in these 2D materials and the excess energy is released either radiatively or non-radiatively. In materials free of defects, the energy is dissipated through the emission of light. In other cases, when the 2D material is rich of defects, the exciton population is rapidly trapped by the defects which can consequently greatly reduce the emission of light of the 2D material. Since photocarriers first relax to the band edges and then return to their equilibrium state, the emitted light energy reveals the difference in energy between the excited and equilibrium state. The PL technique can be used to determine the thickness of the 2D films, since the electronic structure evolves as function of layers.

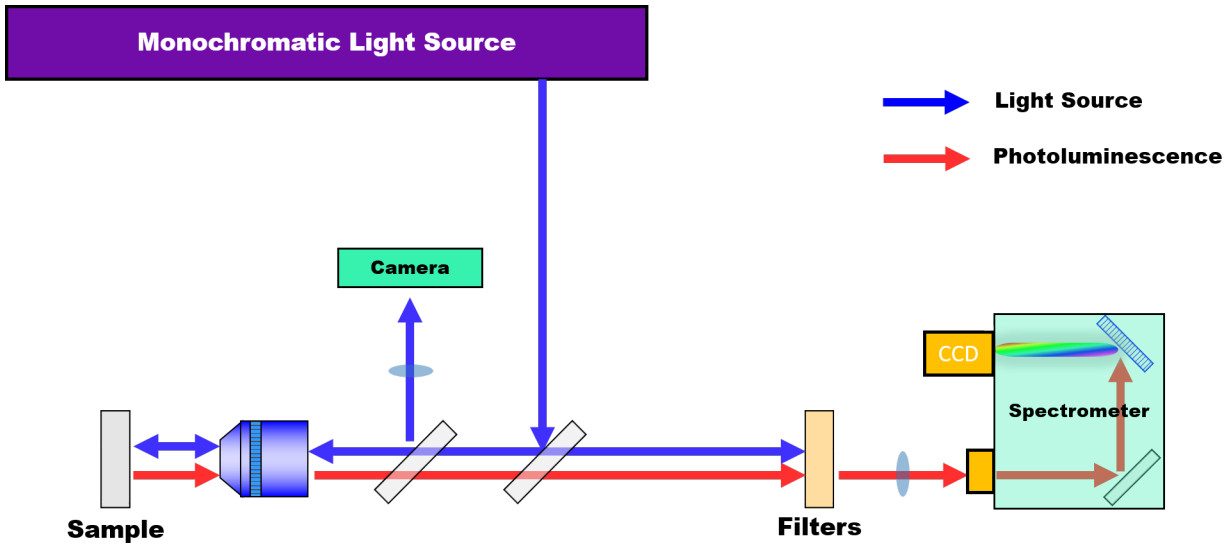

Figure 2.1: Typical photoluminescence spectroscopy setup in reflection geometry.

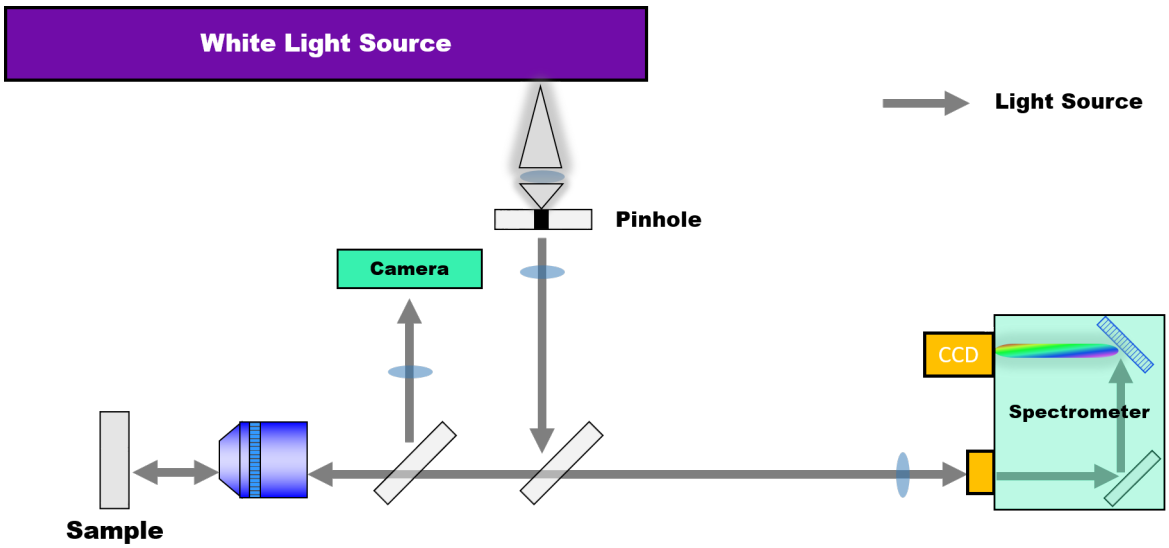

Figure 2.2: Typical absorption spectroscopy setup in reflection geometry.

2.2 Absorption Spectroscopy

As discussed in the previous section, some materials are not efficient in generating PL. Moreover, the PL spectrum only reveals the energy released when and excitons recombine which is not necessarily the bandgap of the 2D material. Therefore, in order to more robustly characterize the electronic structure of the material additional measurements are carried such as absorption spectroscopy. From this the absorption coefficient and the index of refraction can be deduced. If coupled with the PL spectra, the exciton binding energy can also be calculated. In our reflection contrast measurements, a stable broadband tungsten-halogen lamp, which generates light from 300 - 2800 nm, is first spatially filtered with a pinhole and collimated with a pair of lens, see Figure 2.2. The collimated light from the lamp is then directed into a 100$\times$ objective lens and focused to a spot size of 2 - 3 μm. Similarly to the PL setup, the reflected light is then collimated by the same objective lens and sent into the spectrometer which integrates its spectrum over a period of time. Usually two different spectra are taken, one from the sample and the other from a thick transparent substrate. By subtracting the spectrum of the substrate from the spectrum of the sample on the substrate and normalizing the difference by the spectrum of the substrate, the differential reflection spectrum $\Delta R/R_{sub}$ can be determined. These spectrum normally identifies the different exciton

resonances of the 2D material.

If the sample is atomically thin, which is always true in 2D materials, and placed on a thick transparent substrate, such as quartz, the absorbance spectrum (A) can be determined from the differential reflection spectrum with

$$A = \frac{1}{4}(n^2 - 1)\,\frac{\Delta R}{R_{sub}}\,, \tag{2.1}$$

where n is the index of refraction of the substrate.[79] From the absorbance spectrum we can determine the percentage of incident light at given wavelength absorbed by the sample. To calculate the absorption coefficient, we use Beer-Lambert law defined as

$$I = I_0 e^{-\alpha d}\,, \tag{2.2}$$

where I is the transmittance intensity, I_0 is the incident optical intensity, d is the thickness of the material (in our case the thickness of the thin film in cm), and α is the absorption coefficient in units of 1/cm. By noting that the absorbance A is defined as the fraction of incident intensity absorbed, the absorption coefficient is calculated to be

$$\alpha = -\frac{\ln(1-A)}{d}\,. \tag{2.3}$$

Along with the PL technique, the absorption spectroscopy measurements are used to confirm the thickness of the sample as well as its optical properties.

2.3 Time Resolved Pump-Probe Spectroscopy

In Figure 2.3, the basic elements of a typical pump-probe setup are shown. The ultrafast laser systems consist of a Ti:Sapphire laser that generates 100-fs pulses, that can be tuned between 700 - 1080 nm, with an average power of about 2.0 W and a 80 MHz repetition rate. A small portion of this beam (10 - 20%) can directly be used as the probe beam or can either be sent to a beta barium

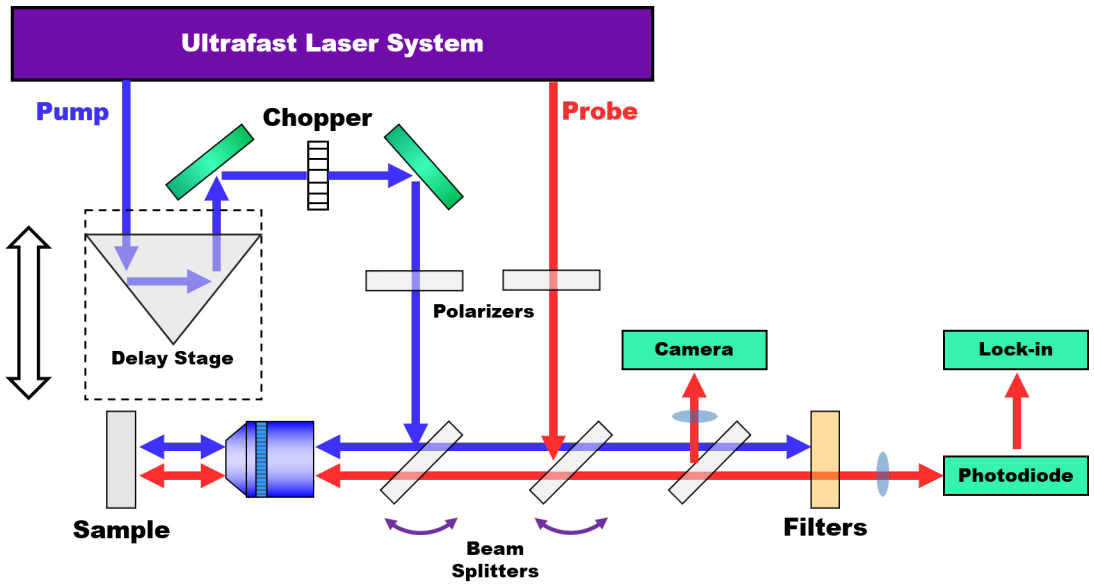

Figure 2.3: Typical pump-probe experimental setup in reflection geometry.

borate (BBO) crystal to generate its second harmonic. A set of filters is used right after the BBO to prevent the Ti:Sapphire beam from reaching the sample. The majority of the beam is sent either into a optical parametric oscillator, which outputs 130-fs pulses with wavelengths in the range 1.1 - 2.6 μm or is focus into a photonic-crystal fiber for supercontinuum generation, which outputs a broadband pulse. The output of the optical parametric oscillator can either be used directly or it can be sent into another BBO crystal to generate its second harmonic. The output of the photonic-crystal can be used as a pump or probe broadband pulse or it can be narrowed down with the used of a band-pass filter with a 10-nm bandwidth, in order to select the desired wavelength. Therefore, by using the Ti:Sapphire laser, the optical parametric oscillator, the photonic-crystal fiber, and BBO crystals, a wide range of wavelengths are available to study samples with different optical properties.

The configuration of the ultrafast-laser system depends on the sample being investigated. The selection of the pump and probe wavelength are chosen generally after the absorption and PL spectroscopy measurements are conducted. The results identify the excited states in the sample. In some cases, the pump and probe wavelengths are determined after a literature search of the material.

In our measurements, the pump beam, blue beam in Figure 2.3, is focused by an objective lens and is normally incident on the sample. The excited photocarriers generated by the pump pulse can either be electron-hole pairs or excitons, depending on the wavelength and sample.[80] Due to the presence of these photocarriers, the complex index of refraction of the sample is altered via various mechanisms such as the phase-space blocking effect due to the exclusion principle and the renormalization of the exciton orbital wavefunction due to the exchange effect and long-range Coulomb effect.[81] These effects provide a convenient way to probe the presence of photocarriers.

The probe pulse, red beam in Figure 2.3, is aligned so that it propagates along with the pump beam and is focused on the sample with the same objective lens. By tuning the probe beam to the resonance of the material or higher, the presence of photocarriers can be sense by measuring the normalized change in the probe's reflection, $\Delta R/R_0 = (R-R_0)/R_0$, typically referred as differential reflection. Here, R is the reflection of the probe beam in the presence of the pump and R_0 is the reflection of the probe without the pump. The pump is prevented from reaching the photodiode with a set of filters. The lock-in technique is used to detect the differential reflection signal $\Delta R/R_0$. This requires that the pump beam is modulated with a mechanical chopper at a given frequency, typically in KHz in our experiments, while the output of the photodiode is sent into the lock-in amplifier. Mathematically, this consist of integrating the product of the probe's signal, which is indirectly modulated by the pump beam, and a periodic reference signal with the same modulation frequency. The integration limits are taken to be from time $t = 0$ up to $t = t_{\text{int}}$, where t_{int} is large when compared to the period determined by the modulation frequency. The result of this operation is then normalized by the integration time t_{int}. Since the probe beam is being indirectly modulated at the same frequency the pump beam is being chopped, the signal the probe beam generates at the photodiode is a periodic square wave which can be decompose by taking its Fourier transform. If one carries along this operation, it can be shown that the output of the lock-in detector is proportional to $(R-R_0)$. Hence, the lock-in measures a voltage that is proportional to ΔR. To obtain R_0, the pump beam is blocked and the probe beam is modulated (with the same frequency) and detected by the lock-in. Using the same mathematical operations, but this time with the probe

signal being modulated directly with the chopper, the output of the lock-in is proportional R_0. Both the proportionality constants for $(R - R_0)$ and R_0 are the same, hence dividing them results in the normalized differential reflection $\Delta R/R_0$. When the samples are optically thin and placed on a transparent substrate, one can also measure the differential transmission defined as $\Delta T/T_0$. For relatively thick samples, different aspects of the photocarrier dynamics are revealed by the differential reflection and the differential transmission, since the reflection is more sensitive to the surface. However, our samples are always atomically thin therefore the difference between the two techniques is minor.

To obtain the time-dynamics of the photocarriers, the differential reflection (or transmission) is measured as function of probe delay, defined as the arrival time of the probe to the sample relative to the pump's arrival. The delay of the probe can be precisely controlled by sending either the pump or probe into a retroreflector placed on a motorized linear stage, see Figure 2.3. The position of the retroreflector can precisely be chosen along the linear stage with the aid of a computer; hence, allowing us to change the path length and consequently the arrival time of the probe beam with respect to the pump's arrival. Zero delay is defined as the simultaneous arrival of the pump and probe beam to the sample. A probe beam that arrives before the pump has a negative arrival time whereas a probe beam that arrives after the pump a positive arrival time. After the initial alignment of the beams, the relative position of the pump and probe beams, which are observed with a camera system that also images the sample surface, are each controlled with beamsplitters equipped with motorized screws. As is shown in Figure 2.3, both the pump and probe beam co-propagate, are normally incident on the sample and focused. The reflected beams from the sample are then collected and collimated by the same objective lens, a fraction of this beams are sent to the camera imaging system, and the unwanted pump beam is stopped from reaching the photodiode with a set of filters.

The differential reflection signal, measured as a function of probe delay, obtained from a WSe_2 ML at room temperature is shown in Figure 2.4. Here, the pump and probe energies are 2.0 and 1.65 eV, respectively. It displays the evolution of the photocarrier population that was injected by

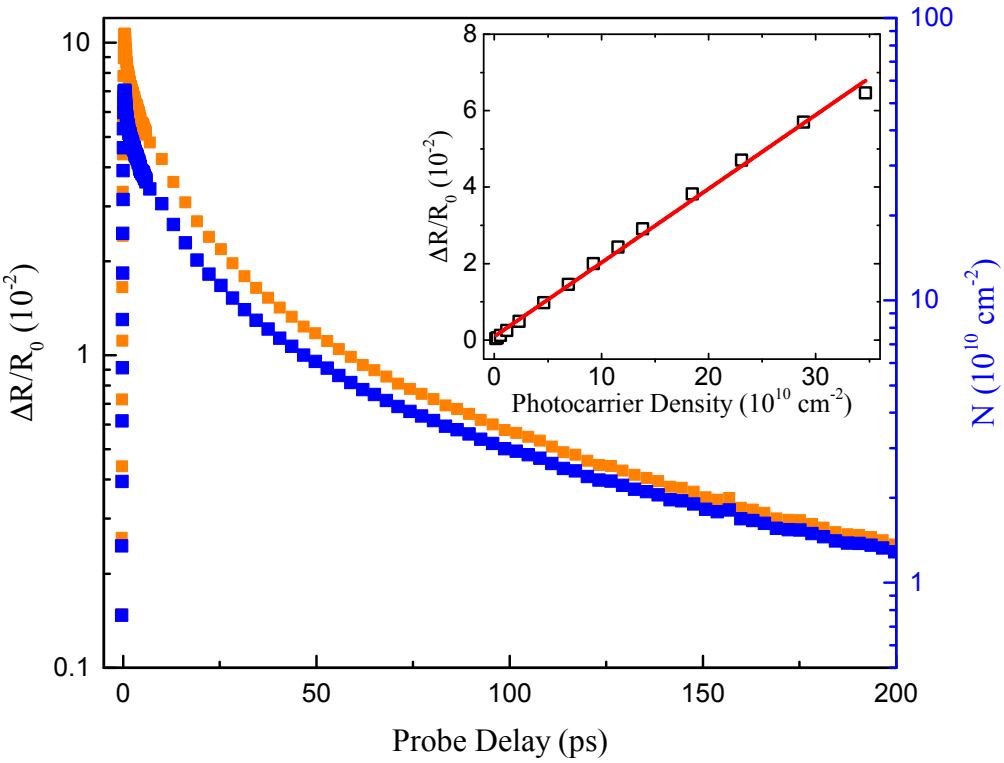

Figure 2.4: The orange symbols represent an example of the differential reflection obtained from a WSe_2 monolayer (ML). The black squares in the inset shows the relation between the signal and the exciton density. The solid red line is a linear fit to the data. Such an experimentally established relation is used to convert the measured signal to the exciton density (the blue symbols).

the pump at 0 ps.

In order to use the differential reflection (or transmission) signal to reflect the photocarrier population, a relationship between the injected carrier density and the signal needs to first be established. This is always first done experimentally by measuring the signal shortly after zero probe delay as a function of pump fluence. If the thickness and the absorption coefficient at the pump's wavelength of the material are known, these can then be used to calculate the initial photocarrier density from the pump fluence, see Appendix B. The inset of Figure 2.4 shows these results for the WSe_2 ML. Such an experimentally established relation is used to convert the measured signal to the photocarrier density, blue symbols in Figure 2.4. This relation can also be obtained from a well established non-linear optical effect known as saturable absorption.[82]

Since the number of available excited states is fixed at a given energy, the absorption of the material will be reduced as more excited states are occupied. In this model, the absorption coefficient, α, is described as a function of the photocarrier density N by

$$\alpha(N) = \frac{\alpha_0}{1+\frac{N}{N_{sat}}}, \tag{2.4}$$

where α_0 is the absorption coefficient when no photocarriers are present ($N = 0$) and N_{sat} is the photocarrier density that causes the absorption coefficient to decrease by 50%.[82] The change in absorption due to the presence of photocarriers with density N can now be calculate it as

$$\Delta\alpha = \alpha(N) - \alpha(0) = \alpha_0 \left[\left(1 + \frac{N}{N_{sat}} \right)^{-1} - 1 \right]. \tag{2.5}$$

For photocarriers densities that are much smaller than N_{sat}, that is $N \ll N_{sat}$, we can use Taylor's approximation for $\Delta\alpha$ and obtain

$$\Delta\alpha \approx -\frac{\alpha_0}{N_{sat}} N \qquad \rightarrow \qquad \frac{\Delta\alpha}{\alpha_0} = \frac{N}{N_{sat}}. \tag{2.6}$$

From equation 2.6, we can see that the change in absorption caused by the pump is directly propor-

tional to the photocarrier density N. In our experiments, we do not directly measure the change in absorption but instead we monitor the change of reflection or transmission of the probe beam. For the sake of simplicity, we would derive this relation for the change in transmission and will note that for our 2D samples, the change in reflection will require us to take into account the multiple reflections that are caused by the different interfaces. However, since the absorption coefficient from the substrates we use [Si, SiO_2, and polydimethylsiloxane (PDMS)] at the wavelengths our experiments were conducted are practically zero, we can safely assume that any change in the reflection is solely caused by the sample. To formulate the relation between $\Delta\alpha$ and ΔT, we use Beer's Law, which established the transmittance, T, through a sample with thickness d and absorption coefficient α as $T = e^{-\alpha d}$. Consequently, the difference in transmission caused by a photocarrier population N is

$$\Delta T = T(N) - T(0) = e^{-\alpha(N)d} - e^{-\alpha_0 d}. \tag{2.7}$$

By normalizing equation 2.7 by the transmission of the probe beam without the presence of photocarriers T_0 and assuming that $\alpha d \ll 1$, which is usually true in our experiments, equation 2.7 can be approximated to be

$$\frac{\Delta T(N)}{T_0} \approx -\Delta\alpha d. \tag{2.8}$$

Therefore, by measuring $\frac{\Delta T}{T_0}$, we are indirectly measuring the change in the reflection coefficient $\Delta\alpha$, which is cause by the presence of photocarriers with density N. By putting equation 2.6 and equation 2.8 together, we then have

$$\frac{\Delta T}{T_0} \approx -\Delta\alpha d \qquad \leftrightarrow \qquad \frac{\Delta\alpha}{\alpha_0} = \frac{N}{N_{sat}} \tag{2.9}$$

From here, we can conclude that by measuring the differential transmission, we are indirectly measuring the change in the absorption coefficient caused by the population of photocarriers injected by the pump. Moreover, equation 2.9 illustrates that a linear relationship exists between the signal and the photocarrier density. This is confirmed by our experiment, see inset of Figure 2.4. The significance of these results are that the signal (either the differential reflection or transmission) can

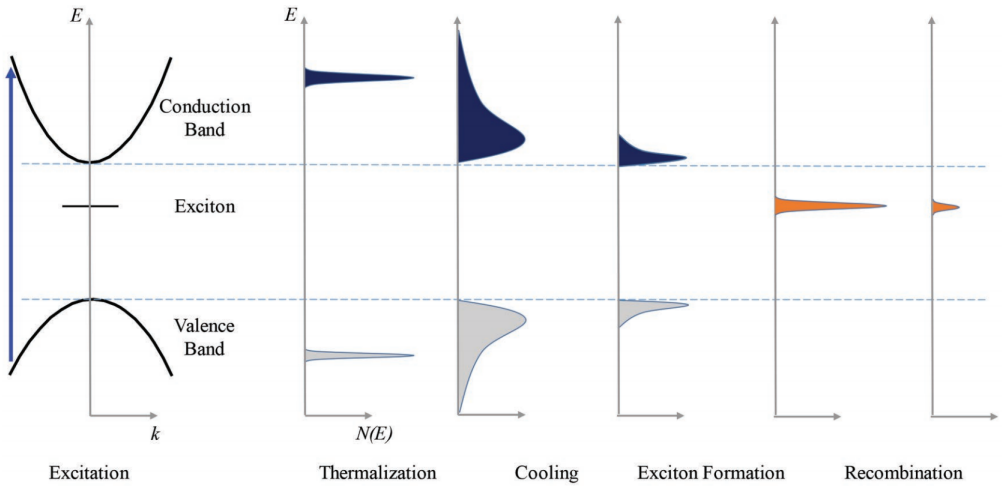

Figure 2.5: The evolution of photocarriers after instantaneous interband excitation. Reproduced with permission.[78] Copyright 2016, Advanced Functional Materials.

be used to monitor the population of photocarriers. The decay of this signal can therefore be used to study the carier dynamics in a quantitative way. In most measurements, the injected density was kept much lower than N_{sat}. In such a linear regime, the signal is proportional to the photocarrier density.

2.4 Time-Domain Photocarrier Dynamics

To understand the origin of the signal shown in Figure 2.4, we need to analyze all physical processes and the time scales that they occur in order to correctly interpret the data. Figure 2.5 shows the typical life cycle of photocarriers in semiconductors.[83] The interband excitation, a result of of pump photoexcitation, produces a nonthermal distribution of electrons and holes. Shortly after, a thermalization process evolves the initial nonthermal distribution into a thermal one, where the electron and hole temperatures are higher than the lattice temperature. Consequently, energy relaxation (cooling) brings the photocarrier system into a quasi-equilibrium state with the phonon system, sharing the same temperature. The free carriers can then form excitons, which can then recombine radiatively or nonradiatively, returning the system to the equilibrium state before the photoexcitation. These processes are not necessarily separated in time. For example, recombi-

nation can occur with hot carriers and the cooling process can occur during the thermalization process.

2.4.1 Thermalization and Energy Relaxation

The initial form of the photocarrier's energy distribution is determined by the pump pulse. When the pump pulse is tuned to the exciton resonance, excitons are directly injected. On the other hand, for interband excitation, the initially injected electrons and holes have Gaussians distributions, which is dictated by the pump spectrum. These extremely nonthermal carriers quickly develop a thermal distribution via both carrier-carrier and carrier-phonon scattering, in a process known as thermalization. Since the redistribution of energy among the carriers is mainly achieved by carrier-carrier scattering, this process is expected to be very fast in 2D materials with an enhanced Coulomb interaction due to the reduced screening that occurs due to dimensionality.

By using a 10-fs time resolution, the ultrafast carrier thermalization and cooling processes were studied in few-layer MoS_2 by Nie et al.,[84] as shown in Figure 2.6. The researchers observed a nonthermal distribution immediately after the pump's photoexcitation and discovered that the thermalization process occurs within 20 fs. Their interpretation that the thermalization occurs via both by carrier-carrier and carrier-phonon scattering is supported by the measured dependence of the thermalization time with the carrier density and temperature of the sample. After the thermalization process, they observed that the cooling of the hot Fermi-Dirac distribution happens in a 0.6 ps time scale via carrier-phonon scattering. Their experimental results are consistent with nonadiabatic ab initio molecular dynamics simulations, which predict carrier-carrier and carrier-phonon scattering time scales of 40 fs and 0.5 ps, respectively.

These time scales are significantly shorter than those in conventional semiconductors which illustrates the enhanced carrier-carrier and carrier-phonon scattering that occurs in 2D semiconductors.[83]

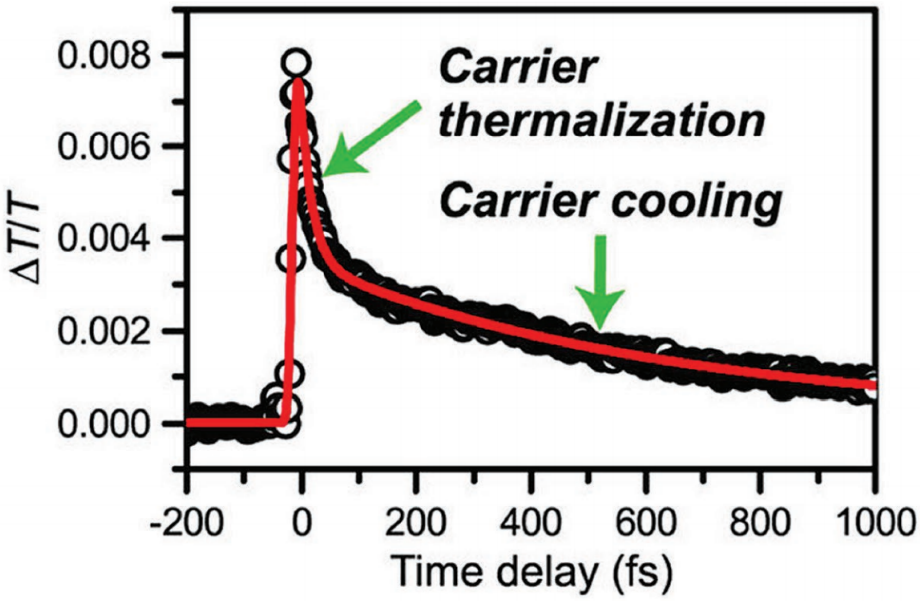

Figure 2.6: Thermalization and energy relaxation of photocarriers in few-layer MoS_2. Two different relaxation processes can be identified and their physical origins are attributed to carrier thermalization that occurs within the first 20 fs mainly via carrier-carrier scattering and carrier cooling that occurs via carrier-phonon scattering and lasts about 0.6 ps. Reproduced with permission.[84] Copyright 2014, American Chemical Society.

2.4.2 Exciton Formation

One of the key differences between 2D and conventional 3D semiconductors is the exceptionally large exciton binding energies on the order of several hundred millielectronvolts that have been revealed in monolayers of MoS_2,[85–87] WS_2,[86–88] $MoSe_2$,[86,89] and WSe_2.[29,86] The large exciton binding energies are a result of the reduced electric field screening that occurs in two dimensions which in turn enhances the electron-electron interactions. This gives rise to excitons that are stable at room temperature and dominate the optical properties of 2D materials.

The exciton formation process in 2D materials, namely in TMDs, was studied by Ceballos et al.[80] After interband excitation, the injected photocarriers thermalize and form a hot Fermi-Dirac distribution that is cooled down via carrier-phonon scattering, as discussed in the previous section. It was found that after the injection of free electron-hole pairs, two different time scales were observed in the decay of the differential reflection signal generated from ML $MoSe_2$ at room temperature, as shown in Figure 2.7(a). The decay of the signal was measured as a function of

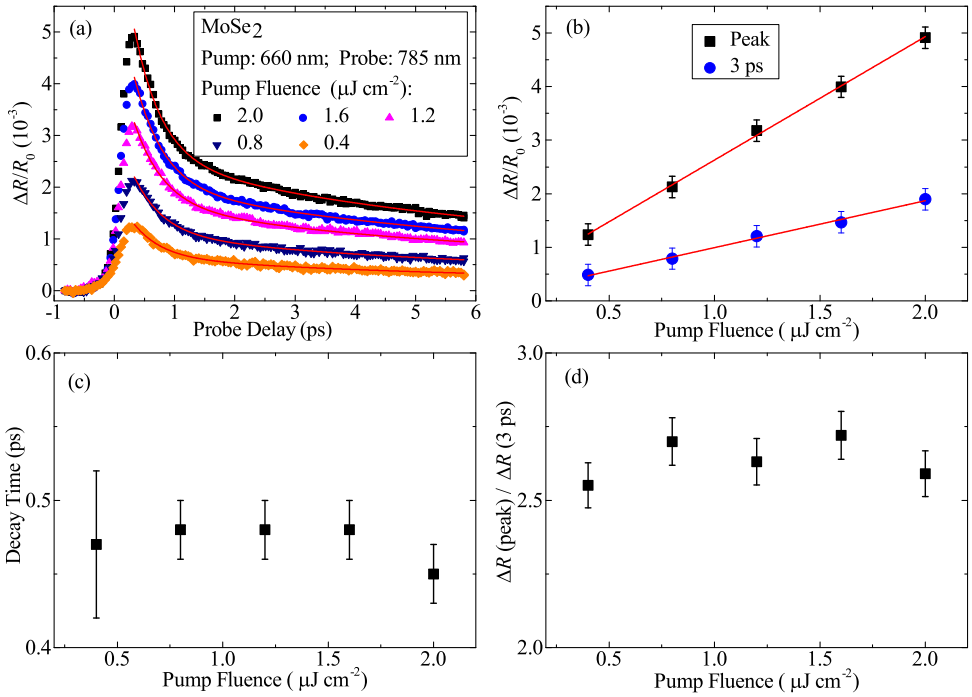

Figure 2.7: (a) The differential reflection signal from ML $MoSe_2$ measured at different pump fluences. The pump and probe wavelengths as well as the pump fluence are noted in the legend. (b) The peak differential reflection and the signal at 3 ps measured as a function of pump fluence. (c) From the bi-exponential fits (shown as the red curves in (a)), the fast decay constants are extracted and plotted as a function of pump fluence. (d) The relative strength of the fast decay component measured as a function of pump fluence. No dependence is observed in either the fast decay constant or the relative strength of the fast decay with the pump fluence. Reproduced by permission from The Royal Society of Chemistry.[80]

pump fluence, shown in Figure 2.7(b), and fitted bi-exponential functions to the signals shown in 2.7(a). The extracted short decay constants, that characterize the fast decay, were then plotted as a function of pump fluence and show no dependence, Figure 2.7(c). To measure the strength of the fast decay component the quantity $\Delta R(\text{peak})/R(3\text{ ps})$ was computed which is simply the ratio of the peak signal and the signal at 3 ps. This quantity showed no dependence with pump fluence, see Figure 2.7(d). Finally, by measuring $\Delta R(\text{peak})/R(3\text{ ps})$ as function of the pump photon energy, while keeping the initial injected photocarrier density constant, it was observed that the strength of the fast decay component decreased as the pump photon energy approached the A exciton resonance and in some cases was virtually absent. Since the excitons are less efficient than free carriers in inducing a transient absorption signal, the rapid decay of the signal was attributed to formation of excitons from free electrons-electrons hole pairs. Such a decay process lasted between 0.3 to 0.5 ps for MoS_2, WS_2, $MoSe_2$, and WSe_2 MLs. This interpretation is supported by the fact that when the pump energy was tune close to the A exciton resonance, that is when excitons are directly injected as oppose to free electron-hole pairs, the fast decay component was absent in the signal. Although other mechanisms, such as the lost of the photocarriers population to defect trapping, can also induce a fast decay of the transient absorption signal, further evidence showed that in this study there is no rapid loss of the carrier population to defects. These experimental results, are consistent with a theoretical study[90] showing that the exciton formation process can be shorter than 1 ps and generated via a longitudinal optical phonon-assisted scattering process. In a recent report, the exciton formation in a ML of WSe_2 was observed to occur in a subpicosecond timescale by using a time-resolved THz spectroscopy technique.[91]

2.4.3 Exciton-Exciton Annihilation

As the exciton population forms, it immediately starts to decay due to electron-hole recombination. This process can be radiative, where the energy is released in a form of a photon, or nonradiative, accompanied by other forms of excitations, such as phonon generation or intraband excitation of carriers.

It was found that with high exciton densities of above 10^{11} cm^{-2}, the decay of the exciton population in TMD MLs is a bimolecular process that depends on the exciton density. This phenomenon is attributed to exciton–exciton annihilation, which has been widely observed in systems with strong exciton–exciton interactions, such as organic molecules[92,93] and carbon nanotubes.[94,95]

With the contribution of exciton–exciton annihilation, the decay of the exciton density N can be written as

$$\frac{\mathrm{d}N}{\mathrm{d}t} = \frac{1}{\tau}N - \frac{1}{2}\gamma N^2, \tag{2.10}$$

where τ and γ are the exciton lifetime and the exciton annihilation, respectively.[95] At very early times when $t \ll \tau$, the first term in the right hand side of the equation can be ignored and by solving for the exciton density N it can be shown that

$$\frac{N_0}{N(t)} - 1 = \gamma N_0 t, \tag{2.11}$$

where N_0 is the initial exciton density.

Figure 2.8 shows the observation of the exciton-exciton annihilation in ML $MoSe_2$.[96] The evolution of the carrier density as a function of probe delay is shown in the left panels. As it can be seen, a fast decay component starts to develop and becomes stronger as the initial carrier density is increased. From the data in the left panels, the quantity $[N_0/N(t)] - 1$ is calculated and plotted on the right column. The initial part of the dynamics can be described by this model. From the linear fits (solid red line) the annihilation rate is found to be $\gamma = 0.33 \pm 0.06$ cm^2 s^{-1}. Exciton–exciton annihilation has also been observed in MoS_2,[97] WS_2,[98] and WSe_2 MLs.[99]

2.4.4 Exciton Recombination

At lower injected photocarrier densities or later decay times, the decay of the exciton density is less affected by exciton–exciton annihilation. The lifetimes of the electrons-hole recombination are critical for TMDs photoelectronic applications; however, the recombination mechanisms are complex and depend on the experimental conditions and the sample being investigated. To develop

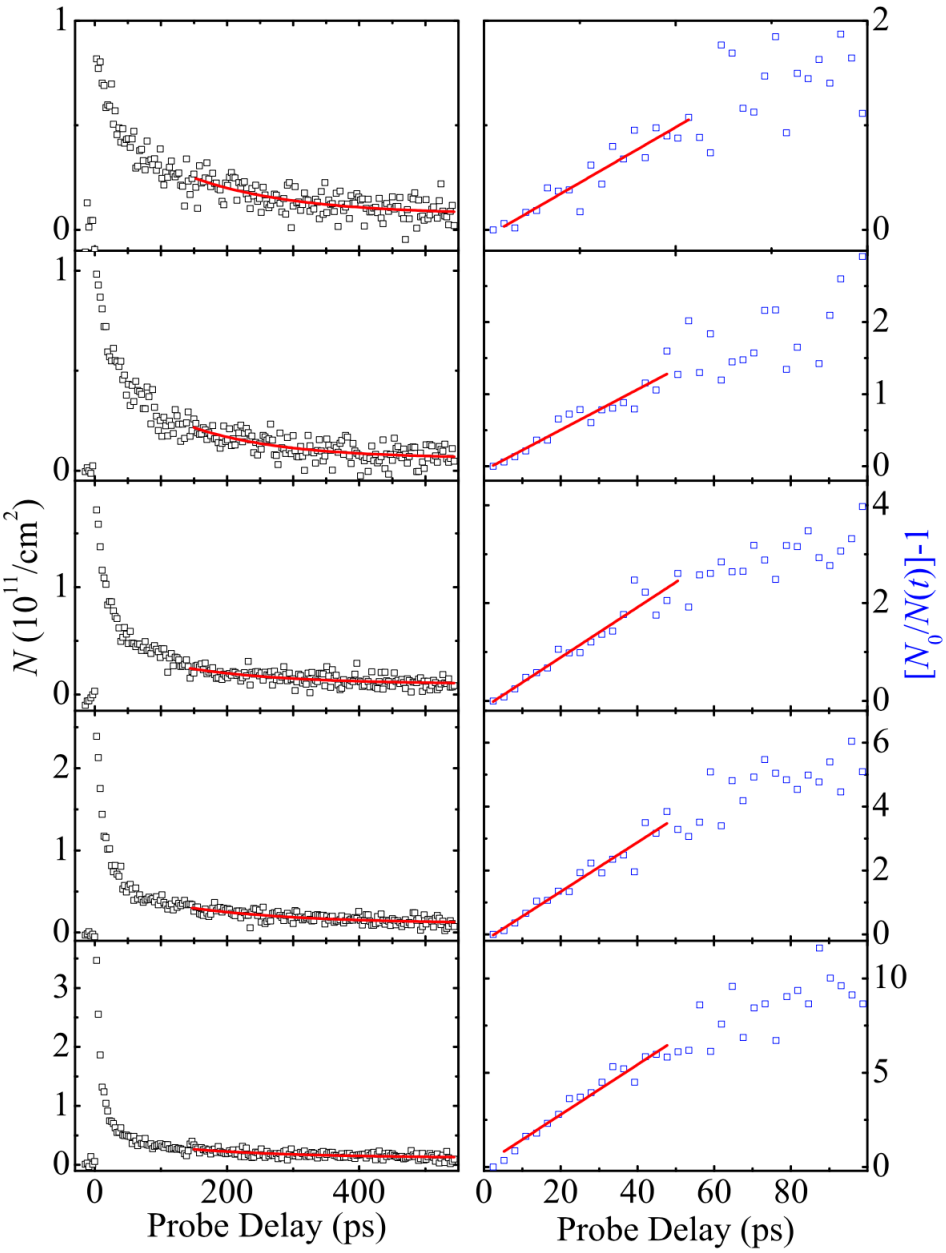

Figure 2.8: Left column: Exciton density as a function of probe delay for various initial injected densities. At times scales shorter than 100 ps, a fast decay component starts to develop as the initial exciton density increases. The red solid curves are single exponential fits to the data after 150 ps. Right column: The quantity $N_0/N(t) - 1$ is calculated from the data in the left panels as function of the probe delay. The red lines are linear fits. Reprinted with permission.[96] Copyright 2014, American Physical Society.

a better understanding of the ultrafast dynamics of the photoexcited carriers optical pump-probe studies as well as time-resolved photoluminescence (TRPL) measurements have been conducted in TMDs MLs.

In the transient absorption spectroscopy studies with 100-fs time resolution (using orthogonal pump-probe polarizations), the differential reflection signal $\Delta R/R_0$ is observed to reach its maximum value in an ultrafast timescale (< 500 fs). This interpreted as the excitation, thermalization, and relaxation of photoexcited carriers.[84,100,101] The $\Delta R/R_0$ signal then exponentially decays with different time scales depending on the experimental conditions in which the experiments were carried. At low injected densities or later decay times, a single exponential function is enough to satisfactorily fit the $\Delta R/R_0$ signal where the exponential decay time (lasting hundreths of ps) is simply attributed to the electron-hole recombination lifetime.[97,102] Furthermore, in a different study in which the probe pulse is tuned close to the A exciton resonance, the excited state population decays in three distinct time scales in where the 2 - 4 ps fast decay is attributed to the trapping of excitons by surface trap states, the intermediate decay of 30-80 ps is associated with interband carrier-phonon scattering, and the slow decay component of 300-1000 ps is assigned to the direct interband electron-hole recombination.[101]

To further investigate the exciton emission dynamics, temperature dependent steady-state PL and TRPL experiments have been carried. The TRPL study by Yuan and Huang[98] on a WS_2 monolayer reports that the PL lifetime, obtained by integrating in time the entire PL spectra and fitting it with a single exponential function, is 806 ± 37 ps. The authors point out that the single exponential decay as well as the high PL yield is the result of the PL originating from a single state showing that the number of defects in WS_2 is low. In contrast, two TRPL studies on WSe_2[103] and MoS_2[104] MLs show that two distinct temporal regions arise in the PL decay. In the WSe_2 study it is noted that the low temperature steady-state WSe_2 PL spectra shows that trion and exciton emission spectrally overlap each other over the investigated temperatures. By analogy of the shorter trion lifetimes when compared to the excitons found in GaAs quantum wells the authors assigned short (long) lived component that evolves from 20 (70) to 60 (250) ps in the temperature

range of 130 to 260 K to the trion (exciton) radiative decay. Conversely, in the MoS_2 study the short decay occurring over the first few picoseconds is ascribed to the exciton lifetime while the long lived component that arises at temperatures higher than 150 K is related to an exciton-phonon scattering process. The discrepancies that exists among different techniques more likely arise from the defects in the samples.

Different from the defect-limited lifetimes, the intrinsic exciton lifetime describes the radiative recombination of excitons in ideal samples. The radiative lifetime of excitons with small in-plane momenta (within the light cone) in WSe_2 MLs was found to be shorter than 0.2 ps by time-resolved mid-infrared measurements[99] and optical two-dimensional Fourier transform spectroscopy.[105] Wang et al. developed a model that produced results of radiative lifetimes that are in excellent agreement with these experimental results.[106] The model also shows that thermalized exciton populations have lifetimes much longer than the radiative lifetime, since the majority of the population is out of the light cone

2.5 Spatially Resolved Pump-Probe Spectroscopy

The measurements in Figure 2.4, reveal the time-domain carrier dynamics, however, the power of the pump-probe technique is fully unleashed when combined with additional knobs. For example, adding spatial resolution, which is usually accomplished with beam splitters that are equipped with picomotor piezo linear actuators that provide exceptional motorized fine positioning of the beams (as shown in Figure 2.3), when coupled with ultrahigh time resolution can reveal the diffusion of photocarriers in 2D materials. In this section, recent studies of exciton diffusion in 2D semiconductors achieved by introducing high spatial resolution will be discussed.

2.5.1 Photocarrier Diffusion

The principle of spatially resolved pump-probe spectroscopy is shown in schematically in Figure 2.9. Here, a tightly focus pump beam (blue in the figure) injects photocarriers with a thin

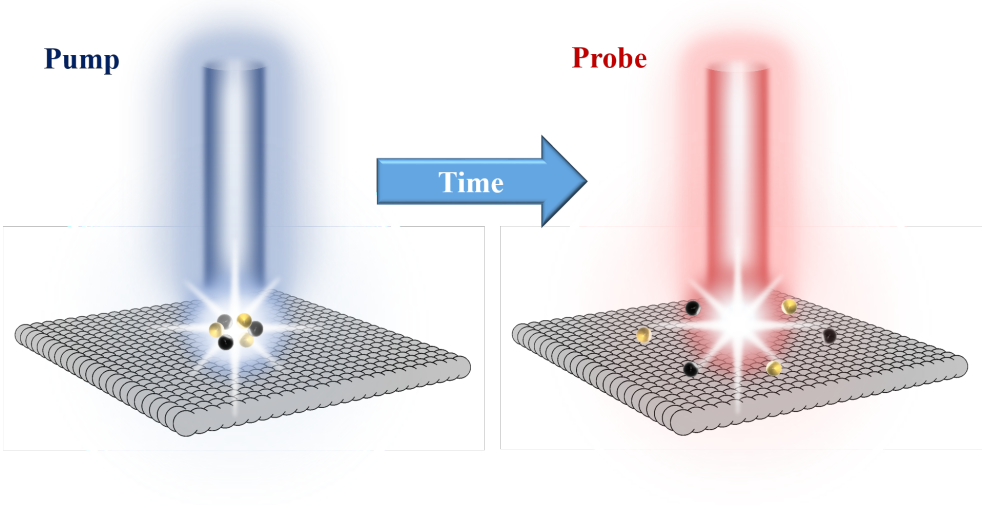

Figure 2.9: Schematic representation of transient absorption microscopy measurements of exciton diffusion in 2D semiconductors. A tightly focused pump pulse (blue beam) injects photocarriers and at a later time a probe pulse (red beam) monitors their spatial profile.

Gaussian spatial profile (same as the beam). The lateral size of the initial distribution can be characterize by its full width at half maximum, w_0, and ranges typically from 1 to 2 μm. The evolution of the Gaussian profile is then driven by the in-plane density gradient which causes the photocarriers to diffuse in the sample, where the profile remains a Gaussian but with a width w that expands.[107] The diffusion equation for a density $N(r,t)$ is

$$\frac{\partial N}{\partial t} = -\frac{N}{\tau} + D\nabla^2 N, \tag{2.12}$$

where D is the diffusion coefficient and τ the photocarrier lifetime. By assuming that the diffusion constant and the photocarrier lifetime are independent, the solution to this equation is found to be

$$N(r,t) = \frac{1}{4\pi Dt} \cdot e^{-r^2/4Dt} \cdot e^{-t/\tau}, \tag{2.13}$$

where the profile's squared width increases linearly with time t as

$$w^2(t) = w_0^2 + 16\ln(2)Dt, \tag{2.14}$$

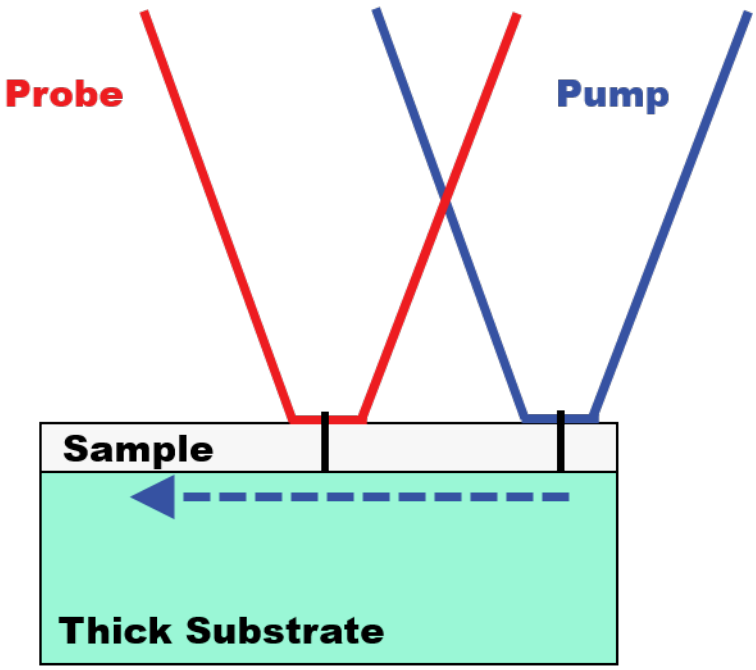

Figure 2.10: Schematic illustration depicting the imaging process of the photoexcited carriers where a pump pulse is scanned relative to a fixed probe beam.

where w_0^2 is the initial width at $t = 0$. The probe pulse (red beam in Figure 2.9) arriving at a later time acquires the spatial profile at that time. In our measurements, this achieved by measuring the differential reflection or transmission as a function of the distance between the pump and the probe spots, schematically depicted in Figure 2.10.

An example of such measurement is shown in Figure 2.11, which was carried on a 20-layer exfoliated black phosphorus film.[108] Here, the differential reflection, with a 1.70-eV pump and 1.53-eV probe, is plotted as function of probe delay and relative probe position in Figure 2.11(a). To demonstrate that at later times the exciton density maintains a Gaussian profile several spatial profiles at different times are shown in Figure 2.11(b). Finally, the spatial profiles are fitted with Gaussian curves, shown as the solid lines in Figure 2.11(b), and the squared widths are extracted and plotted as a function of probe delay in Figure 2.11(c). According to equation 2.14, the slope of the data will contain the diffusion coefficient D. Therefore, by fitting a line and extracting the slope, shown as red solid curve in Figure 2.11(c), a diffusion coefficient $1,300 \pm 30$ cm^2 s^{-1} is determined.

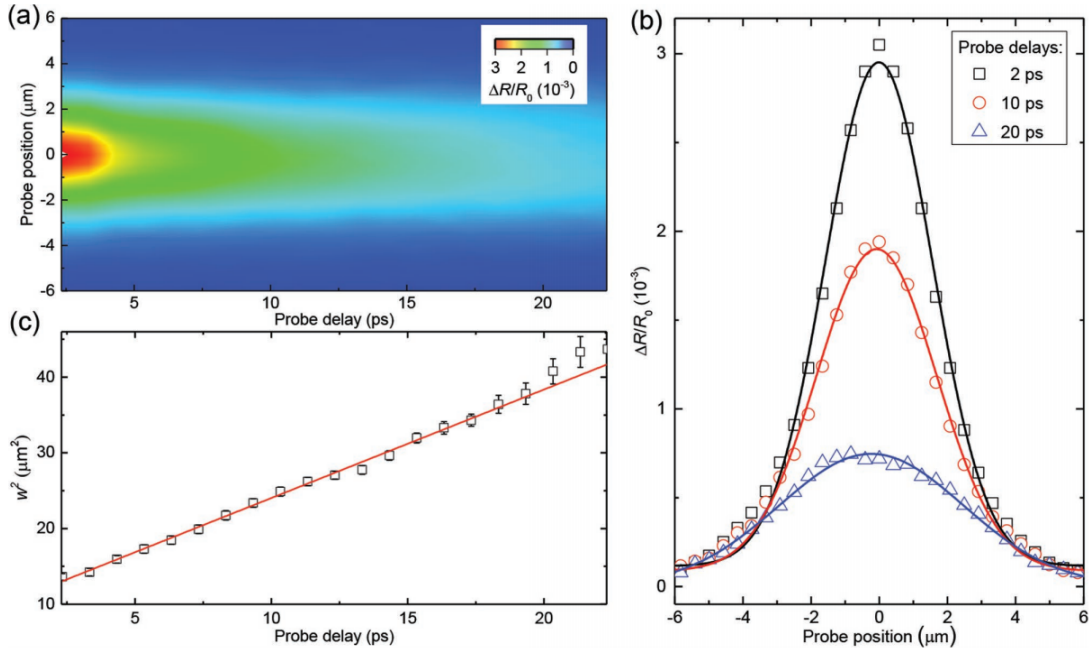

Figure 2.11: (a) The differential reflection from a 20-layer black phosphorus film measured as function of probe delay and relative probe position. This measurement was obtained by scanning the probe spot relative to the fixed pump spot along the armchair direction for different probe delays. (b) Examples of the spatial profiles at different probe delays. The solid lines are Gaussian fits. (c) From the Gaussian fits shown in (b) and others not shown, the square width of the profile is extracted and plotted as function of probe delay (black squares). The solid red line is a linear fit to the data and displays the linear evolution of the width squared. Reprinted with permission.[108] Copyright 2015, American Chemical Society.

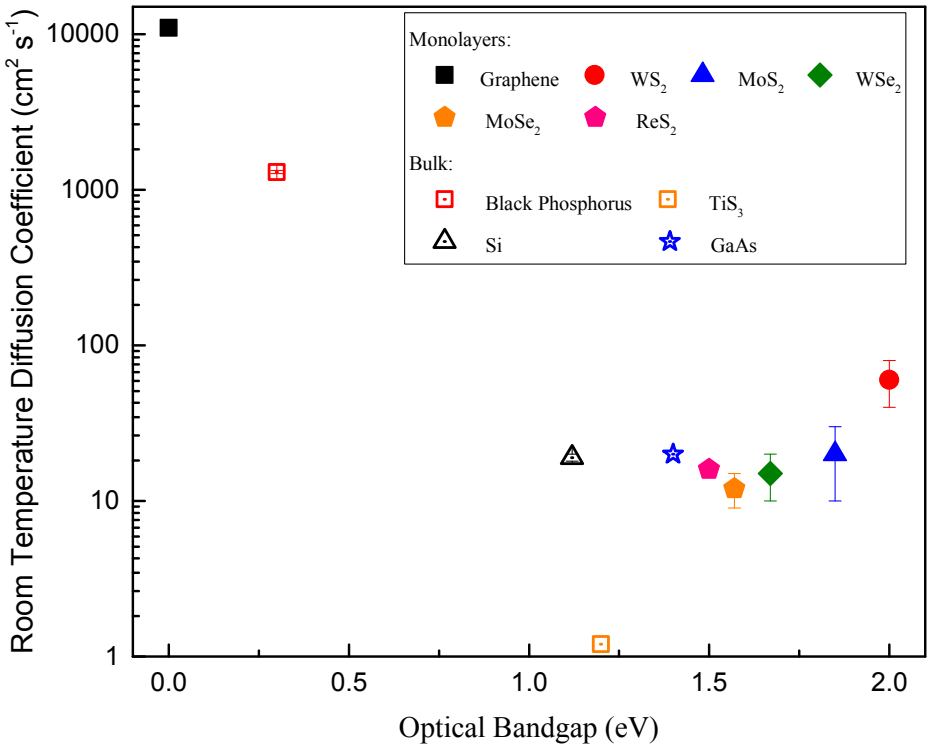

Figure 2.12: Summary of known exciton and electron-hole pairs diffusion coefficients at room temperature for several 2D materials (solid symbols) and bulk materials (open symbols).[102,108–116] Reproduced with permission.[78] Copyright 2016, Advanced Functional Materials.

This same approach has been used to study the exciton or electron-hole pair diffusion in other 2D materials.[102,108–116] The results are summarized in Figure 2.12 where the measured coefficients are plot it against the optical bandgap of the materials. The 2D semiconductors have their diffusion coefficients in the range of 10 to 50 cm^2 s^{-1}, which are comparable to the 3D conventional semiconductors such as Si and GaAs. However, graphene and bulk black phosphorus show diffusion coefficients that are several orders of magnitude larger than those of the reported 2D semiconductors.

In order to deduce the diffusion coefficients using equation 2.14, two conditions must be met. First, the transient absorption signal must be proportional to the carrier density otherwise the measured spatial profile won't represent the true spatial profile of the density. Second, the recombina-

tion time should be independent of the carrier density else the decay of the photocarriers in different parts of the spatial profile will decay at different rates making more difficult to determined the true spatial profile of the samples. This will cause the true spatial profile of the density to deviate from being a Gaussian distribution and the change of the width will be unrelated to the diffusion. These conditions are usually verified experimentally by measuring the transient absorption signal as function of injected carrier density. By fitting the different curves with the appropriate functions the extracted carrier lifetimes can be plot it as a function of injected carrier density. An example of these procedure is shown in Figure2.7(a) and (c). Once it is verified that the carrier lifetime does not depend on the carrier density the signal shortly after zero probe delay is plot it as a function of the injected carrier density, as shown in the inset of Figure 2.4. The spatially resolved pump-probe measurement is then carried at density where the signal scales linearly with the injected carrier density.

Chapter 3

Vertically Stacked Two-dimensional Multilayer Structures

The structure of this section is organized by the complexity of the samples. Our experimental results on bilayer heterostructures are first discussed which stimulated and encouraged the investigation of more complex multilayer structures. Consequently, we fabricated a three-layer and four-layer samples with the purpose of controlling the charge dynamics by the sequence we ordered the layers. All the multilayer samples discussed in this section were fabricated by stacking semiconducting TMDs exfoliated monolayers. The photocarrier dynamics in the monolayers and the multilayer samples as well as the interlayer interactions were optically characterized with non-destructive techniques, such as photoluminescence, absorption, and transient absorption (pump–probe) spectroscopy. With these, we demonstrate the electronic and optical properties of multilayer structures that can help improve their fabrication and design; moreover, it has encouraged the fabrication of 2D multilayer samples that are put together by chemical means.

3.1 Extended Photocarrier Lifetimes and Charge Transfer Exciton Formation in a MoS_2–$MoSe_2$ Bilayer Heterostructure

We report on the time-resolved photocarrier dynamics and formation of charge transfer excitons in a bilayer heterostructure formed with $MoSe_2$ and MoS_2 exfoliated semiconducting TMDs MLs. By selectively injecting photocarriers in one of the layers and probing the exciton states of the other layer, we establish that electrons and hole transfer to the lower energy side of the heterostructure on a subpicosecond time scale. The transferred electrons and holes very quickly form charge transfer excitons, with electrons and holes residing in different layers of the heterostructure. It is discovered that the charge transfer excitons have longer recombination lifetimes when compared to excitons in the individual MLs. Most results in this section were published in ACS Nano.[45]

3.1.1 Experimental Results and Discussion

For several decades, multilayer structures formed with different 3D materials have been the cornerstone for developing functional materials with tunable properties.[72–74] Traditionally, such conventional structures are fabricated by epitaxy techniques that require that the component materials have a closely matching lattice. This restriction limits the number of component materials that can successfully be put together where oftentimes a poor interface is the result of a slight lattice mismatch. With the undeniable success that graphene brought to the 2D world and its substrate dependance properties, soon 2D multilayer structures using graphene and hexagonal boron nitride (hBN) were extensively studied.[8] Encourage by the results that showed that graphene devices on hBN substrates had improved mobilities and carrier inhomogeneities by up to an order of magnitude when compared to graphene devices on SiO_2, multilayer structures composed with 2D materials other than graphene and hBN started to be realized. Since what keeps together 2D multilayer structures is the weak van der Waals force (which acts like glue between the layers) the lattice matching restriction is greatly relaxed. This opens up a new avenue where a huge number of combinations can be designed and explored,[117] where the only limitation is the stability of the 2D material. The

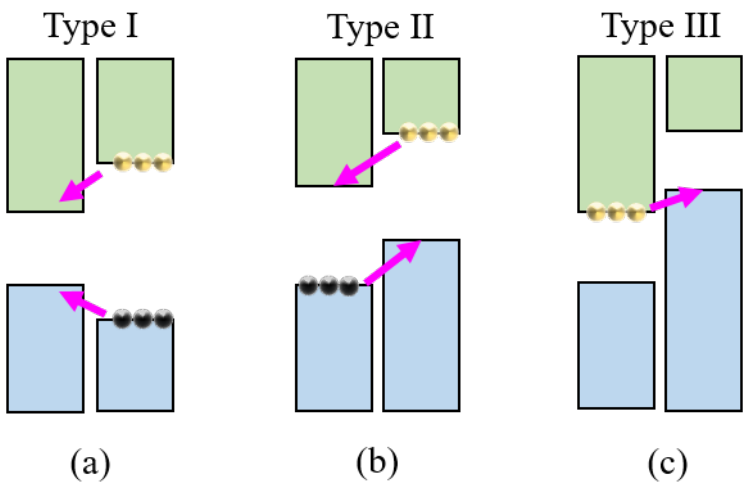

Figure 3.1: Schematic illustrations of Type I, II, and III band alignment in bilayer heterostructures. The valence (conduction) bands are indicated by the green (blue) color. The direction of the electron and hole flow are denoted by the pink arrows.

interface can be atomically sharp and the junction region as thin as two atomic layers.[118] Moreover, the van der Waals multilayers are flexible and their fabrication is compatible with current thin technologies.

When two different semiconducting materials are brought together, three different types of band alignments can be formed, for example, type I (symmetric), type II (staggered), or type III (broken), as illustrated in Figure 3.1. Depending on the type of the desired application, different types of band alignments are used. For example, for light emitting diodes and in lasers, a type I band alignment is more advantageous since electrons and holes can be confined into one layer for more efficient electron-hole recombination. By sandwiching an undoped semiconductor, such as GaAs, between a p-type and n-type semiconductor, such as AlGaAs, a quantum well can be formed, see Figure 3.2. Quantum wells are an extension of type I band alignments where electrons and holes are generated in the outside layers and driven into the middle layer where the lower energy states reside. By carefully selecting the lattice mismatch between the different layers, the band gap of the middle layer and its thickness, the energy of the emitted photon can be tuned. To enhance the performance of these light emitting devices, oftentimes multiple quantum wells are stacked together.[119]

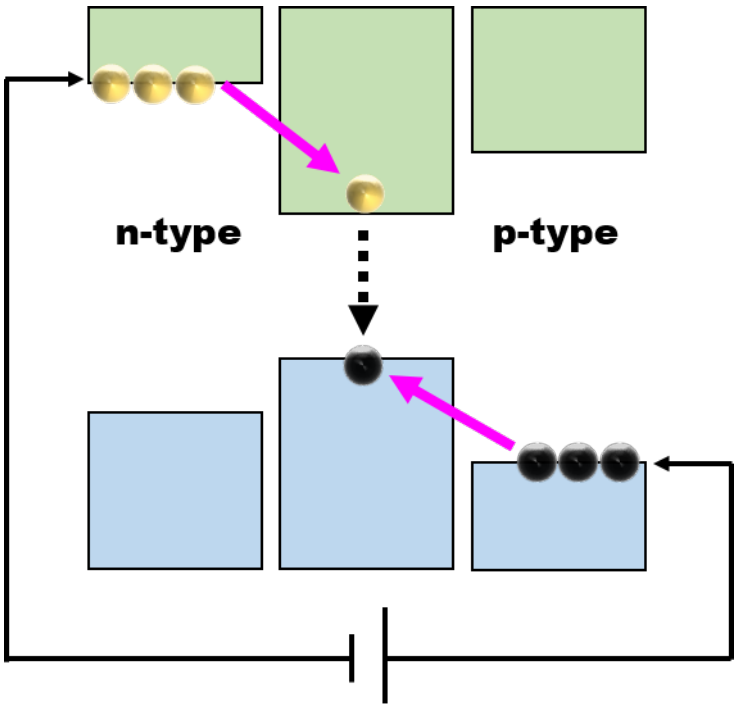

Figure 3.2: Quantum well application formed from Type I heterojunctions.

It has been shown multiple times through theory[62–64] and experiments,[45,55,60,75,120] that type II heterostructures can be formed with semiconducting TMDs MLs, where the conduction band minimum and valence band maximum are located in opposite layers.

The micromechanical exfoliation technique allows for the rapid exploration and realization of multilayer structures and helps reveal functional promising multilayer combinations (see Appendix A). It is in this way that we stumbled upon the MoS_2–$MoSe_2$ bilayer heterostructure. The sample was fabricated by mechanically exfoliating bulk crystals and identifying $MoSe_2$ and MoS_2 MLs by optical contrast on separate transparent substrates. Since ML $MoSe_2$ is affected by ambient conditions, we first transferred the $MoSe_2$ ML onto a Si wafer caped with 90 nm of SiO_2, shown in Figure 3.3(b). Part of the $MoSe_2$ region was then covered with the MoS_2 ML for protection, see Figure 3.3(a) and (c).

Figure 3.3(d) shows the predicted band alignment obtained from first principal calculations,[62–64] where the conduction band lowest electron energy states exclusively populate the MoS_2 layer and the highest valence band states reside in the $MoSe_2$ layer. The conduction (valence) band offset

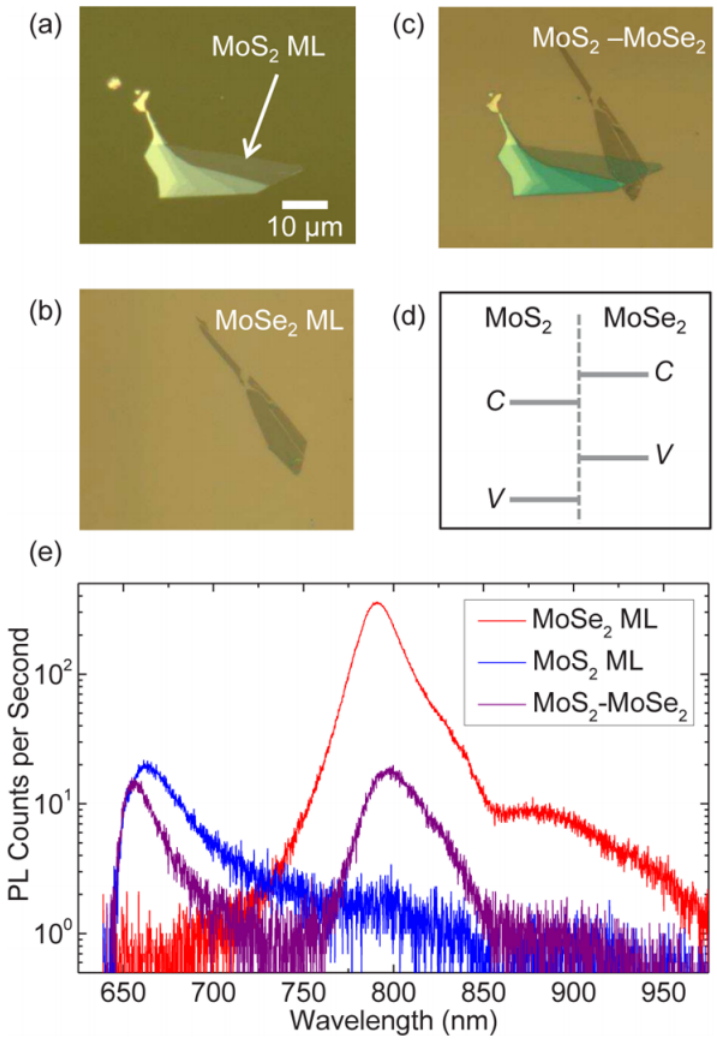

Figure 3.3: (a) Optical image of MoS_2 ML flake on a transparent substrate. (b) The ML $MoSe_2$ on a Si-SiO_2 substrate. (c) The MoS_2–$MoSe_2$ heterostructure sample fabricated by transferring the MoS_2 ML shown in (a) on top of the $MoSe_2$ ML in (b). (d) The type two band alignment of the conduction band and the valence band predicted from first principles.[62–64] (e) PL spectra generated from MoS_2 ML (blue), $MoSe_2$ ML (red), and the heterostructure region (purple). Reproduced with permission.[45] Copyright 2014, American Chemical Society.

is predicted to be about 0.37 (0.63) eV. Fortunately, next to the bilayer heterostructure region, isolated areas of the same composing MLs are also accessible, facilitating and allowing the direct comparison of the heterostructure with the individual MLs.

The PL spectra shown in Figure 3.3(e) of the MoS_2 ML (blue), $MoSe_2$ ML (red), and the MoS_2–$MoSe_2$ heterostructure (purple), was generated under the same experimental conditions with the excitation of a 632.8 nm continuous-wave laser that had an incident power of 50.0 μW. The observed peak positions from the MoS_2 (663.0 nm) and $MoSe_2$ (790.5 nm) MLs are consistent with previously reported values and confirms their thickness.[17,121] Since the PL yield from the $MoSe_2$ ML is about 20 times higher than the PL generated from the MoS_2 ML, we can conclude that stronger nonradiative recombination occurs in MoS_2. The spectrum from the MoS_2–$MoSe_2$ sample consists of two peaks each centered at 656.0 and 798.5 nm, which are close to the individual ML peaks. The 7–8 nm shift of the peaks can be attributed to the different dielectric environment present in the bilayer sample. Moreover, the peak corresponding the $MoSe_2$ layer of the bilayer heterostructure is quenched about 20 times pointing out that most electron excited in $MoSe_2$ prefer to transfer to MoS_2 instead of forming excitons in $MoSe_2$ and radiatively recombining. The same PL quenching effect is also observed in a MoS_2–WSe_2 bilayer heterostructure with a type II band alignment.[120,122] A not so strong quenching (only 30%) can be seen from the PL peak corresponding to the MoS_2 of the heterostructure. This low quenching of the PL can be justified by the stronger nonradiative recombination that occurs in MoS_2. Note that the transition from the conduction band of MoS_2 to the valence band of $MoSe_2$ in the heterostructure is expected to be about 1030 nm, which is out of the spectral range of our detector.[62–64]

To study the charge transfer dynamics as well as the exciton formation and recombination, ultrafast transient absorption measurements were performed in reflection geometry in both the individual MLs and the heterostructure. To study the transfer of electrons from $MoSe_2$ to MoS_2, the pump–probe configuration illustrated in Figure 3.4(a) was used. By tuning the pump pulse to the A exciton resonance of $MoSe_2$ at 790.0 nm [blue arrow in Figure 3.4(a)], we ensure that we selectively inject excitons solely into the $MoSe_2$ layer of the heterostructure since the energy of

the pump photon is far below any exciton states in MoS_2. To monitor the presence of the transferred electrons, the probe pulse is tuned to 655.0 nm, the A exciton resonance in MoS_2, and its differential reflection is measured as a function of probe delay. The differential reflection $\Delta R/R_0$, defined in Section 2.3, its the normalized change in the probe's reflection caused by the pump and when measured as a function of time it displays the lifetime of the photocarrier population. In our case, this would be the lifetime of the electron population occupying the MoS_2 layer of the heterostructure.

Since the pump does not injected photocarriers into the MoS_2 layer, a signal is only expected if the electrons injected in $MoSe_2$ transfer into the conduction band of MoS_2, as illustrated by the purple arrow in Figure 3.4(a). The panels (b) and (c) in Figure 3.4 show the long and short scale dynamics of the signal, respectively, when measured with a pump energy fluence of 5 μJ cm^{-2} (see Appendix B for an explanation of the fluence calculation). As shown in Figure 3.4(c), the signal rapidly reaches its maximum value, within the instrumental response time (see Appendix C) and momentarily maintains the same peak value. The ultrafast rise of the signal shows that the transfer of electrons across the van der Waals interface occurs in an ultrashort time scale, in less than 200 fs, and cannot be resolve by our ultrafast laser system. Surprisingly, this happens despite the strong Coulomb interaction between electrons and holes in the injected excitons. Shortly after, after a few picoseconds, the signal starts to slowly decay as shown with in Figure 3.4(b). The signal is then fitted with a single exponential function (shown as the black curve) from which a 160 ps decay constant is extracted. The decay of the signal reveals that the electrons and holes start to recombine across the interface. To exclude the possibility that probe beam was sensing higher energy states in $MoSe_2$, the measurement was repeated using different probe wavelengths. The results summarized in Figure 3.4(d), demonstrate that magnitude of the signal strongly dependends on the probe wavelength, traces the MoS_2 PL, and peaks roughly at the same position where the MoS_2 PL peaks. With this we confirm that the differential reflection signal is mainly generated in response to electrons that transferred from $MoSe_2$ into MoS_2. To investigate if the signal had any dependence with the injected carrier population, the same measurement were repeated with

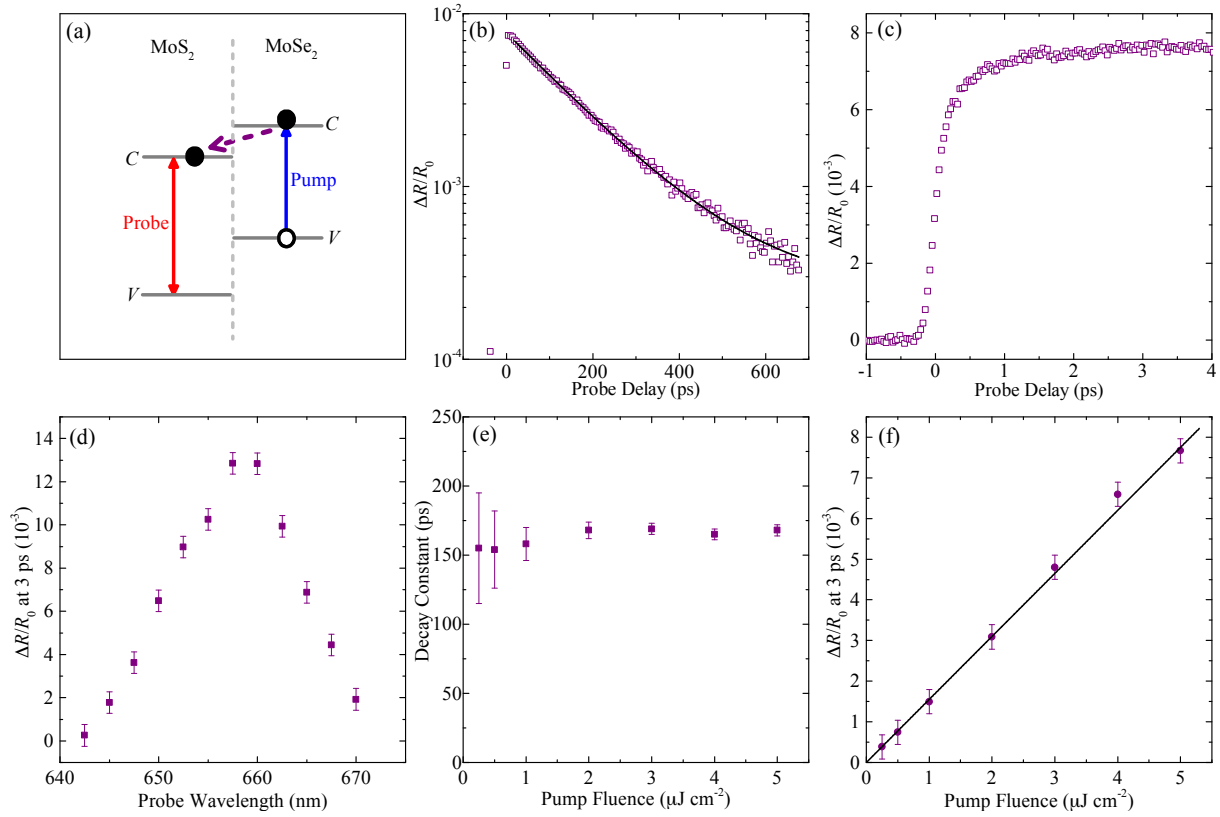

Figure 3.4: (a) Schematic illustration of the pump–probe configuration used to study the transfer of electrons from $MoSe_2$ to MoS_2 in the heterostructure. Differential signal obtained as function of probe delay in a long (b) and short (c) time scale. The solid black curve in (b) is a single exponential fit. (d) Differential reflection signal at 3.0 ps as function of probe wavelength. (e) Decay constant as a function of pump fluence. These were deduce by repeating the measurement at different fluences and fitting the signals with single exponential curves. An example is shown in (b). (f) Differential reflection signal at 3.0 ps as a function of pump fluence. Reproduced with permission.[45] Copyright 2014, American Chemical Society.

different pump fluences and the decay time was extracted. No dependence of the decay time was observed, Figure 3.4(e), and the signal scaled linearly with pump fluence, Figure 3.4(f).

We proceed to investigate the hole transfer from MoS_2 to $MoSe_2$ by using the pump–probe configuration illustrated in Figure 3.5(a). This time, the pump pulse is tuned to the exciton resonance in MoS_2 at 655.0 nm (blue arrow in Figure 3.5(a)) and inevitably both layers are excited. The probe pulse tuned at 790.0 nm (red arrow) senses the presence of holes in the valence band of $MoSe_2$. The differential reflection signal, plotted as a function of probe delay with a pump fluence of 2.0 μJ cm^{-2}, is shown by the purple squares in panels (b) and (c) of Figure 3.5. In the short time scale panel shown in panel (c), the signal rapidly rises and it reaches it peak and then single-exponentially decays with a time constant of about 240 ps extracted from the exponential fit shown by the solid curve in (b).

As we already mentioned, the pump photon energy is large enough to excite both layers; therefore, the differential reflection signal originates from holes directly injected in $MoSe_2$ and holes that transfer from MoS_2. To separate the contribution from the transferred holes that were directly injected in MoS_2, we repeated the measurement with different pump wavelengths around the MoS_2 exciton resonance. The purple squares in Figure 3.5(d) show the magnitude of the signal at 3.0 ps for different pump wavelengths. In the same figure, the MoS_2 PL is shown as the gray curve. The wavelength dependance of the signal exhibits the contribution the holes that transfer from MoS_2 into $MoSe_2$ make to the differential reflection signal. The 30% variation in the signal observed, indicate the contribution holes that transfer from MoS_2 make to the signal. Moreover, as is expected, the dynamics of the signal show no dependence as the pump wavelength was varied. The orange squares in Figure 3.5(c) show the signal obtained after a 670.0 nm pump excited both layers while the same 790.0 nm probe monitored the presence of holes in $MoSe_2$. By scaling this signal by a factor of 1.25, gray squares in panel (c), the scaled signal perfectly matches the signal detected when a 655.0 nm pump excited both layers. From the ultrafast rise of the signal shown in panel (c) by the purple or orange squares, we can conclude that the hole transfer occurs within a subpicosecond time scale, faster than the time resolution of our system. If this was not the case, a

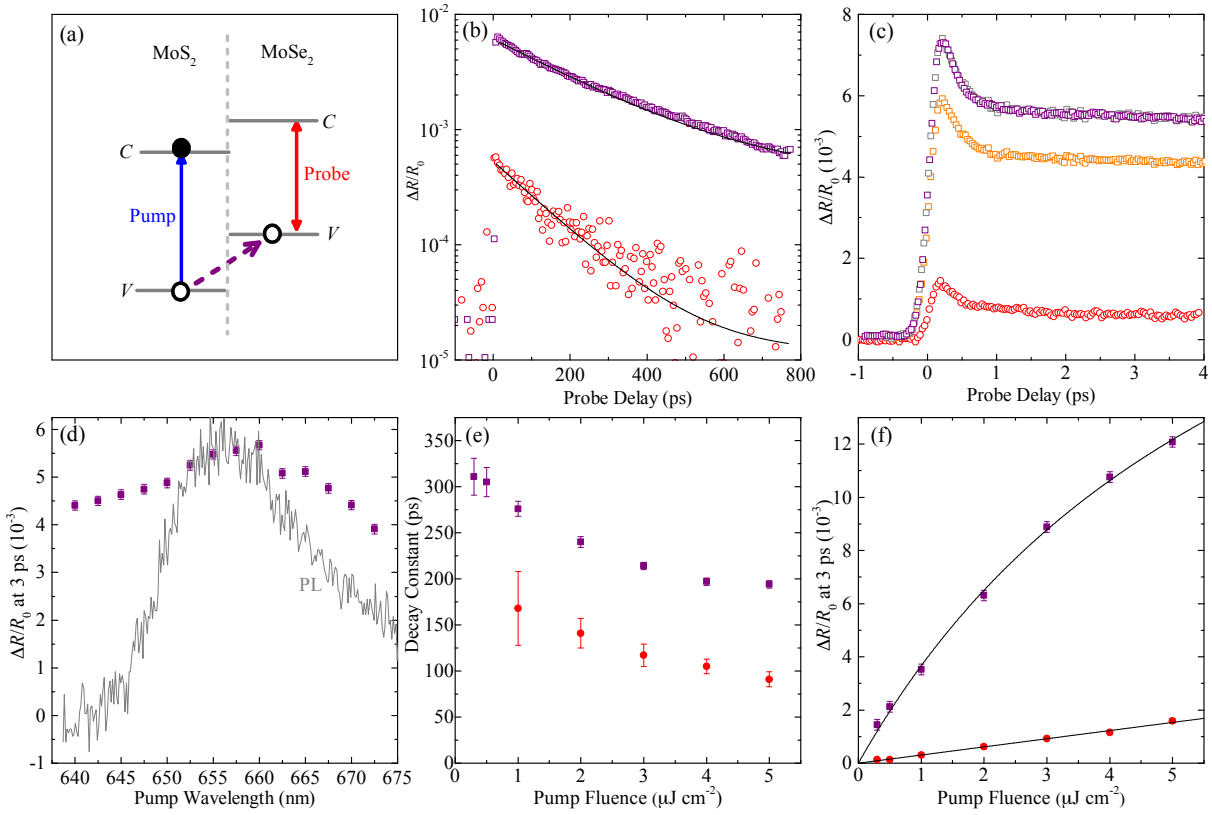

Figure 3.5: (a) Schematic illustration of the pump–probe configuration used to study the transfer of holes from MoS_2 to $MoSe_2$ in the heterostructure. The differential signal obtained as function of probe delay in a long (b) and short (c) time scale. The purple squares in (b) and (c) show the differential signal obtained from the heterostructure using a 655.0 nm pump and a 790.0 nm probe. The differential reflection signal from a $MoSe_2$ ML is shown as the red circles in (b) and (c). The orange circles in (c) show the differential reflection signal from the heterostructure when a 670.0 nm pump excites both layers while 790.0 nm probe senses the $MoSe_2$. The gray squares in (c) represent the scaled signal obtained from the orange squares. (d) Differential reflection signal at 3.0 ps as function of pump wavelength (purple squares). The gray curve is the PL generated from a MoS_2 ML. (e) Decay constants from the heterostructure (purple squares) and from the $MoSe_2$ ML (red circles) plotted as function of pump fluence. (f) Differential reflection at 3.0 ps for the heterostructure (purple squares) and the $MoSe_2$ ML (red circles) plotted as function of pump fluence. Reproduced with permission.[45] Copyright 2014, American Chemical Society.

slow rise of the signal at early times would be expected. However, we do not observe this.

After the electrons and holes have separated, due to the type II band alignment in this system, it is expected that they will form charge transfer excitons, where electrons and holes populate different layers. Since the spatial overlap between the electron and hole wave functions is decreased, due to their increase in spatial separation, it's expected that the electron-hole recombination would be suppressed. To establish this, we measured the exciton lifetimes in the isolated MoS_2 and $MoSe_2$ regions shown in Figure 3.3(c). For comparison, the signal obtained from the $MoSe_2$ ML, taken under the same experimental conditions as the signal shown by the purple squares in panel (b), is shown as the red circles Figure 3.5(b) and (c). The signal from $MoSe_2$ is roughly 10 times less and can be fitted with a single exponential function (solid curve) that is characterized with a time constant of 150 ps. The MoS_2 signal (not shown here) decays even faster. Therefore, we can conclude that the signal obtained from the bilayer heterostructure that decays with a time constant of 240 ps reflects that extended recombination lifetime of the charge transfer excitons. Panels (e) and (f) in Figure 3.5, show the decay constant dependence as well as the dependence of the signal with pump fluence for holes in the heterostructure (purple squares) and excitons in ML $MoSe_2$ (red circles).

With evidence presented for the MoS_2–$MoSe_2$ heterostructure, we establish that ultrafast charge separation and the formation of charge transfer excitons that exhibit extended lifetimes occurs in type II heterostructures formed by two semiconducting MLs. Moreover, the strong PL quenching observed in the heterostructure regions indicates that the charge transfer is highly efficient. Our results are consistent with other experiments. For example, in their measurements Hong *et al* observed in a MoS_2–WS_2 heterostructure, which has a type II band alignment, ultrafast charge separation, quenched PL from the heterostructure region, and derived $\sim$50 fs hole transfer times.[60] Moreover, Fang *et al* showed that in a WSe_2–MoS_2 heterostructure a new strong PL emerged at a lower energy that couldn't be attributed to either WSe_2 or MoS_2 PL.[120] Therefore, since the PL generated by the individual MLs was heavily quenched, it was presented as evidence of the strong and efficient charge transfer exciton radiative recombination.

3.2 Spatiotemporal Dynamics of Charge Transfer Excitons in a $MoSe_2$–WS_2 Bilayer Heterostructure

In this section we show that the van der Waals heterostructure formed by $MoSe_2$ and WS_2 provides a unique system with near degenerate interlayer and intralayer excitonic states. Our photoluminescence measurements indicate that the charge transfer exciton states are approximately 50 meV below the $MoSe_2$ exciton states, with a significant spectral overlap. By monitoring the transient absorption of a femtosecond pulse, we studied the spatial and temporal dynamics of the charge transfer excitons at room temperature. We found a lifetime of approximately 80 ps for the charge transfer excitons and a diffusion coefficient of about 14 $cm^2\ s^{-1}$ was deduced, which is comparable to individual excitons in transition metal dichalcogenides. The results in this section were published in Nanoscale.[123]

3.2.1 Excitonic States in $MoSe_2$–WS_2 heterostructure

The $MoSe_2$–WS_2 heterostructure sample studied is shown schematically in Figure 3.6(a) and visually in Figure 3.6(b). The monolayers composing the heterostructure have neighboring secluded regions of WS_2 and $MoSe_2$ which ease the comparison between any measurement done in the heterostructure and its constituent monolayers. No efforts were made to determine and control the relative orientations of the two flakes; as a matter of fact, the WS_2 location was selected so that the heterostructure region contained a large area. In all the measurements discussed here, the sample was kept under an ambient condition. No sample degradation was observed during the course of the entire study.

Two groups have predicted, using first-principle calculations[63,64] that the conduction band offset of $MoSe_2$ and WS_2 could be as small as 20 or 60 meV. Figure 3.6(c) shows schematically the type-II band alignment of this heterostructure, where the near degenerate conduction bands facilitate the control of the electron population between the two layers which can be utilized in tunneling-based devices.

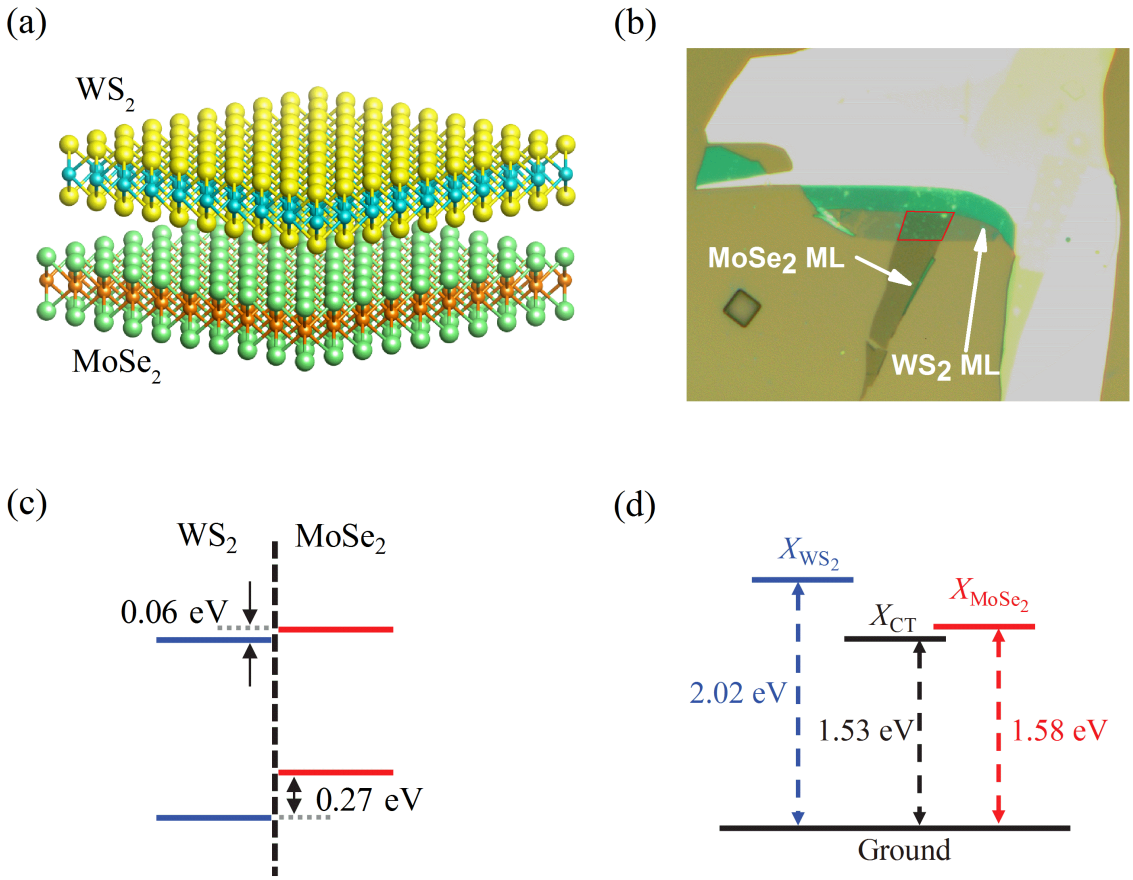

Figure 3.6: (a) Schematic illustration of the $MoSe_2$–WS_2 heterostructure. (b) Microscope images of the sample containing the heterostructure (indicated by the red box) and the individual $MoSe_2$ and WS_2 monolayer regions on the a Si–SiO_2 substrate. Band alignment predicted by first principle calculations,[63] showing 60 and 270 meV conduction and valence band offsets, respectively. (d) Energy diagram of excitons states determined by the photoluminescence spectrum. Reproduced by permission from The Royal Society of Chemistry.[123]

We begin our study by conducting PL spectroscopy on the heterostructure and its neighboring monolayers. To generate the PL a continuous wave laser with a 405 nm wavelength and incident power of 0.6 μW was focused onto a perpendicularly placed sample using a 50$\times$ microscope objective lens. The PL spectra of the WS_2 (blue), $MoSe_2$ (red), and WS_2–$MoSe_2$ heterostructure (black), shown in Figure 3.7, were collected by an imaging spectrometer equipped with a thermoelectrically cooled CCD camera. An intense PL emission centered at 617.3 nm was observed when the laser spot was located on the WS_2 monolayer region (blue curve in Figure 3.7, divided by 23). The peak position, line-width, and PL yield are all reasonably consistent with previous reports,[124–127] further confirming its monolayer thickness. When the laser spot was placed on the $MoSe_2$ region, a much weaker PL peak was observed at 785.5 nm (red curve in Figure 3.7), which is also consistent with previous results.[27,96,128]

Of more interest is the heterostructure PL spectrum which exhibits two peaks at 614.7 nm and 810.0 nm. Without interlayer coupling or charge transfer, the PL spectrum of the heterostructure is expected to be the sum of the two individual monolayer spectrum. However, the 614.7 nm peak, due to the radiative recombination of excitons in the WS_2 layer of the heterostructure, is close to the WS_2 monolayer peak, but is slightly blue shifted due to the different dielectric environment present in the heterostructure. Moreover, its magnitude has been quenched by a factor of 23, suggesting that most of the holes created in WS_2 transferred to $MoSe_2$ before forming direct excitons and recombining radiatively. A similar PL quenching effect has been recently observed on WS_2–MoS_2 heterostructures with clean interfaces.[60,67,129–131] In addition, its shape displays a shoulder, absent in the WS_2 PL spectrum, that occurs at longer wavelengths from the 614.7 nm peak and is attributed to the formation of trions.[132]

The strong peak at 810.0 nm, observed in the heterostructure, appears near the spectral range of the $MoSe_2$ exciton. The following facts show that the radiative recombination of excitons in $MoSe_2$ is not the origin of this peak. First, the 810.0 nm peak in the heterostructure is 25.0 nm longer than the $MoSe_2$ monolayer PL peak (785.5 nm). When forming heterostructures, the exciton binding energies are expected to slightly change due to the different dielectric environment; actually, pre-

vious measurements show that the shift of the $MoSe_2$ PL peak is at most a few nanometers when forming heterostructures with MoS_2[45] and WSe_2.[55] Considering the similar dielectric properties of these TMDs, it is unlikely that WS_2 would cause a 25 nm shift of the $MoSe_2$ exciton peak. In fact, in this sample, the shift of the WS_2 peak is only 2.6 nm. Second, previous studies on TMD heterostructures have all observed PL quenching. Specifically, exciton PL of $MoSe_2$ was found to be reduced by a factor of 15 when forming a heterostructure with MoS_2[45] and by a factor of 5 with WSe_2.[55] However, the 810 nm peak magnitude in our $MoSe_2$–WS_2 heterostructure sample is twice as large than the magnitude of the $MoSe_2$ monolayer, strongly suggesting that it does not originate from excitons in $MoSe_2$.

Having excluded the $MoSe_2$ excitons as the origin, we attribute the 810 nm peak to the spatially indirect excitons, known as charge transfer excitons (X_{CT}). Upon optical excitation with a 405.0 nm laser, electrons and holes are injected into both layers. This would normally produce direct excitons that would reside and decay in the particular layer they were produced; however, as a result of the heterostructure type-II band alignment, where the minimum of the conduction band is located in the WS_2 monolayer and the maximum of the valence band is in the $MoSe_2$ monolayer, spatial separation of most electrons and holes after the photoexcitation will ensue. Despite the fact that electrons populate the WS_2 monolayer and holes the $MoSe_2$ monolayer, their electrostatic Coulomb force binds them together to form charge transfer excitons. With this assignment, we can construct the exciton energy states diagram as shown in Figure 3.6(d). The energy difference of 50 meV between the charge transfer and $MoSe_2$ excitons is order-of-magnitude consistent with the theoretical predictions on the conduction band offset.[63,64]

We note that the annealing process described in Appendix A is necessary for forming a clean interface between the two monolayers, which is required for efficient charge transfer. Samples before the annealing process show no sign of charge transfer, where the PL spectra of the heterostructure is similar to the sum of the spectra of individual monolayers.

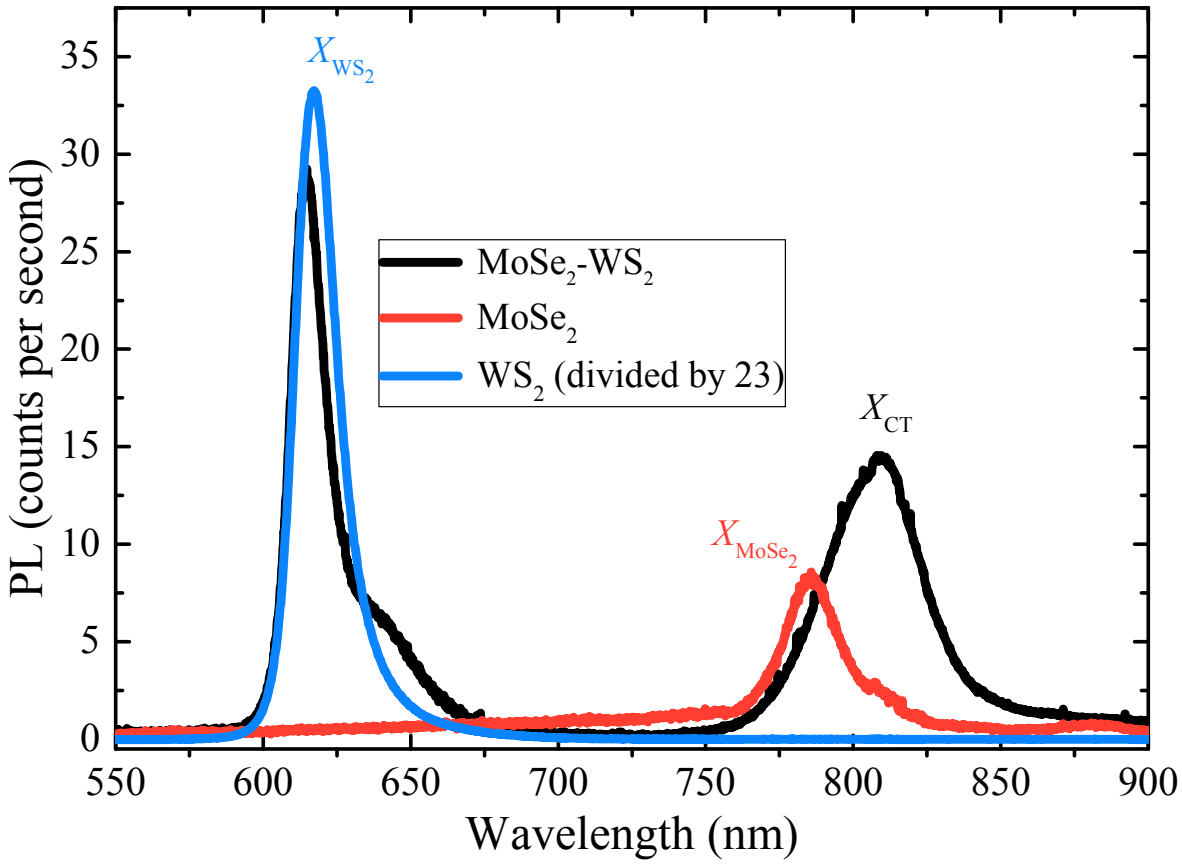

Figure 3.7: Room Temperature photoluminescence spectra of the $MoSe_2$–WS_2 heterostructure (black) and the individual WS_2 (blue, divided by 23) and $MoSe_2$ (red) monolayers obtained under the same experimental conditions. The pink curves are the two components of a double-Gaussian fit to the 810 nm peak. Reproduced by permission from The Royal Society of Chemistry.[123]

3.2.2 Probing The Charge Transfer Excitons

To further confirm the observation of the charge transfer excitons, we performed transient absorption measurements in reflection geometry. A 730 nm pump pulse with a peak fluence of 5.6 μJ cm^{-2} is used to inject excitons in the $MoSe_2$ layer of the heterostructure sample. To monitor the charge transfer excitons, we measured the differential reflection of a 810 nm probe pulse (tuned to the charge transfer exciton PL peak). The differential reflection is defined as the relative change of the probe reflection cause by the presence of the pump, see Section 2.3. We observed a strong differential reflection signal with a magnitude on the order of 10^{-3}, as shown by the black curves in Figure 3.8, that reaches a peak immediately following the pump excitation. The ultrafast rise of the signal is a clear indication that charge transfer excitons are formed in an ultrashort time scale.

Two control experiments were performed to ensure that the charge transfer excitons were probed. First, we repeated the measurement on the $MoSe_2$ monolayer region of the flake, where no signal could be measured (shown as the blue curves on Figure 3.8) since the 810 nm pulse is well below the exciton resonance of $MoSe_2$. Second, we used the 810 nm pulse as the pump and 730 nm pulse as the probe on the heterostructure sample. No signal was observed (shown as the purple curve on Figure 3.8), which further confirms the nature of the 810 nm peak. As a spatially indirect transition, its absorption is expected to be weak and even if some charge transfer excitons are injected by the 810 nm pump, they cannot populate the $MoSe_2$ exciton states; therefore, they should not be detected by the 730 nm probe. These two measurements prove unambiguously that the black curves shown in Figure 3.8 are indeed from the charge transfer excitons.

To compare the charge transfer excitons with excitons in the individual monolayers, we probed the excitons in $MoSe_2$ (395 nm pump and 790 nm probe, red curve) and WS_2 (385 nm pump and 620 nm probe, orange curve) regions. We found that under the same conditions, the differential reflection signals when probing the monolayers were larger than the signal of the charge transfer excitons. Although part of the difference could be attributed to changes of absorption coefficient at different pump wavelengths, the indirect nature of the charge transfer exciton absorption should result in a weaker transient absorption response.

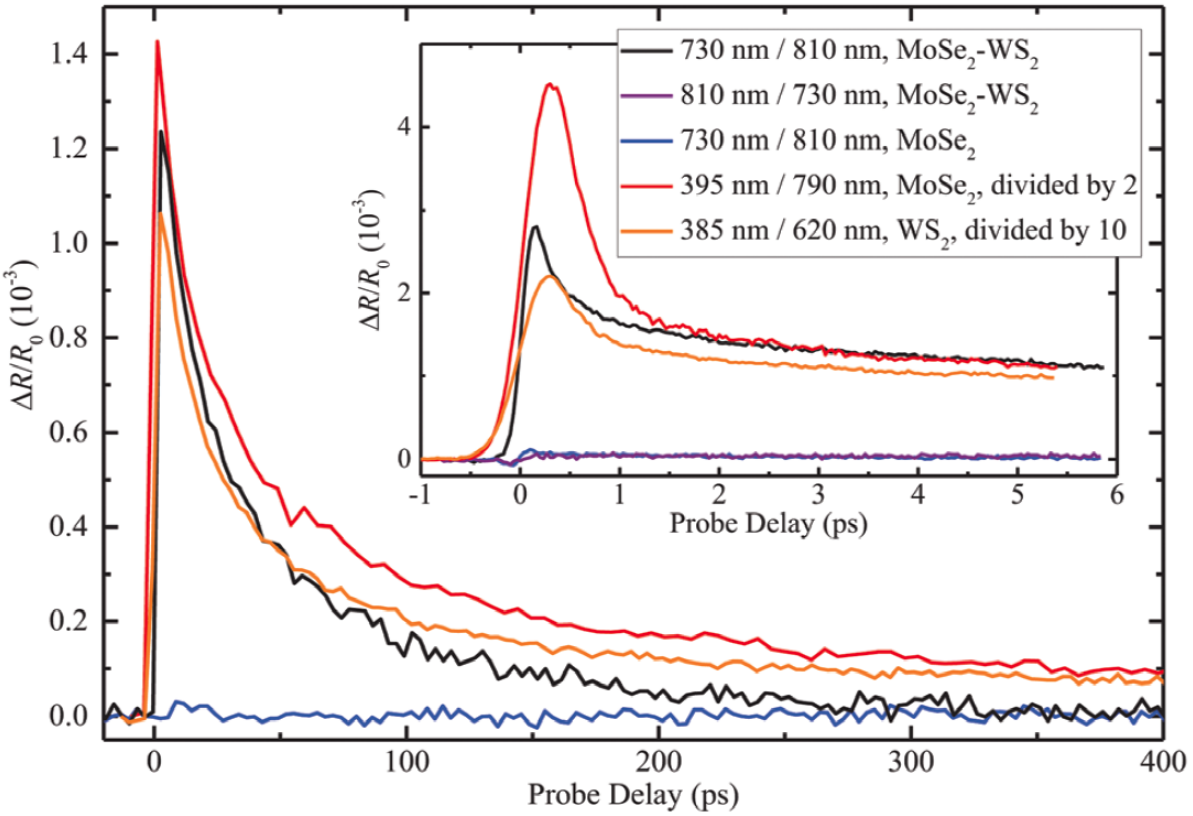

Figure 3.8: Differential reflection signals measured with 730 nm pump and 810 nm probe pulses from the $MoSe_2$–WS_2 heterostructure (black) and individual $MoSe_2$ (blue) at room temperature. The red and orange curves are signals from individual $MoSe_2$ and WS_2 monolayers, with 395 nm / 790 nm and 385 nm / 620 nm pump/probe wavelengths, respectively. The purple curve shows the signal from the heterostructure sample with 810 nm / 730 nm configuration. The inset shows the results near zero probe delay. Reproduced by permission from The Royal Society of Chemistry.[123]

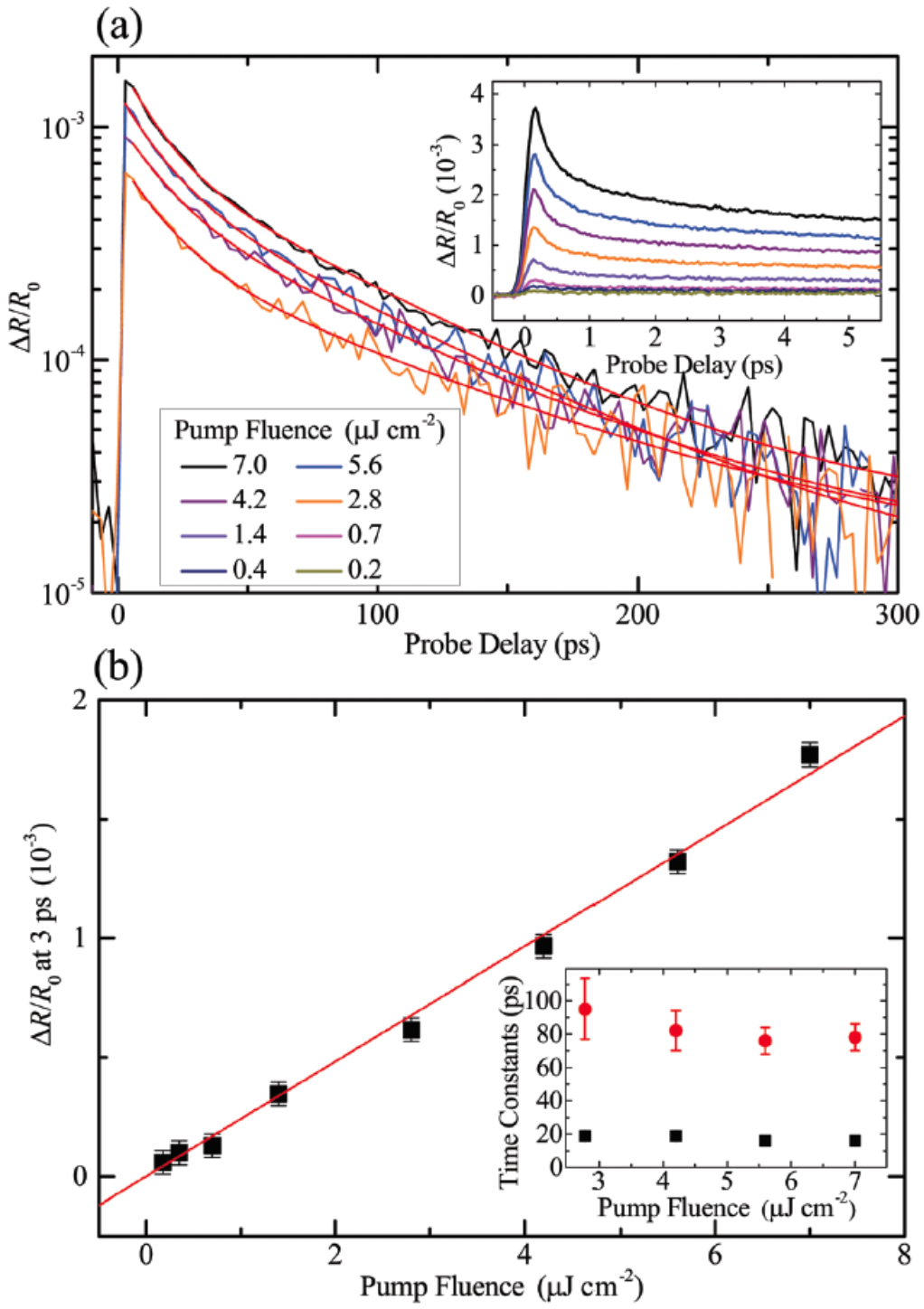

Figure 3.9: (a) Differential reflection signals measured at room temperature with 730 nm pump and 810 nm probe pulses from the $MoSe_2$–WS_2 heterostructure with different values of the pump pulse fluence as indicated. The red curves are bi-exponential fits. (b) The magnitude of the differential reflection signal, represented by the signal at a probe delay of 3 ps, as a function of the pump fluence. The inset shows the short (black squares) and long (red circles) time constants obtained from the fits shown in (a). Reproduced by permission from The Royal Society of Chemistry.[123]

3.2.3 Dynamics of Charge Transfer Excitons

Having established the probe of charge transfer excitons, we used the 730 nm pump and 810 nm probe to study the dynamics of charge transfer excitons.

First, to study the recombination of charge transfer excitons, we performed time-resolved differential reflection measurements with different values of the pump fluence. Figure 3.9(a) shows the decay of the signal, with the pump fluences indicated in the figure. We find that the magnitude of the signal is proportional to the pump fluence, as summarized in Figure 3.9(b), which shows that the transient absorption signal is proportional to the density of the charge transfer excitons. After a short transient of less than 1 ps, the rest of the decay can be well described by bi-exponential functions, as confirmed by the fits shown as the red curves in Figure 3.9(a). The two time constants obtained from these fits are summarized in the inset of Figure 3.9(b). We found that in this range, the decay constants are independent of the pump fluence, which shows the multiexciton recombination process plays an unimportant role in the dynamics of charge transfer excitons. This is in contrast to exciton dynamics in monolayer $MoSe_2$, where a density dependent dynamic due to exciton–exciton annihilation was observed.[96] We attribute the long time constant of approximately 80 ps to the lifetime of charge transfer excitons. Given the expected long radiative lifetime of these excitons, the lifetime deduced here is likely limited by nonradiative recombination. The short time constant of less than 20 ps can be attributed to energy relaxation since the carriers are injected with large excess energies.

Next, we performed spatially resolved differential reflection measurements to study the diffusion of charge transfer excitons, see Section 2.5 for more details. Here, the pump and probe pulses are both focused to about 2 μm in full width at half maximum. The distance between the centers of the pump and probe spots, defined as the probe position (with respect to the pump spot center), can be adjusted by slightly changing the incident angle of the beam to the objective lens. By measuring the differential reflection signal as a function of the probe delay at each probe position, we obtain the evolution of the signal as a function of both time and space, as plotted in Figure 3.10(a). At each probe delay, the spatial profile has a Gaussian shape. Figure 3.10(b) shows a few examples

of these profiles, along with the Gaussian fits (solid curves). The squared width deduced from all the fits are plotted in Figure 3.10(c), as a function of the probe delay.

In this process, the pump pulse injects excitons in $MoSe_2$, which form charge transfer excitons rapidly after the electrons moved to WS_2 that then diffuse in the heterostructure, driven by the in-plane density gradient. This diffusion process can be described by the classic diffusion equation, which predicts that the squared width (full of the profile increases linearly as $w^2(t) = w_0^2 + 16\ln(2)Dt$, where D and w_0 are the exciton diffusion coefficient and the initial width, respectively.[107] We find that this model can well describe the expansion of the profile after about 20 ps. By a linear fit, as indicated by the red line in Figure 3.10(c), we obtain a diffusion coefficient of 14 ± 3 cm^2 s^{-1}. This value is similar to exciton diffusion coefficients found in individual TMD monolayers,[110,112] showing that the spatial indirect nature of the charge transfer excitons does not significantly change its in-plane transport property.

3.2.4 Conclusion on $MoSe_2$–WS_2 Bilayer Heterostructure

We present multiple evidence that the 810 nm PL peak originates from charge transfer excitons in the $MoSe_2$–WS_2 heterostructures. Based on that, we constructed the energy diagram of exciton states in this structure, with near degenerate charge transfer and $MoSe_2$ exciton states. Our PL measurement confirmed the theoretical predictions of the small conduction band offset of this structure. Finally, through transient absorption measurements with high temporal and spatial resolution, we obtained a lifetime of 80 ps and an in-plane diffusion coefficient of 14 cm^2 s^{-1} for these charge transfer excitons.

3.3 Highly Efficient and Ultrafast Charge Transfer in a MoS_2–WS_2–$MoSe_2$ Three-layer Heterostructure

A central issue in developing such multilayer structures is understanding and controlling the interlayer electron transfer process, which plays a key role in implementing these materials in logic

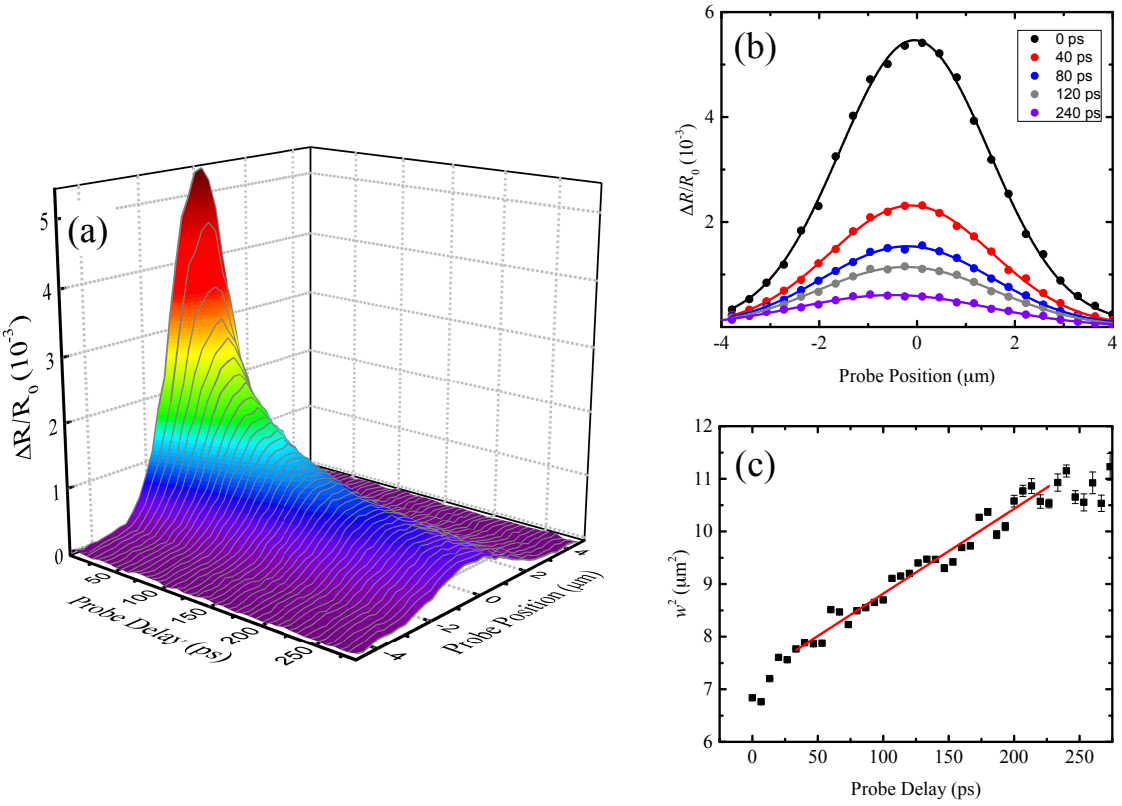

Figure 3.10: (a) Differential reflection signal of the $MoSe_2$–WS_2 heterostructure as a function of the probe delay and probe position at room temperature. The pump and probe wavelengths are 730 and 810 nm, respectively. (b) Examples of the spatial profiles of differential reflection at several probe delays. The solid curves are Gaussian fits. (c) Squared width of the profile deduced from Gaussian fits as a function of the probe delay. The linear fit, as indicated by the red line, corresponds to an exciton diffusion coefficient of 14 cm^2 s^{-1}. Reproduced by permission from The Royal Society of Chemistry.[123]

electronics, thin-film transistors, and optoelectronics. Recent efforts on this issue have focused on bilayer heterostructures. Our steady state optical measurements and that of others have revealed effective charge transfer between different monolayers from the quenching of photoluminescence.[55,75,120,122,130,132,133] Later, transient absorption measurements were attempted to time resolve the charge transfer between two different monolayers. It was found that this process occurs on an ultrafast time scale that was beyond the time resolution of these studies, has it been demonstrated in the previous two sections.[45,60,123,134] Due to the weak interlayer coupling and the large momentum mismatch between these atomic layers, such a fast transfer is rather surprising.[135] Various mechanisms have been proposed, such as resonant transfer to higher energy states,[135] delocalization of the electron wave function in momentum space,[135] coherence enhancement,[136] and Coulomb potential enhancement.[137] Nevertheless, there is still a lack of fundamental understanding on how this process can be so efficient at van der Waals interfaces.

In this section, we show evidence suggesting the coherent nature of the interlayer electron transfer. In a three-layer sample of MoS_2–WS_2–$MoSe_2$, electrons excited in $MoSe_2$ transfer to MoS_2 in about one picosecond. Surprisingly, these electrons do not populate the middle WS_2 layer during this process. Calculations showed the coherent nature of the charge transfer and reproduced the measured electron transfer time. The hole transfer from MoS_2 to $MoSe_2$ is also found to be efficient and ultrafast. The separation of electrons and holes extends their lifetimes to more than one nanosecond, suggesting potential applications of such multilayer structures in optoelectronics. Most results in this section were published in Nano Letters.[138]

3.3.1 Experimental Section

The three-layer sample, which is schematically shown in Figure 3.11(a), was fabricated by mechanically exfoliating the monolayers and transferring them one by one, with the sequence of $MoSe_2$–WS_2–MoS_2, on a silicon substrate covered with 90 nm of SiO_2, (see Appendix A for more details). The monolayer thickness of each layer was identified by optical contrast and photoluminescence. The sample was kept in an ambient condition during all the measurements.

The interlayer charge transfer and the charge transfer exciton lifetime in the three-layer sample was studied by PL and the ultrafast pump–probe technique based on a 80 MHz femtosecond laser system, see Section 2.1 and 2.3.

3.3.2 Coherent Electron Transport Across a Monolayer

According to first-principle calculations,[62,63] this three-layer sample forms a ladder alignment in both the conduction and the valence bands, as schematically shown in Figure 3.11(b).The conduction band minimum and valence band maximum lie in the MoS_2 and $MoSe_2$ layers, respectively. Photoluminescence measurements were performed to probe the quality of the interfaces, as shown in Figure 3.11(c). Without the interlayer charge transfer, the spectrum of the three-layer sample would resemble the sum of the spectra from the three monolayers. However, the WS_2 A- exciton peak is about 250 times weaker in the three-layer sample than the monolayer. The significant quenching of the MoS_2 and $MoSe_2$ peaks, which are practically invisible in the three-layer spectrum, also confirms the high quality of the interfaces between the monolayers.[55,75,120,122,130,132,133] The strong peak at 1.54 eV observed in the three-layer is consistent with the charge transfer exciton PL we previously identified in the $MoSe_2$–WS_2 heterostructure.[123,132]

The interlayer charge transfer in the three-layer sample was studied by the ultrafast pump–probe technique based on a 80 MHz femtosecond laser system.[78] A 1.57 eV and 100-fs pump pulse is used to selectively excite electrons in $MoSe_2$. Since the optical band gaps of MoS_2 and WS_2 are 1.88 and 2.01 eV, respectively, the pump photon energy is not sufficient to excite these layers. Once excited to the conduction band of $MoSe_2$, the electrons are expected to transfer to MoS_2, as shown in Figure 3.11(b). To monitor the population of these electrons in the conduction band of MoS_2, the differential reflection of a 1.88 eV probe pulse (tuned to the MoS_2 optical band gap) was measured as a function of its arrival time at the sample with respect to the pump pulse. The carrier densities initially injected in $MoSe_2$, as indicated in the label of Figure 3.11(d), were estimated from the fluences of the pump pulse and the absorption coefficient of $MoSe_2$, see Appendix B for more details. A control experiment performed with a $MoSe_2$ monolayer yielded no signal,

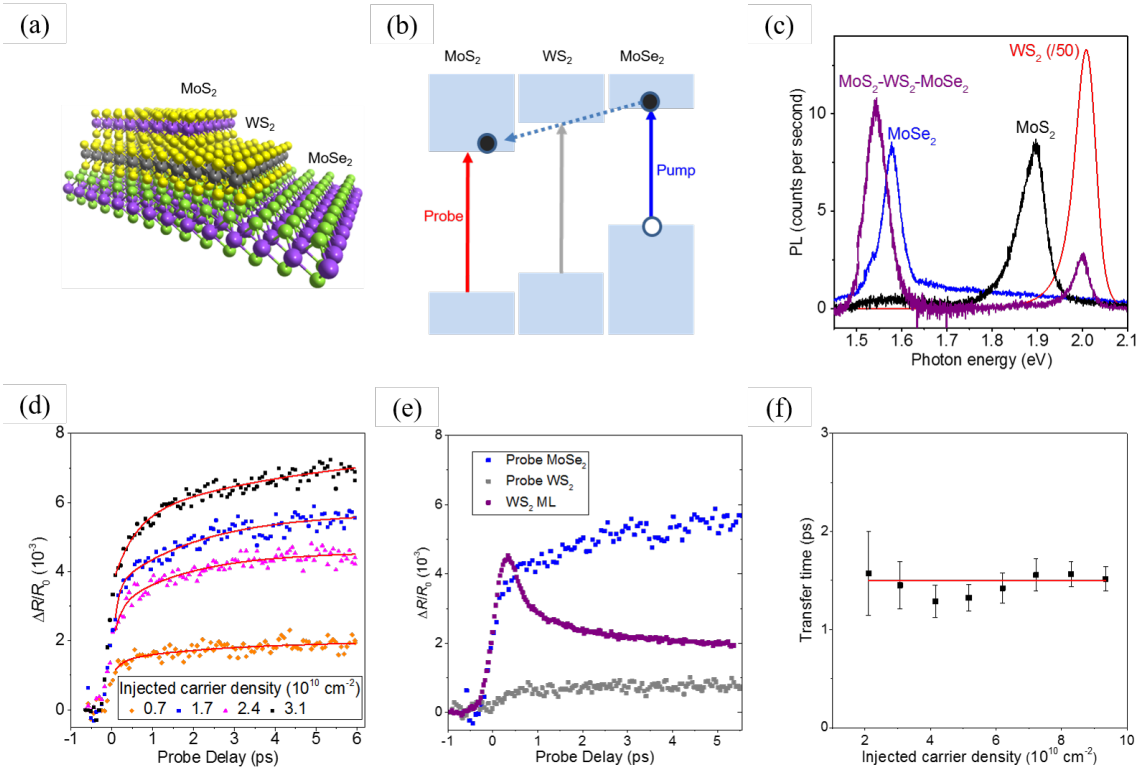

Figure 3.11: (a) Schematic illustration of the MoS_2–WS_2–$MoSe_2$ trilayer sample studied. (b) Band alignment of the three-layer sample and the pump–probe configuration, where a pump pulse excited the $MoSe_2$ layer and a probe pulse detects carriers in MoS_2. (c) Photoluminescence spectra of the three-layer (purple) and monolayers of MoS_2 (black), WS_2 (red, divided by 50), and $MoSe_2$ (blue) under steady excitation of 405 nm and 0.5 μW. (d) Differential reflection of a 1.88 eV probe pulse (sensing carriers in MoS_2) after a pump pulse of 1.57 eV injected carriers in $MoSe_2$. The red curves are fits. (e) The gray symbols are differential reflection of a 2.00 eV probe (sensing WS_2 of the three-layer) after a pump pulse of 1.57 eV injected carriers in $MoSe_2$. The purple symbols are measured from a WS_2 monolayer sample with a 3.14 eV pump pulse injecting carriers. The blue symbols are replotted from (d) for comparison. (f) Charge transfer time as a function of injected carrier density. Reprinted with permission.[138] Copyright 2017, American Chemical Society

confirming that the 1.88 eV probe does not sense carriers in $MoSe_2$. Hence, the signal originates from electrons in MoS_2 that have transferred from $MoSe_2$. The rise of the signal can be modeled, as indicated by the red curves in Figure 3.11(d), by noticing that the population of electrons in MoS_2 should follow $N(t) = N_0[1 - \exp(-t/\tau_e)]$, where N_0 is the initially injected density in $MoSe_2$ and τ_e the transfer time. Here we assume that all the electrons injected in $MoSe_2$ transfer to MoS_2 due to the strong photoluminescence quenching observed in the three-layer sample, where the $MoSe_2$ photoluminescence is practically absent in the three-layer spectrum, as shown in Figure 3.11(c). From these fits and others that are not shown, we obtain an average charge transfer time of 1.5 $\pm$ 0.2 ps, which shows no significant density dependence, see Figure 3.11(f).

To determine whether the electrons temporarily populate the conduction band of the WS_2 middle layer during the transfer, a 2.00 eV probe was used, which is tuned to the optical band gap of WS_2. To gauge the probe, we first measured a WS_2 monolayer sample. With a pump of 3.18 eV injecting a carrier density of about 4.3×10^{10} cm^{-2}, a signal of about 4×10^{-3} was observed, purple symbols in Figure 3.11(e). If the electron transfer from $MoSe_2$ to MoS_2 is an incoherent and sequential process, the electrons are expected to temporarily populate WS_2. With the 1.57 eV pump injecting a density of 4.3×10^{10} cm^{-2} in $MoSe_2$, one would expect the detection of a transient signal that would last for about 1 ps and with a peak magnitude similar to the purple symbols. However, the observed signal (gray symbols) is much weaker than expected and does not show the temporal feature described above. A detailed investigation on the magnitude and temporal behavior of this residual signal shows that it originates from the holes residing in $MoSe_2$.

3.3.3 Simulation of the Electron Transfer

The observation that the electrons do not populate WS_2 as they move from $MoSe_2$ to MoS_2 suggests that the transfer could be a coherent process. To obtain physics insight into this process, our collaborators performed nonadiabatic molecular dynamics simulations to make the discussion more complete.[139,140] An electron transfer time of about 0.9 ps was obtained, in good agreement with the experiment.

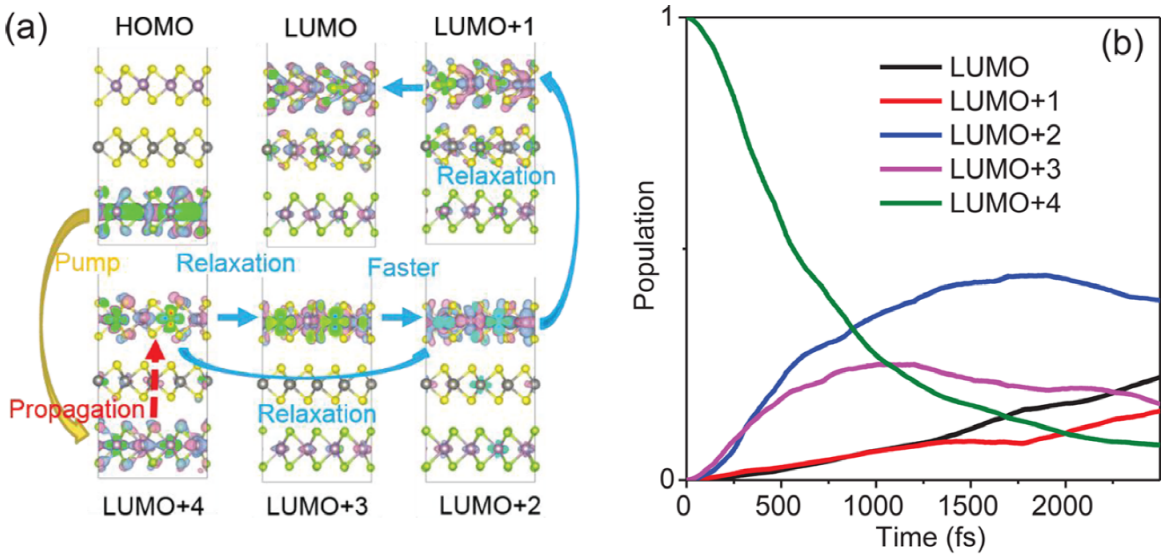

Figure 3.12: (a) Schematic diagram of energy levels involved in the excited electron dynamics. (b) Decay of population of excited electron states. Adapted with permission.[138] Copyright 2017, American Chemical Society

Figure 3.12(a) shows wave functions of the states near the band edges, based on the configuration of the molecular dynamic trajectory at 1 ps. The highest occupied molecular orbital (HOMO) is entirely localized in $MoSe_2$, while the lowest unoccupied molecular orbital (LUMO) is mostly localized in MoS_2 but slightly extends to the other two layers. Among higher excited states, the LUMO+1, LUMO+2, and LUMO+3 states exhibit similar wave function distributions as LUMO, whereas only LUMO+4 shows significant distribution in the $MoSe_2$. Hence, the 1.57 eV pump excites electrons initially from HOMO to LUMO+4, where the electrons are delocalized between $MoSe_2$ and MoS_2. The initially excited LUMO+4 can be viewed as a donor state while the four lower LUMO states can be viewed as acceptor states. The strong donor–acceptor interaction results in the electron transfer from $MoSe_2$ to MoS_2. More importantly, in both acceptor and donor states, molecular orbitals are mostly localized in $MoSe_2$ and MoS_2, indicating that electrons can coherently transfer from $MoSe_2$ to MoS_2 without populating WS_2.

Figure 3.12(b) shows the simulated dynamics of the electron population at various LUMO levels. From an exponential fit to the LUMO+4 population shown in green in Figure 3.12(b), an electron transfer time of about 0.9 ps was obtained, in good agreement with the experiment.

3.3.4 Hole Transfer Across a Semiconducting Monolayer

The ladder arrangement of the valence bands in the sample allows hole transfer from MoS_2 to $MoSe_2$, opposite to the electron transfer direction as shown in Figure 3.13(a). To study this process, a 1.88 eV pump excites MoS_2 while a 1.57 eV probe monitors $MoSe_2$. The result is shown by the blue symbols in Figure 3.13(b). Although undesired for the sake of investigating hole transfer, the pump also inevitably injects carriers in $MoSe_2$, which has a smaller optical band gap. The total carrier density injected in the two layers is about 1.3×10^{11} cm^{-2}. To isolate the contribution of the holes directly injected in $MoSe_2$, we changed the pump to 1.75 eV, so that it injects carriers in $MoSe_2$ only, with a density of about 4.4×10^{10} cm^{-2}. It is not energetic enough to excite MoS_2. As the excited electrons transfer to MoS_2 , the signal observed, red symbols in Figure 3.13(b) , is induced by holes in $MoSe_2$. Since the signal is proportional to the hole density, we can deduce the signal corresponding to a hole density of 1.3×10^{11} cm^{-2} by multiplying the observed signal with a factor of 3. The result, open symbols in (b), is in excellent agreement with blue symbols. This comparison confirms that holes injected in MoS_2 transfer to $MoSe_2$ with a near unity efficiency. This interpretation is further confirmed by the systematic variation of the signal measured at 3 ps as the pump photon energy is changed, shown in Figure 3.13(c) . Since the temporal profiles of the two signals are identical, both rising to maximum on a time scale limited by the time resolution of the instrument, the hole transfer process is at least as fast as the instrument response time of 0.3 ps and is faster than the electron transfer.

3.3.5 Long Lifetime of Photocarriers

After the charge transfer, the electrons and holes settle in different layers and are separated by a middle layer, which is expected to extend the carrier lifetime. To probe the lifetime of the electrons in MoS_2 after their transfer from $MoSe_2$, the differential reflection of the 1.88 eV probe was measured over a long time range after the 1.57 eV pump injected a carrier density of 1.1×10^{10} cm^{-2} in $MoSe_2$. As shown by the blue symbols in Figure 3.14(a), the lifetime of these electrons is about 950 ps. This is significantly longer than the 30 ps photocarrier lifetime in MoS_2 monolayer

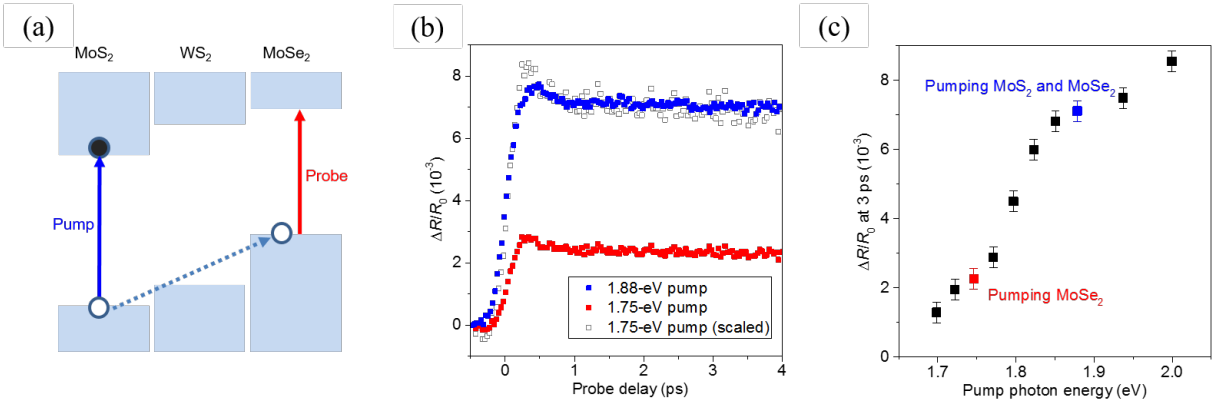

Figure 3.13: (a) Experiment configuration used to study transport of holes from MoS_2 to $MoSe_2$. A 1.88-eV pulse (blue arrow) is used to excite the MoS_2 layer. Holes transferred to $MoSe_2$ are detected by a probe pulse of 1.57-eV (red arrow). (b) Differential reflection signal of the 1.57-eV probe after the three-layer sample is pumped by 1.88 (blue) and 1.75 eV (red) pumps, respectively. (c) The differential reflection signal at a probe delay of 3 ps as a function of the pump photon energy. The two data points corresponding to b are plotted with the corresponding colors. Adapted with permission.[138] Copyright 2017, American Chemical Society

(open symbols), determined by measuring a monolayer MoS_2 sample with the same probe but a 3.14 eV pump. We also probed the lifetime of holes in $MoSe_2$ by using the 1.57 eV probe. As shown in Figure 3.14(b), the lifetime is also significantly extended compared to $MoSe_2$ monolayer and is reasonably consistent with the lifetime of electrons in MoS_2 of the three-layer sample.

3.3.6 Conclusions in MoS_2–WS_2–$MoSe_2$ Three-layer Heterostructure

In summary, we time-resolved the transfer of electrons from $MoSe_2$ to MoS_2 monolayers that are separated by a WS_2 monolayer. The transfer time is about 1.5 ps. Considering the thickness of these monolayers of about 1 nm, such a transfer time corresponds to a speed on the order of 1000 m s^{-1}. Surprisingly, the electrons do not populate the middle WS_2 layer during the transfer, which suggests that the transfer could be a coherent process. Our first-principle calculations reproduced both the transfer time and the coherent nature of the transfer. However, we note that our measurement does not directly monitor the coherence of the transfer due to the incoherent nature of the probe technique. We also observed efficient and ultrafast transfer of holes from MoS_2 to $MoSe_2$. The spatial separation of electrons and holes by the WS_2 layer enhanced their lifetime to about 1

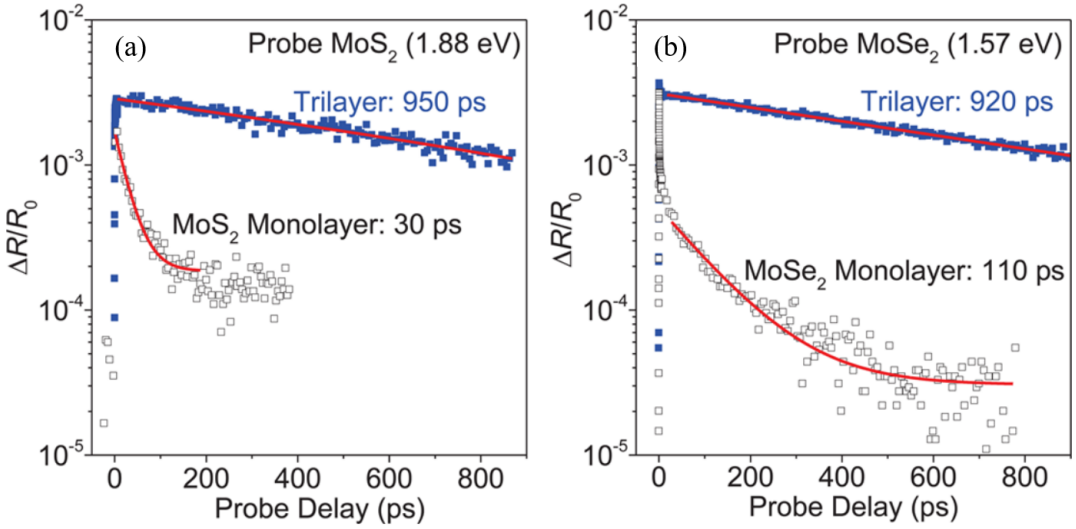

Figure 3.14: (a) Blue solid symbols show the differential reflection of a 1.88 eV probe after a 1.57 eV pump pulse injected carriers with a peak density of 1.1 $\times$ 10^{10} cm^{-2} in the $MoSe_2$ layer of the three-layer sample. Open symbols represent results from a MoS_2 monolayer, with the same probe, but with a 3.14 eV pump pulse that injects carriers with the same density. The red curves are exponential fits. (b) The differential reflection of a 1.57 eV probe after a 2.00 eV pump pulse injected carriers in the three-layer sample (blue solid symbols) and a $MoSe_2$ monolayer (open symbols) with a density of 9.5 $\times$ 10^{10} cm^{-2}. The red curves are exponential fits. Adapted with permission.[138] Copyright 2017, American Chemical Society

ns. These results on efficient charge transfer and long carrier lifetime suggest potential applications of van der Waals multilayers as new electronic and optoelectronic materials.

3.4 Separating Electrons and Holes by Monolayer Increments in van der Waals Heterostructures

In this section we present a systematic study with 2D stacked layered materials, where their properties are tailored monolayer by monolayer. By arranging WSe_2, $MoSe_2$, WS_2, and MoS_2 monolayers in predetermined sequences, that are predicted to have a ladder band alignment in both the conduction and valence bands, we separate electrons and holes between the two utmost layers. The samples studied are a WSe_2 monolayer, a WSe_2–$MoSe_2$ bilayer, a WSe_2–$MoSe_2$–WS_2 trilayer, and a WSe_2–$MoSe_2$–WS_2–MoS_2 four-layer. We observed an increase in absorbance, a decrease in photoluminescence, a variation in interlayer charge transfer, and photocarrier lifetimes that are extended up to a few nanoseconds as additional layers were added. With these results, we demonstrate that van der Waals stacked 2D materials can form effective complex stacks and are promising platforms for fabricating ultra-thin and flexible optoelectronics applications.

3.4.1 Optical Properties and Exciton Lifetimes of WSe_2, $MoSe_2$, WS_2, and MoS_2 Monolayers

To better understand the evolution of the multilayers, we begin by describing the relevant properties of the four component MLs used to fabricate them. To do so, WSe_2, $MoSe_2$, WS_2 and MoS_2 flakes were first prepared on flexible PDMS substrates by mechanical exfoliation from their bulk crystal counterparts (see Appendix A). The ML samples were first identified under a microscope by their optical contrast and then transferred onto either Si–SiO_2 (90 nm) substrates for photoluminescence (PL) and pump-probe spectroscopy studies or quartz substrates for absorption spectroscopy measurements.

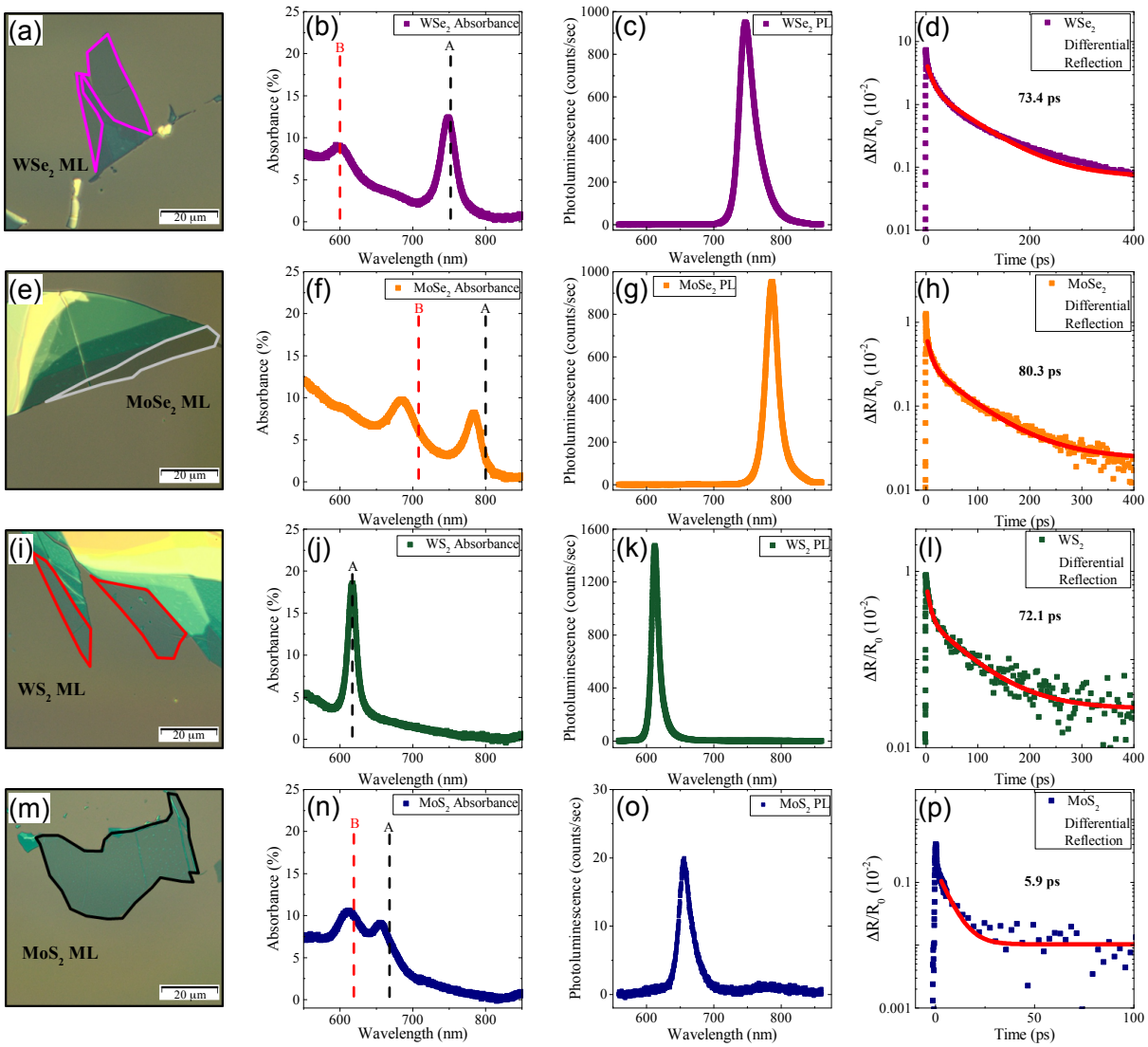

Figure 3.15: (a), (e), (i) and (m): Optical microscopy image of the WSe_2, $MoSe_2$, WS_2, and MoS_2 MLs on a Si–SiO_2 substrate. (b), (f), (j), and (n): Absorbance spectra of WSe_2 (purple), $MoSe_2$ (orange), WS_2 (green), and MoS_2 (blue) MLs. The dashed vertical lines denote previous reported A and B exciton resonances. (c), (g), (k), and (o): Photoluminescence (PL) spectra of the MLs samples measured under the same conditions. (d), (h), (l), and (p): Decay of the transient absorption signal. The solid curves represent bi-exponential fits where the long decay constant extracted are shown in the corresponding panel.

The left column of Figure 3.15 shows the optical microscope images of the individuals MLs on Si–SiO_2. For clarity, the ML regions in these images are identified by the colored outlines. Figure 3.15(b), (f), (j), and (n) show the absorbance of WSe_2 (purple), $MoSe_2$ (orange), WS_2 (green), and MoS_2 (blue) MLs, deduced from reflection measurements. For sufficiently thin samples on

transparent and thick substrates, the absorbance A of the samples can be calculated from the fractional change of reflectance defined as $(R_{S+Q} - R_Q)/R_Q$, where R_{S+Q} and R_Q are, respectively, the reflectance of the sample on quartz and the reflectance of the quartz substrate. The absorbance can be obtained by $A = (1/4)(n^2 - 1)(R_{S+Q} - R_Q)/R_Q$, where n denotes the index of refraction of the substrate.[79] The absorbance and peak positions are consistent with previously reported A and B exciton resonances[141] indicated by the dashed vertical lines. The PL spectra, measured under the excitation of a 405 nm continuous-wave laser with an incident power of 0.5 μW and a spot size of about 1.0 μm, are shown in Figure 3.15(c), (g), (k), and (o). The peak positions of WSe_2 (749 nm), $MoSe_2$ (786 nm), WS_2 (612 nm), and MoS_2 (655 nm) along with the PL yield agree with earlier reports, too.[29,45,80,96] From the optical contrast, the absorption, and the PL spectra, we securely confirm the ML thickness of these samples and their high quality.

To obtain the exciton lifetimes in the MLs, we conducted ultrafast transient absorption measurements in reflection geometry with orthogonal pump–probe polarizations. Here, a linearly polarized and above-resonance pump pulse is used to injected photocarriers which are then monitored by measuring the differential reflection $\Delta R/R_0$ of a time delayed probe pulse tuned to the A exciton resonance of the sample. Panels (d), (h), (l), and (p) in Figure 3.15 present these results with an injected carrier density of 2.0×10^{11} cm^{-2} on each sample. Right after photoexcitation, the signal reaches it maximum value within the instrument response time and starts to immediately decay. The decay of the signal reflects the decay of the exciton population; therefore, by fitting a bi-exponential function (solid curves) we extract the decay constants shown in the the corresponding panels.

3.4.2 Optical Properties of Multilayer Samples

Next, we study the multilayer samples composed from exfoliated MLs. Similar to the fabrication of the isolated MLs, flakes were first exfoliated onto PDMS substrates using adhesive tape and inspected under an optical microscope. The multilayer samples were then composed by precisely transferring different TMDs on top of each other (see Appendix A). This set of sample consist of

WSe_2 ML, WSe_2–$MoSe_2$ bilayer, WSe_2–$MoSe_2$–WS_2 trilayer, and WSe_2– $MoSe_2$–WS_2–MoS_2 four-layer. The particular arrangement of the layers was chosen in order to study the behavior of the electrons and holes has their spatial separation gradually increases. According to first-principle calculations, these multilayers form ladder band alignment.[62,63] As schematically shown in Figure 3.17(a), (d), and (g), the valence band maximum is located in the bottom WSe_2 while the conduction band minimum is in the top layer in all these samples. Consequently, electrons and holes are incline to separate between the layers in order to populate the lower energy states available. Purposely the arrangement of the layers in the multilayer samples maximizes the charge separation.

We study the evolution of the absorption and PL spectra under the same experimental conditions used to study MLs. Starting with two distinctive peaks, previously identified as the A and B exciton resonances, the WSe_2 absorption spectrum [Figure 3.16(b)] shows that at 749 nm the absorbance is about 12%. The optical absorption spectrum of the WSe_2–$MoSe_2$ bilayer, shown as the gray curve in Figure 3.16(e), closely resembles the sum of the individual spectra (black curve) that was obtained by adding the spectra of the composing MLs. Noticeable differences start to be visible when comparing the spectrum from WSe_2–$MoSe_2$–WS_2 trilayer (gray curve) and that put together by summing the composing ML spectra (black curve) shown in Figure 3.16(h). The trilayer sample absorbs approximately 1 - 1.5 times more light over the wavelength range studied with the two evident peaks from WSe_2 and WS_2 red shifted about 10 - 15 nm, which can be attributed to the different dielectric environment present in different samples. Following a similar trend, in the WSe_2–$MoSe_2$–WS_2–MoS_2 four-layer, absorption [gray curve in Figure 3.16(k)] is increased by a factor of 1.5 - 2 when compared to the sum of the four individual ML absorption spectra (black curve). The enhanced absorption in multilayers could be attributed the broadening of the exciton transitions due to the reduced lifetime of excitons in these MLs,[142] which is a consequence of ultrafast charge transfer between these layers and the local field effect in multilayers.[143] The peak absorbance of the four-layer sample, with a thickness d of only 2.5 nm, is about 50%. This corresponds to an absorption coefficient $\alpha = -\ln(1-A)/d = 2.8 \times 10^6$ cm^{-1}, calculated

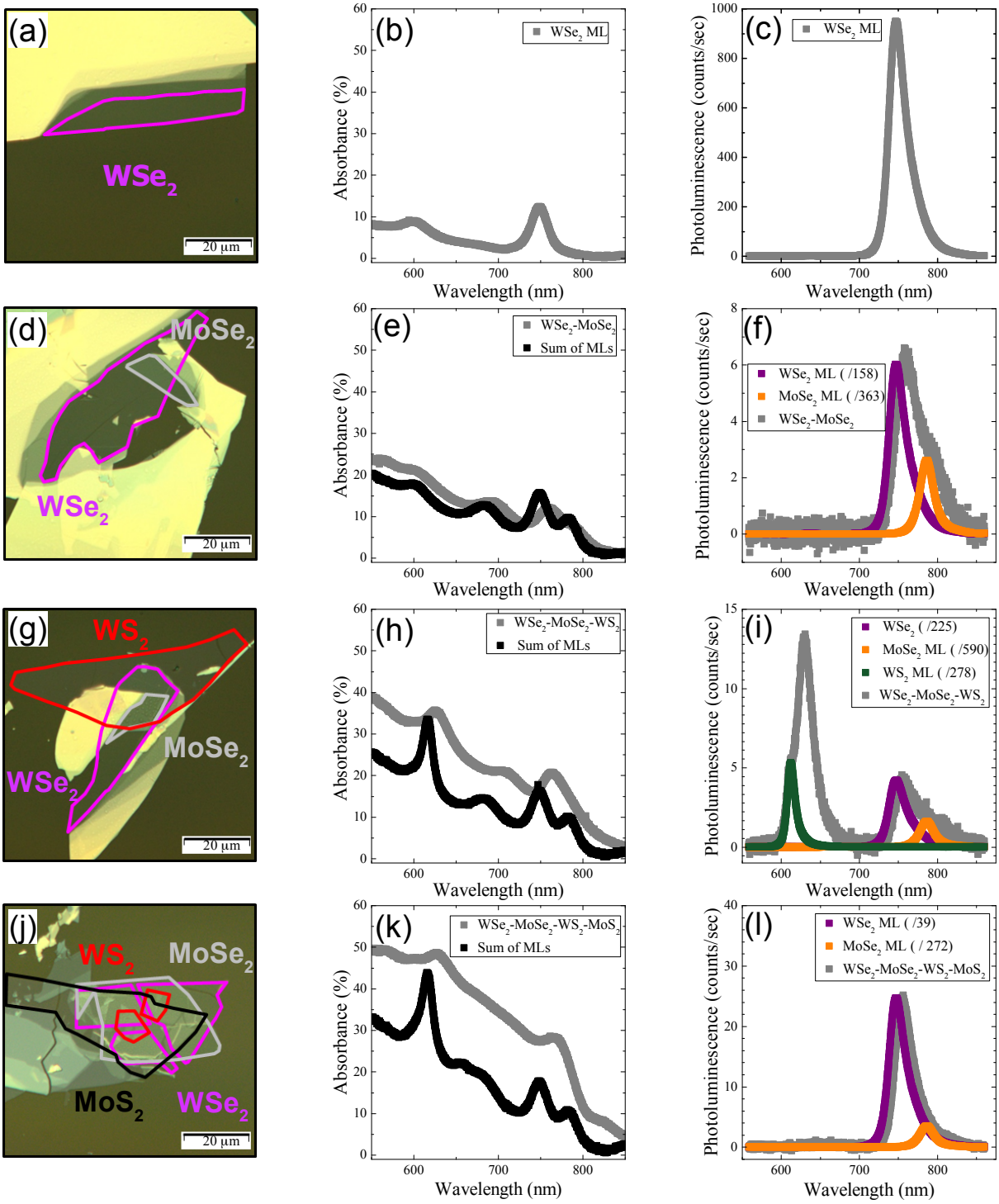

Figure 3.16: Optical images of the WSe_2 ML (a), WSe_2–$MoSe_2$ (d), WSe_2–$MoSe_2$–WS_2 (g), and WSe_2–$MoSe_2$–WS_2–MoS_2 (j) on quartz substrates. The absorption and PL spectra taken under the same experimental conditions (gray curves) for the WSe_2 ML (b) and (c), WSe_2–$MoSe_2$ (e) and (f), WSe_2–$MoSe_2$–WS_2 (h) and (i), and WSe_2–$MoSe_2$–WS_2–MoS_2 (k) and (l). In the absorption spectra panels, the black curves are composed by summing the individual MLs spectra. The quenching factors for the PL peaks are labeled in the legend and are shown as the non-gray curves.

using Beer - Lambert law.[82]

The demonstrated ultrahigh absorbance of such ultrathin films suggests their potential uses in ultrathin and flexible photovoltaic and photodetection devices as a light-absorbing layer. For such applications, the properties of photocarriers, especially their lifetime, are also very important. To understand the photocarrier dynamics in these samples, we first use PL spectroscopy to probe the effectiveness of interlayer charge transfer. Figure 3.16(c) shows the PL spectrum of WSe_2 ML, which displays a pronounce peak at 749 nm. We then measured the PL spectrum from the WSe_2–$MoSe_2$ bilayer, shown as the gray curve in Figure 3.16(f). The PL spectra from WSe_2 (purple) and $MoSe_2$ (orange) MLs are shown with the quenching factors labeled in the legend. The strong quenching of the PL from the bilayer structure is a clear indicator of effective charge transfer; that is, interlayer charge transfer occur on a time scale shorter than the recombination lifetime of excitons. The PL spectrum from the WSe_2–$MoSe_2$–WS_2 trilayer, gray curve in Figure 3.16(i), displays several spectral features. First, the WSe_2 (purple), $MoSe_2$ (orange), and WS_2 (green) PL peaks are quenched by factors of 225, 590, and 278, respectively. Secondly, the appearance of a pronounce fourth peak at 630 nm is displayed, which has been identified as the radiative recombination of trions in a $MoSe_2$–WS_2 sample.[132] Finally, the four-layer PL spectrum, gray curve in Figure 3.16(l), shows one distinctive quenched peak corresponding to the WSe_2 ML. Interestingly, we note that the WSe_2 peak in the four-layer is about 6 times stronger than in the trilayer. The origin of this counter-intuitive observation will be discussed after the time–resolved results are presented.

3.4.3 Probing the Electron Dynamics

Having confirmed that the samples form effective heterojunctions between adjacent layers, we proceed to time–resolve the dynamics of the photocarriers in the multilayer samples with the pump-probe configurations shown in Figure 3.17(a), (d), and (g). Layers that are resonantly (non-resonantly) excited are denoted by the solid (dashed) vertical arrows. To measure the lifetime of the electrons in the WSe_2–$MoSe_2$ sample, we monitor the differential reflection of a probe pulse

tuned near the A exciton resonance of $MoSe_2$ after a pump pulse non-resonantly injects excitons into both WSe_2 and $MoSe_2$ [dashed vertical arrows in Figure 3.17(a)]. The total injected carrier density in the multilayer structures was calculated using Rouard's method that yields the reflection and transmission coefficient R and T, respectively, for a system of k thin films on a thick transparent substrate.[144] It accounts for the reflected photons at each interface and those absorbed within each layer, which allows us to estimate the incident fluence on each layer and thus the injected carriers, see Appendix B for more details. Given that the conduction band minimum is situated in the $MoSe_2$ layer, electrons in the conduction band of WSe_2 are predispose to transfer to $MoSe_2$, pink dashed arrow in (a). Similarly, holes in the valence band of $MoSe_2$ are incline to transfer into WSe_2. Once electrons and holes separate between the layers, they are expected to form charge transfer excitons. As a result of the increase in spatial separation between electron-hole pairs, the electron-hole recombination will be suppress and their lifetime will be extended. Figure 3.17(b) and (c) show the differential reflection of the 790 nm probe in a short and long time scale (blue squares), respectively, where the total injected photocarrier density is 15.0×10^{10} cm^{-2}. The signal immediately reaches its maximum value, within the instrument response function [solid red curve in Figure 3.17(b)], and starts to decay shortly after. The long decay constant of 92 ps shown in Figure 3.17(c), extracted from a bi-exponential fit shown as the solid red curve in Figure 3.17(c), is slightly larger than the lifetime of excitons in $MoSe_2$ ML, see Figure 3.15(h). Moving on to the trilayer sample, the 750 nm pump pulse injects a total of 15.0×10^{10} cm^{-2} excitons into $MoSe_2$ and WSe_2. This time a 620 nm probe pulse is used to detect the presence of electrons in WS_2. As a result of the lower energy of the pump photons, the WS_2 layer is not excited; hence, a strong change in the reflection of the 620 nm probe will be caused only by transferred electrons. Three temporal regions are observed and shown in Figure 3.17(e) and (f): (I) After photoexcitation by the pump pulse, the $\Delta R/R_0$ quickly rises within the first 500 fs as seen in (e). (II) Shortly after, $\Delta R/R_0$ slowly rises and reaches it maximum value around 5 ps. Typically in the ML and bilayer samples, $\Delta R/R_0$ reaches it maximum value in the first 500 fs; however, since the pump excites $MoSe_2$ and WSe_2, two different transfer processes have to occur. We attribute the ultrafast rise

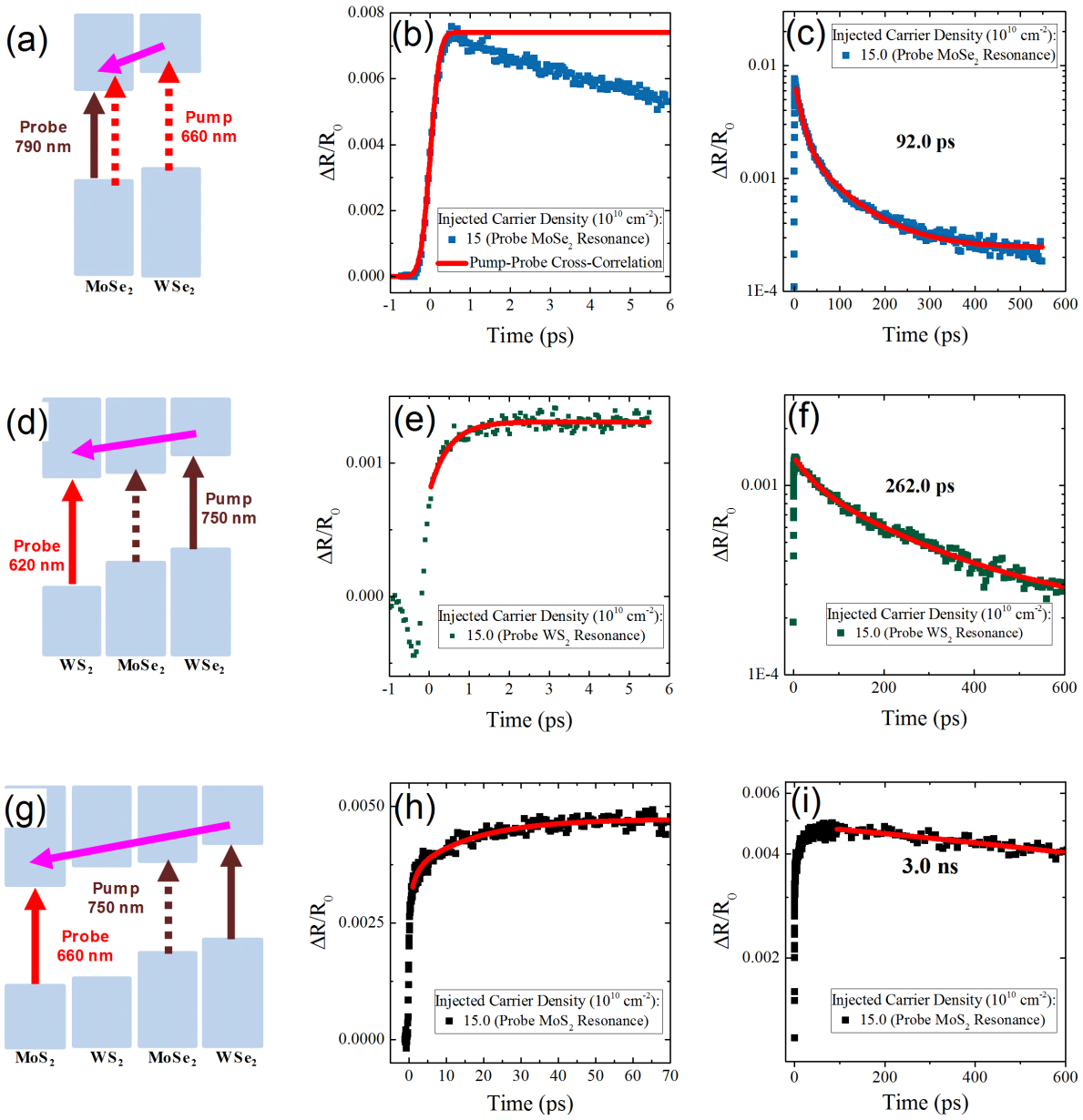

Figure 3.17: (a), (d), and (g) Schematics of the pump-probe configuration used to study the transfer of electrons from different layers into the conduction band minimum. (b) and (c) Differential reflection signal (sensing electrons $MoSe_2$) as function of probe delay in a short (b) and long (c) temporal regions. The solid red curve in (b) is the pump-probe cross-correlation function and in (c) is a bi-exponential fit with the long decay constant shown in the figure. (e) and (f) are the same as (b) and (c) but for the three-layer sample (sensing electrons in WS_2). (h) and (i) show the differential reflection signal in the four-layer structure (sensing electrons in MoS_2 layer) in a short (h) and (i) long time scale. The solid red curves are fits.

of the signal to the transfer of electrons from $MoSe_2$ into WS_2 and the second temporal region to the transfer of electrons from WSe_2 into WS_2. To model the second temporal region, we used $N(t) = N_0[1 - \exp(t/\tau_e)]$, where N_0 is a fraction of the injected density and τ_e is the transfer time, red curve in (e). The extracted transfer time is of 0.37 ± 0.02 ps. (III) Finally, a slow decay of the signal occurs after 5 ps that last a few hundred picoseconds. As it is expected, the lifetime of the electrons in the three-layer sample, shown in panel (f), are extended up to 262 ps.

In the four-layer sample, the 750 nm pump injects excitons into the WSe_2 and $MoSe_2$ layers, leaving the WS_2 and MoS_2 layers unexcited, see Figure 3.17(g). By tuning the probe near the exciton resonance of MoS_2, we observe three temporal regions shown in Figure 3.17(h) and a fourth one in (i): (I) The ultrafast rise of the signal that occurs within the first 500 fs. (II) A relatively fast rise of the signal that occurs within 1-10 ps that we attribute to the transfer of electrons from the $MoSe_2$ (the closer layer) into MoS_2. (III) A very slow rise of the signal from 10 - 70 ps. (IV) A very slow decay shown in Figure 3.17(i).

We attribute the slow rise of the signal in (III) to the transfer of electrons from the bottom WSe_2 to the top MoS_2 layer in this four-layer structure. This assignment is supported by the decay of the exciton population in the WSe_2 ML. As shown in Figure 3.15(d), about 90% of the injected excitons in the WSe_2 ML decays in 70 ps due to their recombination. This is approximately the rising time observed in the four-layer. The PL of the three-layer [Figure 3.16(i)] and the four-layer samples [Figure 3.16(l)] at 755 nm (corresponding to WSe_2) is 4 and 24 counts per second, respectively. The higher PL yield from the four-layer sample indicates that a higher fraction of electrons recombine in the WSe_2 layer of the four-layer sample as a consequence of a less efficient electron transfer, further supporting this interpretation. The rise of the signal in temporal regions (II) and (III) is modeled by $N(t) = N_0[1 - \exp(t/\tau_e)]$. From the fit shown in Figure 3.17(h) and others not shown, we obtain the transfer times of 1.4 ± 0.6 ps and 14.9 ± 1.8 ps, respectively.

Finally, the slow decay of the signal after 70 ps shown in Figure 3.17(i) is attributed to the extremely long lifetime of electrons in MoS_2. By fitting a single exponential function to the decay of the signal (the red curve), we extract electrons lifetimes of about 3.0 ns. Compared to the

lifetime of excitons in individual MLs, the electron lifetime in the four-layer sample is extended several hundred times.

3.4.4 Probing the Hole Dynamics

We also measured the lifetime of holes in these samples. To do so we used the pump probe configurations shown in Figure 3.18(a), (d), and (g). Here a 620 nm pump excites all the layers and a 750 nm probe monitors the presence of holes in WSe_2 where the valence band maximum resides. The short scale dynamics are shown in Figure 3.18(b), (e), and (h) whereas the long scale dynamics are shown in Figure 3.18(c), (f), and (i). Two temporal regions are observed. (I) The ultrafast rise time that occurs in the first picosecond and (II) the decay of the signal after $\Delta R/R_0$ has reached it maximum value. Since holes directly injected in WSe_2 give rise to a fast rise of the signal, the transfer of holes from other layers is difficult to be analyzed. By analyzing the decay of the signal, we found a systematic increase in the hole lifetime from 133.8 ps up to 2.3 ns as the number of layers is increased, as shown in Figure 3.18(c), (f), and (i). The hole lifetime in the four-layer sample is reasonably consistent with the electron lifetime, as expected.

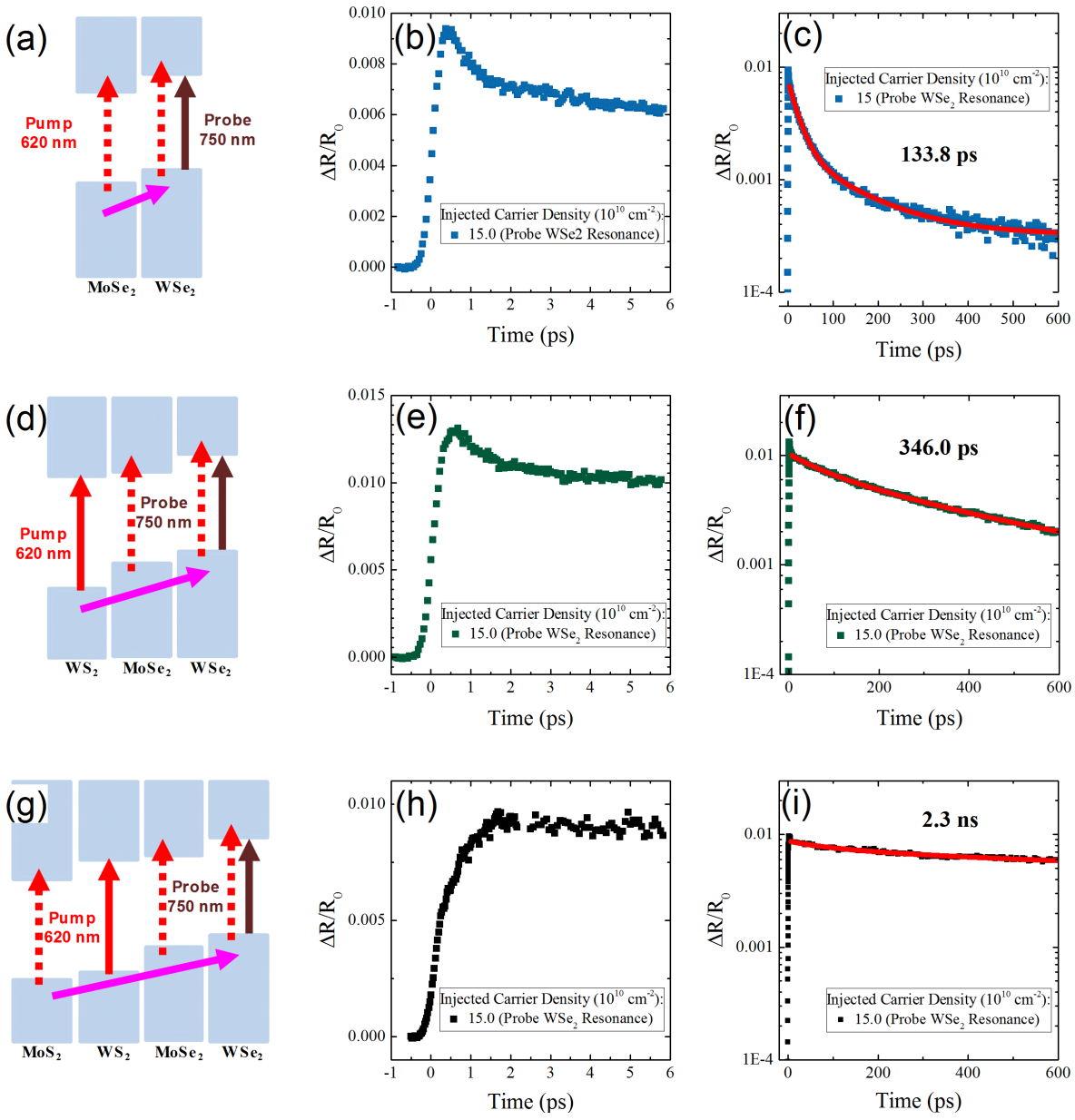

Figure 3.18: (a), (d), and (g) Schematics of the pump-probe configuration used to study the transfer of holes from different layers into the valence band maximum. As additional layers are added, the lifetime of the holes was measured in different regimes. The short time scale regime results are shown in (b), (e), and (h) while the long scale regime results are shown in panels (c), (f), and (i). The solid red curves are exponential fits with the extracted lifetime constants shown in the corresponding panel.

3.4.5 Summary

In summary, by using four different TMD MLs, we have fabricated a set of samples of bilayer WSe_2–$MoSe_2$, trilayer WSe_2–$MoSe_2$–WS_2, and four-layer WSe_2–$MoSe_2$–WS_2–MoS_2, and characterize their properties by conducting absorption, PL, and ultrafast pump-probe spectroscopy measurements. These specific set of multilayer samples were chosen with the intention of studying the behavior of electrons and holes as they are further separated from each other. The presented multilayer samples were atomically engineer to precisely achieve this purpose. We observed that the absorbance is higher in the multilayer structures when compared to the sum of the individual absorbances from the constituent MLs. Moreover, from the PL results we confirmed that we can effectively put up to four different semiconducting layers together with high quality interfaces that allow efficient interlayer charge transfer. We were able to time resolve the transfer of electrons between the layers and quantified how the lifetime of the electrons and holes was extended as additional layers were added. We show that the four-layer sample with a thickness of just a few nanometers has an absorbance as high as 50% in the visible range, an effective absorption coefficient of 3.5×10^6 cm^{-1}, and photocarrier lifetimes of several nanoseconds. Their novel properties suggests promising potential applications in ultrathin, flexible, and efficient photovoltaic and photodetection devices. Furthermore, we demonstrated an approach for fabricating van der Waals multilayers that can be used to produce more complex multilayer structures with the desired band alignment and optoelectronic properties for various applications.

Chapter 4

Summary and Outlook

Since WSe_2, $MoSe_2$, WS_2, and MoS_2 TMDs are direct band gap semiconductors in monolayer form, flexible, stable at room temperature, and efficiently absorb light in the visible regime, they have become attractive candidates for a variety of ultrathin optoelectronics applications. Nonetheless, it has been demonstrated that their real potential and that of other 2D materials lies when combining different 2D materials to form multilayer structures which allows the fine tuning of their electronic properties.

To noninvasively study the properties of 2D materials and that of the van der Waals multilayer structures, photoluminescence, absorption, and ultrafast laser spectroscopy techniques were employed. First, by using photoluminescence spectroscopy the electronic structure of the 2D materials as well as the charge transfer in multilayer structures was probed. To measure how effective our 2D samples and multilayer structures were at absorbing light, absorption spectroscopy measurements were carried.

Next ultrafast laser spectroscopy measurements were discussed. In our measurements, both the pump and probe beam are focused on sample by a microscope objective lens, reflected, and collimated by the same objective lens. The reflected beams are then redirected into a set of filters that prevent the pump from going through. The probe beam that makes it through the set of filters is then focused onto a photodiode which output is sent to a lock-in amplifier. Here, the

interband excitation which results from the pump photoexcitation injects a nonthermal distribution of electrons and holes which quickly evolves into a thermal distribution within 20 fs via both carrier-carrier and carrier-phonon scattering. Since the newly formed thermal distribution is at much higher temperature than the lattice temperature, energy relaxation occurs and within the next 0.6 ps it brings the photocarrier system into a quasi-equilibrium state with the phonon system through a process that occurs via carrier-phonon scattering. The photocarriers then form excitons which recombine radiatively or nonradiatively, returning the system to the equilibrium state before the photoexcitation. The dynamics of the photocarriers injected by the pump is monitored by measuring the the normalized change of reflection of the probe beam, which is directly proportional to the photocarrier density, at different probe delays and positions relative to the pump beam. In the case of multilayer structures, depending on the pump–probe configuration, the ultrafast laser spectroscopy technique can be used to selectively injected carriers into specific layers while probing for their presence in different layers. In this way, information about the photocarrier lifetimes, their diffusion, and transferring between the layers can be obtained.

The aforementioned techniques were used to study the photocarrier dynamics in different multilayer structures with a type II or ladder band alignment. In the MoS_2–$MoSe_2$ bilayer heterostructure, the strong quenching of the photoluminescence provided evidence of the effective charge transfer between the layers. By using the ultrafast pump probe technique and tuning the pump beam to excite only the $MoSe_2$ layer of the bilayer heterostructure, the strong differential signal that originated from the probe beam tuned to the MoS_2 resonance allowed us to determine that the charge transfer occurred in an ultrafast time scale. Moreover, the photocarriers lifetimes were extended due to the separation of charge between the layers which reduces the overlap of the electron and hole wave functions. Moving on the $MoSe_2$–WS_2 bilayer heterostructure, our photoluminescence measurements indicated that the charge transfer was effective and that the charge transfer exciton states were approximately 50 meV below the $MoSe_2$ exciton states, with a significant spectral overlap. This time, the transient absorption of a femtosecond pulse was monitored in order to study the spatial and temporal dynamics of the charge transfer excitons at room temperature. A

lifetime of approximately 80 ps and a diffusion coefficient of 14 cm^2 $s^{-1}$was deduced for the charge transfer excitons.

To successfully implement multilayer structures in logic electronics, thin-film transistors, and optoelectronics, is important to understand and control the interlayer electron transfer process. Most efforts so far have focused on bilayer heterostructures which have laid the foundation in understanding certain key aspects of multilayer structures. For example, steady state optical measurements reveal the effective charge transfer between different monolayers from the quenching of the photoluminescence. While transient absorption measurements are typically used to selectively excite and probe different layers to determine the charge transfer time as well quantify the extended lifetimes of the photocarriers. Due to the weak interlayer coupling and the large momentum mismatch between these atomic layers, such a fast transfer is rather surprising. Although various mechanisms have been proposed, there is still a lack of understanding on how this process can be so efficient at van der Waals interfaces. Using a MoS_2–WS_2–$MoSe_2$ three-layer sample, we showed evidence suggesting the coherent nature of the interlayer electron transfer. It was determined that when electrons are excited in $MoSe_2$ they transfer to MoS_2 in about one picosecond. Surprisingly, these electrons do not populate the middle WS_2 layer during this process. Moreover, calculations reproduced the coherent nature of the electron charge transfer and closely replicated the measured electron transfer time. The hole transfer from MoS_2 to $MoSe_2$ is also found to be efficient and ultrafast. By adding an additional layer to separate electrons and holes between the two outmost layers, their lifetimes were extended up to one nanosecond, suggesting potential applications of such multilayer structures in optoelectronics.

Finally, a systematic study with 2D stacked layered materials was presented where their properties were tailored monolayer by monolayer. Here, WSe_2, $MoSe_2$, WS_2, and MoS_2 monolayers were arranged in predetermined sequences predicted to have a ladder band alignment in both the conduction and valence bands. Such type of band alignment encourages the separation of charge between the constituent monolayers with the electrons and holes settling in the outmost layers. The samples made were WSe_2 monolayer, WSe_2–$MoSe_2$, WSe_2–$MoSe_2$–WS_2, and WSe_2–$MoSe_2$–

WS_2–MoS_2. In these samples as the number of layers was increased, an increase in absorbance, a decrease in photoluminescence, a variation in the interlayer charge transfer, and an increase in the photocarrier lifetime can systematically be observed. Moreover, the 4-layer sample with a thickness of just a few nanometers showed an absorbance as high as 50% in the visible regime which translates to an effective absorption coefficient of 3.5×10^6 cm^{-1} with photocarrier lifetimes extending up to a few nanoseconds. With these results, is once more demonstrated that van der Waals stacked 2D materials can form effective complex stacks and are promising platforms for fabricating ultra-thin and flexible optoelectronics applications.

With the research on 2D materials rapidly intensifying and showing no signs of settling down, it is inevitable that the same type of interest will be invested van der Waals multilayer structures. As some scientist search for new 2D materials, others are fabricating single layer transistors, solar cells, and photodetectors out of them while others are manually stacking 2D materials and showing that particular combinations deserve more attention. This effectively motivates and leads the development of chemically grown van der Waals heterostructures. Although what joins together different type of 2D materials is the weak van der Waals force, the interaction between adjacent layers is strong enough so that the electronic properties of the resulting stack can be tuned by selection of materials, sequence in which they are arrange, and orientation between the layers. Additionally, different external knobs such implementation of chemical methods to slightly change the 2D material properties, and the application of electrical, mechanical, and optical stresses allow for the finer tuning of the electrical properties in van der Waals stacked 2D materials. It is almost certain that the most exciting 2D materials are yet to be discovered and that individual 2D materials will become the basic building blocks of complex heterostructures offering precise tuning of their electronic properties. However, as the research moves forward new problems begin to emerge. For example, as new 2D materials are discovered through the mechanical exfoliation technique and new combinations of manually stacked 2D materials are formed, their scalable high quality large scale growth becomes a new issue for researchers. As of today, the current research remains at a proof of concept level with still a large area of unexplored possible bilayer heterostructures.

By stacking additional layers this enormously increases the number of possible permutations of different 2D materials. With a lot yet to be discovered, van der Waals stacked 2D materials offer rich fundamental research and functional optoelectronic applications in the years to come.

References

[1] A. R. Guichard, D. N. Barsic, S. Sharma, T. I. Kamins, and M. L. Brongersma, "Tunable light emission from quantum-confined excitons in $TiSi_2$-catalyzed silicon nanowires," *Nano Letters*, vol. 6, no. 9, pp. 2140–2144, Sep 2006. [Online]. Available: https://doi.org/10.1021%2Fnl061287m

[2] L. D. Landau and E. M. Lifshitz, *Statistical Physics, Part I*. Oxford: Pergamon Press, 1980.

[3] K. S. Novoselov, D. Jiang, F. Schedin, T. J. Booth, V. V. Khotkevich, S. V. Morozov, and A. K. Geim, "Two-dimensional atomic crystals," *Proceedings of the National Academy of Sciences of the United States of America*, vol. 102, no. 30, pp. 10 451–10 453, 2005. [Online]. Available: http://www.pnas.org/content/102/30/10451.abstract

[4] A. K. Geim and K. S. Novoselov, "The rise of graphene," *Nature Materials*, vol. 6, no. 3, pp. 183–191, Mar 2007. [Online]. Available: https://doi.org/10.1038%2Fnmat1849

[5] C. Lee, X. Wei, J. W. Kysar, and J. Hone, "Measurement of the elastic properties and intrinsic strength of monolayer graphene," *Science*, vol. 321, no. 5887, pp. 385–388, 2008. [Online]. Available: http://www.sciencemag.org/content/321/5887/385.abstract

[6] J. S. Bunch, S. S. Verbridge, J. S. Alden, A. M. van der Zande, J. M. Parpia, H. G. Craighead, and P. L. McEuen, "Impermeable atomic membranes from graphene sheets," *Nano Letters*, vol. 8, no. 8, pp. 2458–2462, Aug 2008. [Online]. Available: http://dx.doi.org/10.1021/nl801457b

[7] S. Bae, H. Kim, Y. Lee, X. Xu, J.-S. Park, Y. Zheng, J. Balakrishnan, T. Lei, H. Ri Kim, Y. I. Song, Y.-J. Kim, K. S. Kim, B. Özyilmaz, J.-H. Ahn, B. H. Hong, and S. Iijima, "Roll-to-roll production of 30-inch graphene films for transparent electrodes," *Nature Nanotechnology*, vol. 5, pp. 574–578, Aug. 2010.

[8] C. R. Dean, A. F. Young, I. Meric, C. Lee, L. Wang, S. Sorgenfrei, K. Watanabe, T. Taniguchi, P. Kim, K. L. Shepard, and J. Hone, "Boron nitride substrates for high-quality graphene electronics," *Nature Nanotech*, vol. 5, no. 10, pp. 722–726, Aug 2010. [Online]. Available: http://dx.doi.org/10.1038/nnano.2010.172

[9] M. S. Bresnehan, M. J. Hollander, M. Wetherington, M. LaBella, K. A. Trumbull, R. Cavalero, D. W. Snyder, and J. A. Robinson, "Integration of hexagonal boron nitride with quasi-freestanding epitaxial graphene: Toward wafer-scale, high-performance devices," *ACS Nano*, vol. 6, no. 6, pp. 5234–5241, Jun 2012. [Online]. Available: http://dx.doi.org/10.1021/nn300996t

[10] E. Gibney, "The super materials that could trump graphene," *Nature*, vol. 522, no. 7556, pp. 274–276, Jun 2015. [Online]. Available: http://dx.doi.org/10.1038/522274a

[11] L. Tao, E. Cinquanta, D. Chiappe, C. Grazianetti, M. Fanciulli, M. Dubey, A. Molle, and D. Akinwande, "Silicene field-effect transistors operating at room temperature," *Nature Nanotech*, vol. 10, no. 3, pp. 227–231, Feb 2015. [Online]. Available: http://dx.doi.org/10.1038/nnano.2014.325

[12] M. E. Dávila, L. Xian, S. Cahangirov, A. Rubio, and G. L. Lay, "Germanene: a novel two-dimensional germanium allotrope akin to graphene and silicene," *New Journal of Physics*, vol. 16, no. 9, p. 095002, Sep 2014. [Online]. Available: http://dx.doi.org/10.1088/1367-2630/16/9/095002

[13] X. Xi, L. Zhao, Z. Wang, H. Berger, L. Forró, J. Shan, and K. F. Mak, "Strongly enhanced

charge-density-wave order in monolayer $NbSe_2$," *Nature Nanotechnology*, vol. 10, no. 9, pp. 765–769, Jul 2015. [Online]. Available: https://doi.org/10.1038%2Fnnano.2015.143

[14] Z. Lin, A. McCreary, N. Briggs, S. Subramanian, K. Zhang, Y. Sun, X. Li, N. J. Borys, H. Yuan, S. K. Fullerton-Shirey, A. Chernikov, H. Zhao, S. McDonnell, A. M. Lindenberg, K. Xiao, B. J. LeRoy, M. Drndić, J. C. M. Hwang, J. Park, M. Chhowalla, R. E. Schaak, A. Javey, M. C. Hersam, J. Robinson, and M. Terrones, "2D materials advances: from large scale synthesis and controlled heterostructures to improved characterization techniques, defects and applications," *2D Materials*, vol. 3, no. 4, p. 042001, Dec 2016. [Online]. Available: https://doi.org/10.1088%2F2053-1583%2F3%2F4%2F042001

[15] H. J. Conley, B. Wang, J. I. Ziegler, R. F. Haglund, S. T. Pantelides, and K. I. Bolotin, "Bandgap engineering of strained monolayer and bilayer MoS_2," *Nano Letters*, vol. 13, no. 8, pp. 3626–3630, Aug 2013. [Online]. Available: https://doi.org/10.1021%2Fnl4014748

[16] S. B. Desai, G. Seol, J. S. Kang, H. Fang, C. Battaglia, R. Kapadia, J. W. Ager, J. Guo, and A. Javey, "Strain-induced indirect to direct bandgap transition in multilayer WSe_2," *Nano Letters*, vol. 14, no. 8, pp. 4592–4597, Aug 2014. [Online]. Available: https://doi.org/10.1021%2Fnl501638a

[17] K. F. Mak, C. Lee, J. Hone, J. Shan, and T. F. Heinz, "Atomically Thin MoS_2: A new direct-gap semiconductor," *Physical Review Letters*, vol. 105, no. 13, Sep 2010. [Online]. Available: https://doi.org/10.1103%2Fphysrevlett.105.136805

[18] A. Splendiani, L. Sun, Y. Zhang, T. Li, J. Kim, C.-Y. Chim, G. Galli, and F. Wang, "Emerging photoluminescence in monolayer MoS_2," *Nano Letters*, vol. 10, no. 4, pp. 1271–1275, Apr 2010. [Online]. Available: https://doi.org/10.1021%2Fnl903868w

[19] K. M. McCreary, A. T. Hanbicki, G. G. Jernigan, J. C. Culbertson, and B. T. Jonker, "Synthesis of large-area WS_2 monolayers with exceptional photoluminescence," *Scientific*

Reports, vol. 6, p. 19159, Jan 2016. [Online]. Available: https://doi.org/10.1038%2Fsrep19159

[20] H. Nan, Z. Wang, W. Wang, Z. Liang, Y. Lu, Q. Chen, D. He, P. Tan, F. Miao, X. Wang, J. Wang, and Z. Ni, "Strong photoluminescence enhancement of MoS_2 through defect engineering and oxygen bonding," *ACS Nano*, vol. 8, no. 6, pp. 5738–5745, Jun 2014. [Online]. Available: https://doi.org/10.1021%2Fnn500532f

[21] Y. Li, "Measurement of the optical dielectric function of monolayer transition metal dichalcogenides:MoS_2,$MoSe_2$,WS_2, andWSe_2," in *Probing the Response of Two-Dimensional Crystals by Optical Spectroscopy*. Springer Nature, Nov 2015, pp. 33–43. [Online]. Available: https://doi.org/10.1007%2F978-3-319-25376-3_5

[22] D. Xiao, G.-B. Liu, W. Feng, X. Xu, and W. Yao, "Coupled spin and valley physics in monolayers of MoS_2 and other group-VI dichalcogenides," *Physical Review Letters*, vol. 108, no. 19, May 2012. [Online]. Available: https://doi.org/10.1103%2Fphysrevlett.108.196802

[23] H. Zeng, J. Dai, W. Yao, D. Xiao, and X. Cui, "Valley polarization in MoS_2 monolayers by optical pumping," *Nature Nanotechnology*, vol. 7, no. 8, pp. 490–493, Jun 2012. [Online]. Available: https://doi.org/10.1038%2Fnnano.2012.95

[24] K. F. Mak, K. He, J. Shan, and T. F. Heinz, "Control of valley polarization in monolayer MoS_2 by optical helicity," *Nature Nanotechnology*, vol. 7, no. 8, pp. 494–498, Jun 2012. [Online]. Available: https://doi.org/10.1038%2Fnnano.2012.96

[25] A. M. Jones, H. Yu, N. J. Ghimire, S. Wu, G. Aivazian, J. S. Ross, B. Zhao, J. Yan, D. G. Mandrus, D. Xiao, W. Yao, and X. Xu, "Optical generation of excitonic valley coherence in monolayer WSe_2," *Nature Nanotechnology*, vol. 8, no. 9, pp. 634–638, Aug 2013. [Online]. Available: https://doi.org/10.1038%2Fnnano.2013.151

[26] K. F. Mak, K. He, C. Lee, G. H. Lee, J. Hone, T. F. Heinz, and J. Shan, "Tightly bound trions in monolayer MoS_2," *Nature Materials*, vol. 12, no. 3, pp. 207–211, Dec 2012. [Online]. Available: https://doi.org/10.1038%2Fnmat3505

[27] J. S. Ross, S. Wu, H. Yu, N. J. Ghimire, A. M. Jones, G. Aivazian, J. Yan, D. G. Mandrus, D. Xiao, W. Yao, and X. Xu, "Electrical control of neutral and charged excitons in a monolayer semiconductor," *Nature Communications*, vol. 4, p. 1474, Feb 2013. [Online]. Available: https://doi.org/10.1038%2Fncomms2498

[28] A. Chernikov, T. C. Berkelbach, H. M. Hill, A. Rigosi, Y. Li, O. B. Aslan, D. R. Reichman, M. S. Hybertsen, and T. F. Heinz, "Exciton binding energy and nonhydrogenic rydberg series in monolayerWS_2," *Physical Review Letters*, vol. 113, no. 7, Aug 2014. [Online]. Available: https://doi.org/10.1103%2Fphysrevlett.113.076802

[29] K. He, N. Kumar, L. Zhao, Z. Wang, K. F. Mak, H. Zhao, and J. Shan, "Tightly bound excitons in monolayer WSe_2," *Physical Review Letters*, vol. 113, no. 2, Jul 2014. [Online]. Available: https://doi.org/10.1103%2Fphysrevlett.113.026803

[30] H. Zeng, G.-B. Liu, J. Dai, Y. Yan, B. Zhu, R. He, L. Xie, S. Xu, X. Chen, W. Yao, and X. Cui, "Optical signature of symmetry variations and spin-valley coupling in atomically thin tungsten dichalcogenides," *Scientific Reports*, vol. 3, Apr 2013. [Online]. Available: https://doi.org/10.1038%2Fsrep01608

[31] N. Kumar, S. Najmaei, Q. Cui, F. Ceballos, P. M. Ajayan, J. Lou, and H. Zhao, "Second harmonic microscopy of monolayer MoS_2," *Physical Review B*, vol. 87, no. 16, Apr 2013. [Online]. Available: https://doi.org/10.1103%2Fphysrevb.87.161403

[32] L. M. Malard, T. V. Alencar, A. P. M. Barboza, K. F. Mak, and A. M. de Paula, "Observation of intense second harmonic generation from MoS_2 atomic crystals," *Physical Review B*, vol. 87, no. 20, May 2013. [Online]. Available: https://doi.org/10.1103%2Fphysrevb.87.201401

[33] X. Yin, Z. Ye, D. A. Chenet, Y. Ye, K. OBrien, J. C. Hone, and X. Zhang, "Edge nonlinear optics on a MoS_2 atomic monolayer," *Science*, vol. 344, no. 6183, pp. 488–490, May 2014. [Online]. Available: https://doi.org/10.1126%2Fscience.1250564

[34] D. Akinwande, N. Petrone, and J. Hone, "Two-dimensional flexible nanoelectronics," *Nature Communications*, vol. 5, p. 5678, Dec 2014. [Online]. Available: https://doi.org/10.1038%2Fncomms6678

[35] B. W. H. Baugher, H. O. H. Churchill, Y. Yang, and P. Jarillo-Herrero, "Optoelectronic devices based on electrically tunable p–n diodes in a monolayer dichalcogenide," *Nature Nanotechnology*, vol. 9, no. 4, pp. 262–267, Mar 2014. [Online]. Available: https://doi.org/10.1038%2Fnnano.2014.25

[36] A. Pospischil, M. M. Furchi, and T. Mueller, "Solar-energy conversion and light emission in an atomic monolayer p–n diode," *Nature Nanotechnology*, vol. 9, no. 4, pp. 257–261, mar 2014. [Online]. Available: https://doi.org/10.1038%2Fnnano.2014.14

[37] Y. J. Zhang, T. Oka, R. Suzuki, J. T. Ye, and Y. Iwasa, "Electrically switchable chiral light-emitting transistor," *Science*, vol. 344, no. 6185, pp. 725–728, Apr 2014. [Online]. Available: https://doi.org/10.1126%2Fscience.1251329

[38] J. S. Ross, P. Klement, A. M. Jones, N. J. Ghimire, J. Yan, D. G. Mandrus, T. Taniguchi, K. Watanabe, K. Kitamura, W. Yao, D. H. Cobden, and X. Xu, "Electrically tunable excitonic light-emitting diodes based on monolayer WSe_2 p–n junctions," *Nature Nanotechnology*, vol. 9, no. 4, pp. 268–272, Mar 2014. [Online]. Available: https://doi.org/10.1038%2Fnnano.2014.26

[39] B. Radisavljevic, A. Radenovic, J. Brivio, V. Giacometti, and A. Kis, "Single-layer MoS_2 transistors," *Nature Nanotechnology*, vol. 6, no. 3, pp. 147–150, Jan 2011. [Online]. Available: https://doi.org/10.1038%2Fnnano.2010.279

[40] B. Radisavljevic and A. Kis, "Mobility engineering and a metal–insulator transition in monolayer MoS_2," *Nature Materials*, vol. 12, no. 9, pp. 815–820, Jun 2013. [Online]. Available: https://doi.org/10.1038%2Fnmat3687

[41] B. Radisavljevic, M. B. Whitwick, and A. Kis, "Integrated circuits and logic operations based on single-layer MoS_2," *ACS Nano*, vol. 5, no. 12, pp. 9934–9938, Dec 2011. [Online]. Available: https://doi.org/10.1021%2Fnn203715c

[42] H. Wang, L. Yu, Y.-H. Lee, Y. Shi, A. Hsu, M. L. Chin, L.-J. Li, M. Dubey, J. Kong, and T. Palacios, "Integrated circuits based on bilayer MoS_2 transistors," *Nano Letters*, vol. 12, no. 9, pp. 4674–4680, 2012, pMID: 22862813. [Online]. Available: http://dx.doi.org/10.1021/nl302015v

[43] V. V. Gobre and A. Tkatchenko, "Scaling laws for van der Waals interactions in nanostructured materials," *Nature Communications*, vol. 4, Aug 2013. [Online]. Available: https://doi.org/10.1038%2Fncomms3341

[44] M. Z. Bellus, M. Li, S. D. Lane, F. Ceballos, Q. Cui, X. C. Zeng, and H. Zhao, "Type-I van der Waals heterostructure formed by MoS_2 and ReS_2 monolayers," *Nanoscale Horiz.*, vol. 2, no. 1, pp. 31–36, 2017. [Online]. Available: https://doi.org/10.1039%2Fc6nh00144k

[45] F. Ceballos, M. Z. Bellus, H.-Y. Chiu, and H. Zhao, "Ultrafast charge separation and indirect exciton formation in a MoS_2–$MoSe_2$ van der Waals heterostructure," *ACS Nano*, vol. 8, no. 12, pp. 12 717–12 724, Dec 2014. [Online]. Available: http://dx.doi.org/10.1021/nn505736z

[46] M. Bokdam, P. A. Khomyakov, G. Brocks, Z. Zhong, and P. J. Kelly, "Electrostatic doping of graphene through ultrathin hexagonal boron nitride films," *Nano Letters*, vol. 11, no. 11, pp. 4631–4635, Nov 2011. [Online]. Available: https://doi.org/10.1021%2Fnl202131q

[47] S. Das, W. Zhang, M. Demarteau, A. Hoffmann, M. Dubey, and A. Roelofs, "Tunable

transport gap in phosphorene," *Nano Letters*, vol. 14, no. 10, pp. 5733–5739, Oct 2014. [Online]. Available: https://doi.org/10.1021%2Fnl5025535

[48] R. Quhe, J. Zheng, G. Luo, Q. Liu, R. Qin, J. Zhou, D. Yu, S. Nagase, W.-N. Mei, Z. Gao, and J. Lu, "Tunable and sizable band gap of single-layer graphene sandwiched between hexagonal boron nitride," *NPG Asia Materials*, vol. 4, no. 2, p. e6, Feb 2012. [Online]. Available: https://doi.org/10.1038%2Fam.2012.10

[49] L. Britnell, R. M. Ribeiro, A. Eckmann, R. Jalil, B. D. Belle, A. Mishchenko, Y.-J. Kim, R. V. Gorbachev, T. Georgiou, S. V. Morozov, A. N. Grigorenko, A. K. Geim, C. Casiraghi, A. H. C. Neto, and K. S. Novoselov, "Strong light-matter interactions in heterostructures of atomically thin films," *Science*, vol. 340, no. 6138, pp. 1311–1314, May 2013. [Online]. Available: https://doi.org/10.1126%2Fscience.1235547

[50] G. C. Constantinescu and N. D. M. Hine, "Energy landscape and band-structure tuning in realistic MoS_2/$MoSe_2$ heterostructures," *Physical Review B*, vol. 91, no. 19, May 2015. [Online]. Available: https://doi.org/10.1103%2Fphysrevb.91.195416

[51] K. Liu, L. Zhang, T. Cao, C. Jin, D. Qiu, Q. Zhou, A. Zettl, P. Yang, S. G. Louie, and F. Wang, "Evolution of interlayer coupling in twisted molybdenum disulfide bilayers," *Nature Communications*, vol. 5, p. 4966, Sep 2014. [Online]. Available: https://doi.org/10.1038%2Fncomms5966

[52] S. Huang, X. Ling, L. Liang, J. Kong, H. Terrones, V. Meunier, and M. S. Dresselhaus, "Probing the interlayer coupling of twisted bilayer MoS_2 using photoluminescence spectroscopy," *Nano Letters*, vol. 14, no. 10, pp. 5500–5508, Oct 2014. [Online]. Available: https://doi.org/10.1021%2Fnl5014597

[53] K. Wang, B. Huang, M. Tian, F. Ceballos, M.-W. Lin, M. Mahjouri-Samani, A. Boulesbaa, A. A. Puretzky, C. M. Rouleau, M. Yoon, H. Zhao, K. Xiao, G. Duscher, and D. B. Geohegan, "Interlayer coupling in twisted WSe_2/WS_2 bilayer heterostructures revealed

by optical spectroscopy," *ACS Nano*, vol. 10, no. 7, pp. 6612–6622, Jul 2016. [Online]. Available: https://doi.org/10.1021%2Facsnano.6b01486

[54] P. Hu, J. Ye, X. He, K. Du, K. K. Zhang, X. Wang, Q. Xiong, Z. Liu, H. Jiang, and C. Kloc, "Control of radiative exciton recombination by charge transfer induced surface dipoles in MoS_2 and WS_2 monolayers," *Scientific Reports*, vol. 6, p. 24105, Apr 2016. [Online]. Available: https://doi.org/10.1038%2Fsrep24105

[55] P. Rivera, J. R. Schaibley, A. M. Jones, J. S. Ross, S. Wu, G. Aivazian, P. Klement, K. Seyler, G. Clark, N. J. Ghimire, J. Yan, D. G. Mandrus, W. Yao, and X. Xu, "Observation of long-lived interlayer excitons in monolayer $MoSe_2$–WSe_2 heterostructures," *Nature Communications*, vol. 6, p. 6242, Feb 2015. [Online]. Available: https://doi.org/10.1038%2Fncomms7242

[56] M.-Y. Li, Y. Shi, C.-C. Cheng, L.-S. Lu, Y.-C. Lin, H.-L. Tang, M.-L. Tsai, C.-W. Chu, K.-H. Wei, J.-H. He, W.-H. Chang, K. Suenaga, and L.-J. Li, "Epitaxial growth of a monolayer WSe_2-MoS_2 lateral p-n junction with an atomically sharp interface," *Science*, vol. 349, no. 6247, pp. 524–528, Jul 2015. [Online]. Available: https://doi.org/10.1126%2Fscience.aab4097

[57] A. K. Geim and I. V. Grigorieva, "Van der Waals heterostructures," *Nature*, vol. 499, no. 7459, pp. 419–425, Jul 2013. [Online]. Available: https://doi.org/10.1038%2Fnature12385

[58] W. J. Yu, Y. Liu, H. Zhou, A. Yin, Z. Li, Y. Huang, and X. Duan, "Highly efficient gate-tunable photocurrent generation in vertical heterostructures of layered materials," *Nature Nanotechnology*, vol. 8, no. 12, pp. 952–958, Oct 2013. [Online]. Available: https://doi.org/10.1038%2Fnnano.2013.219

[59] K. Roy, M. Padmanabhan, S. Goswami, T. P. Sai, G. Ramalingam, S. Raghavan, and A. Ghosh, "Graphene–MoS_2 hybrid structures for multifunctional photoresponsive memory

devices," *Nature Nanotechnology*, vol. 8, no. 11, pp. 826–830, Oct 2013. [Online]. Available: https://doi.org/10.1038%2Fnnano.2013.206

[60] X. Hong, J. Kim, S.-F. Shi, Y. Zhang, C. Jin, Y. Sun, S. Tongay, J. Wu, Y. Zhang, and F. Wang, "Ultrafast charge transfer in atomically thin MoS_2/WS_2 heterostructures," *Nature Nanotechnology*, vol. 9, no. 9, pp. 682–686, Aug 2014. [Online]. Available: https://doi.org/10.1038%2Fnnano.2014.167

[61] P. Rivera, K. L. Seyler, H. Yu, J. R. Schaibley, J. Yan, D. G. Mandrus, W. Yao, and X. Xu, "Valley-polarized exciton dynamics in a 2D semiconductor heterostructure," *Science*, vol. 351, no. 6274, pp. 688–691, Feb 2016. [Online]. Available: https://doi.org/10.1126%2Fscience.aac7820

[62] Y. Guo and J. Robertson, "Band engineering in transition metal dichalcogenides: Stacked versus lateral heterostructures," *Applied Physics Letters*, vol. 108, no. 23, p. 233104, Jun 2016. [Online]. Available: https://doi.org/10.1063%2F1.4953169

[63] C. Gong, H. Zhang, W. Wang, L. Colombo, R. M. Wallace, and K. Cho, "Band alignment of two-dimensional transition metal dichalcogenides: Application in tunnel field effect transistors," *Applied Physics Letters*, vol. 103, no. 5, p. 053513, Jul 2013. [Online]. Available: https://doi.org/10.1063%2F1.4817409

[64] J. Kang, S. Tongay, J. Zhou, J. Li, and J. Wu, "Band offsets and heterostructures of two-dimensional semiconductors," *Applied Physics Letters*, vol. 102, no. 1, p. 012111, Jan 2013. [Online]. Available: https://doi.org/10.1063%2F1.4774090

[65] M.-H. Chiu, C. Zhang, H.-W. Shiu, C.-P. Chuu, C.-H. Chen, C.-Y. S. Chang, C.-H. Chen, M.-Y. Chou, C.-K. Shih, and L.-J. Li, "Determination of band alignment in the single-layer MoS_2/WSe_2 heterojunction," *Nature Communications*, vol. 6, p. 7666, Jul 2015. [Online]. Available: https://doi.org/10.1038%2Fncomms8666

[66] C. Huang, S. Wu, A. M. Sanchez, J. J. P. Peters, R. Beanland, J. S. Ross, P. Rivera, W. Yao, D. H. Cobden, and X. Xu, "Lateral heterojunctions within monolayer $MoSe_2$–WSe_2 semiconductors," *Nature Materials*, vol. 13, no. 12, pp. 1096–1101, Aug 2014. [Online]. Available: https://doi.org/10.1038%2Fnmat4064

[67] Y. Gong, J. Lin, X. Wang, G. Shi, S. Lei, Z. Lin, X. Zou, G. Ye, R. Vajtai, B. I. Yakobson, H. Terrones, M. Terrones, B. K. Tay, J. Lou, S. T. Pantelides, Z. Liu, W. Zhou, and P. M. Ajayan, "Vertical and in-plane heterostructures from WS_2/MoS_2 monolayers," *Nature Materials*, vol. 13, no. 12, pp. 1135–1142, Sep 2014. [Online]. Available: https://doi.org/10.1038%2Fnmat4091

[68] Y. Gong, S. Lei, G. Ye, B. Li, Y. He, K. Keyshar, X. Zhang, Q. Wang, J. Lou, Z. Liu, R. Vajtai, W. Zhou, and P. M. Ajayan, "Two-step growth of two-dimensional WSe_2/$MoSe_2$ heterostructures," *Nano Letters*, vol. 15, no. 9, pp. 6135–6141, Sep 2015. [Online]. Available: https://doi.org/10.1021%2Facs.nanolett.5b02423

[69] X. Duan, C. Wang, J. C. Shaw, R. Cheng, Y. Chen, H. Li, X. Wu, Y. Tang, Q. Zhang, A. Pan, J. Jiang, R. Yu, Y. Huang, and X. Duan, "Lateral epitaxial growth of two-dimensional layered semiconductor heterojunctions," *Nature Nanotechnology*, vol. 9, no. 12, pp. 1024–1030, Sep 2014. [Online]. Available: https://doi.org/10.1038%2Fnnano.2014.222

[70] H. Heo, J. H. Sung, G. Jin, J.-H. Ahn, K. Kim, M.-J. Lee, S. Cha, H. Choi, and M.-H. Jo, "Rotation-misfit-free heteroepitaxial stacking and stitching growth of hexagonal transition-metal dichalcogenide monolayers by nucleation kinetics controls," *Advanced Materials*, vol. 27, no. 25, pp. 3803–3810, May 2015. [Online]. Available: https://doi.org/10.1002%2Fadma.201500846

[71] M. P. Levendorf, C.-J. Kim, L. Brown, P. Y. Huang, R. W. Havener, D. A. Muller, and J. Park, "Graphene and boron nitride lateral heterostructures for atomically thin

circuitry," *Nature*, vol. 488, no. 7413, pp. 627–632, Aug 2012. [Online]. Available: https://doi.org/10.1038%2Fnature11408

[72] H. Morkoc and S. N. Mohammad, "High-luminosity blue and blue-green gallium nitride light-emitting diodes," *Science*, vol. 267, no. 5194, pp. 51–55, Jan 1995. [Online]. Available: https://doi.org/10.1126%2Fscience.267.5194.51

[73] K. Y. Lau, "Dynamics of quantum well lasers," in *Quantum Well Lasers*. Elsevier BV, 1993. [Online]. Available: https://doi.org/10.1016%2Fb978-0-08-051558-8.50011-7

[74] T. Mimura, S. Hiyamizu, T. Fujii, and K. Nanbu, "A new field-effect transistor with selectively doped GaAs/n-al$_x$ Ga$_{1-x}$ as heterojunctions," *Japanese Journal of Applied Physics*, vol. 19, no. 5, pp. L225–L227, May 1980. [Online]. Available: https://doi.org/10.1143%2Fjjap.19.l225

[75] C.-H. Lee, G.-H. Lee, A. M. van der Zande, W. Chen, Y. Li, M. Han, X. Cui, G. Arefe, C. Nuckolls, T. F. Heinz, J. Guo, J. Hone, and P. Kim, "Atomically thin p–n junctions with van der Waals heterointerfaces," *Nature Nanotech*, vol. 9, no. 9, pp. 676–681, Aug 2014. [Online]. Available: http://dx.doi.org/10.1038/nnano.2014.150

[76] W. J. Yu, Z. Li, H. Zhou, Y. Chen, Y. Wang, Y. Huang, and X. Duan, "Vertically stacked multi-heterostructures of layered materials for logic transistors and complementary inverters," *Nature Materials*, vol. 12, no. 3, pp. 246–252, Dec 2012. [Online]. Available: https://doi.org/10.1038%2Fnmat3518

[77] M. Massicotte, P. Schmidt, F. Vialla, K. G. Schdler, A. Reserbat-Plantey, K. Watanabe, T. Taniguchi, K. J. Tielrooij, and F. H. L. Koppens, "Picosecond photoresponse in van der Waals heterostructures," *Nature Nanotechnology*, vol. 11, no. 1, pp. 42–46, Oct 2015. [Online]. Available: https://doi.org/10.1038%2Fnnano.2015.227

[78] F. Ceballos and H. Zhao, "Ultrafast laser spectroscopy of two-dimensional materials

beyond graphene," *Advanced Functional Materials*, p. 1604509, Dec 2016. [Online]. Available: https://doi.org/10.1002%2Fadfm.201604509

[79] O. B. Aslan, D. A. Chenet, A. M. van der Zande, J. C. Hone, and T. F. Heinz, "Linearly polarized excitons in single- and few-layer ReS_2 crystals," *ACS Photonics*, vol. 3, no. 1, pp. 96–101, Jan 2016. [Online]. Available: https://doi.org/10.1021%2Facsphotonics.5b00486

[80] F. Ceballos, Q. Cui, M. Z. Bellus, and H. Zhao, "Exciton formation in monolayer transition metal dichalcogenides," *Nanoscale*, vol. 8, no. 22, pp. 11 681–11 688, 2016. [Online]. Available: https://doi.org/10.1039%2Fc6nr02516a

[81] S. Schmitt-Rink, D. S. Chemla, and D. A. B. Miller, "Theory of transient excitonic optical nonlinearities in semiconductor quantum-well structures," *Physical Review B*, vol. 32, no. 10, pp. 6601–6609, Nov 1985. [Online]. Available: https://doi.org/10.1103%2Fphysrevb.32.6601

[82] R. W. Boyd, *Nonlinear Optics, Third Edition*, 3rd ed. Academic Press, 2008.

[83] J. Shah, *Ultrafast Spectroscopy of Semiconductors and Semiconductor Nanostructures*. Springer Berlin Heidelberg, 1996. [Online]. Available: https://doi.org/10.1007%2F978-3-662-03299-2

[84] Z. Nie, R. Long, L. Sun, C.-C. Huang, J. Zhang, Q. Xiong, D. W. Hewak, Z. Shen, O. V. Prezhdo, and Z.-H. Loh, "Ultrafast carrier thermalization and cooling dynamics in few-layer MoS_2," *ACS Nano*, vol. 8, no. 10, pp. 10 931–10 940, Oct 2014. [Online]. Available: https://doi.org/10.1021%2Fnn504760x

[85] C. Zhang, A. Johnson, C.-L. Hsu, L.-J. Li, and C.-K. Shih, "Direct imaging of band profile in single layer MoS_2 on graphite: Quasiparticle energy gap, metallic edge states, and edge band bending," *Nano Letters*, vol. 14, no. 5, pp. 2443–2447, May 2014. [Online]. Available: https://doi.org/10.1021%2Fnl501133c

[86] H.-L. Liu, C.-C. Shen, S.-H. Su, C.-L. Hsu, M.-Y. Li, and L.-J. Li, "Optical properties of monolayer transition metal dichalcogenides probed by spectroscopic ellipsometry," *Applied Physics Letters*, vol. 105, no. 20, p. 201905, Nov 2014. [Online]. Available: https://doi.org/10.1063%2F1.4901836

[87] H. M. Hill, A. F. Rigosi, C. Roquelet, A. Chernikov, T. C. Berkelbach, D. R. Reichman, M. S. Hybertsen, L. E. Brus, and T. F. Heinz, "Observation of excitonic rydberg states in monolayer MoS_2 and WS_2 by photoluminescence excitation spectroscopy," *Nano Letters*, vol. 15, no. 5, pp. 2992–2997, May 2015. [Online]. Available: https://doi.org/10.1021%2Fnl504868p

[88] B. Zhu, X. Chen, and X. Cui, "Exciton binding energy of monolayer WS_2," *Scientific Reports*, vol. 5, p. 9218, Mar 2015. [Online]. Available: https://doi.org/10.1038%2Fsrep09218

[89] M. M. Ugeda, A. J. Bradley, S.-F. Shi, F. H. da Jornada, Y. Zhang, D. Y. Qiu, W. Ruan, S.-K. Mo, Z. Hussain, Z.-X. Shen, F. Wang, S. G. Louie, and M. F. Crommie, "Giant bandgap renormalization and excitonic effects in a monolayer transition metal dichalcogenide semiconductor," *Nature Materials*, vol. 13, no. 12, pp. 1091–1095, Aug 2014. [Online]. Available: https://doi.org/10.1038%2Fnmat4061

[90] A. Thilagam, "Exciton formation assisted by longitudinal optical phonons in monolayer transition metal dichalcogenides," *Journal of Applied Physics*, vol. 120, no. 12, p. 124306, Sep 2016. [Online]. Available: https://doi.org/10.1063%2F1.4963123

[91] P. Steinleitner, P. Merkl, P. Nagler, J. Mornhinweg, C. Schller, T. Korn, A. Chernikov, and R. Huber, "Direct observation of ultrafast exciton formation in a monolayer of WSe_2," *Nano Letters*, vol. 17, no. 3, pp. 1455–1460, Feb 2017. [Online]. Available: https://doi.org/10.1021%2Facs.nanolett.6b04422

[92] A. Suna, "Kinematics of exciton-exciton annihilation in molecular crystals," *Physical*

Review B, vol. 1, no. 4, pp. 1716–1739, Feb 1970. [Online]. Available: https://doi.org/10.1103%2Fphysrevb.1.1716

[93] A. Kohler, J. Wilson, and R. Friend, "Fluorescence and phosphorescence in organic materials," *Advanced Materials*, vol. 14, no. 10, pp. 701–707, 2002. [Online]. Available: http://dx.doi.org/10.1002/1521-4095(20020517)14:10<701::AID-ADMA701>3.0.CO;2-4

[94] L. Ler, S. Hoseinkhani, D. Polli, J. Crochet, T. Hertel, and G. Lanzani, "Size and mobility of excitons in (6, 5) carbon nanotubes," *Nature Physics*, vol. 5, no. 1, pp. 54–58, Nov 2008. [Online]. Available: https://doi.org/10.1038%2Fnphys1149

[95] Y.-Z. Ma, L. Valkunas, S. L. Dexheimer, S. M. Bachilo, and G. R. Fleming, "Femtosecond spectroscopy of optical excitations in single-walled carbon nanotubes: Evidence for exciton-exciton annihilation," *Physical Review Letters*, vol. 94, no. 15, Apr 2005. [Online]. Available: https://doi.org/10.1103%2Fphysrevlett.94.157402

[96] N. Kumar, Q. Cui, F. Ceballos, D. He, Y. Wang, and H. Zhao, "Exciton-exciton annihilation in $MoSe_2$ monolayers," *Physical Review B*, vol. 89, no. 12, Mar 2014. [Online]. Available: https://doi.org/10.1103%2Fphysrevb.89.125427

[97] D. Sun, Y. Rao, G. A. Reider, G. Chen, Y. You, L. Brézin, A. R. Harutyunyan, and T. F. Heinz, "Observation of rapid exciton–exciton annihilation in monolayer molybdenum disulfide," *Nano Letters*, vol. 14, no. 10, pp. 5625–5629, Oct 2014. [Online]. Available: https://doi.org/10.1021%2Fnl5021975

[98] L. Yuan and L. Huang, "Exciton dynamics and annihilation in WS_2 2D semiconductors," *Nanoscale*, vol. 7, no. 16, pp. 7402–7408, 2015. [Online]. Available: https://doi.org/10.1039%2Fc5nr00383k

[99] C. Poellmann, P. Steinleitner, U. Leierseder, P. Nagler, G. Plechinger, M. Porer, R. Bratschitsch, C. Schller, T. Korn, and R. Huber, "Resonant internal quantum transitions

and femtosecond radiative decay of excitons in monolayer WSe_2," *Nature Materials*, vol. 14, no. 9, pp. 889–893, Jul 2015. [Online]. Available: https://doi.org/10.1038%2Fnmat4356

[100] H. Wang, C. Zhang, and F. Rana, "Ultrafast dynamics of defect-assisted electron–hole recombination in monolayer MoS_2," *Nano Letters*, vol. 15, no. 1, pp. 339–345, Jan 2015. [Online]. Available: https://doi.org/10.1021%2Fnl503636c

[101] H. Shi, R. Yan, S. Bertolazzi, J. Brivio, B. Gao, A. Kis, D. Jena, H. G. Xing, and L. Huang, "Exciton dynamics in suspended monolayer and few-layer MoS_2 2D crystals," *ACS Nano*, vol. 7, no. 2, pp. 1072–1080, 2012. [Online]. Available: http://dx.doi.org/10.1021/nn303973r

[102] N. Kumar, Q. Cui, F. Ceballos, D. He, Y. Wang, and H. Zhao, "Exciton diffusion in monolayer and bulk $MoSe_2$," *Nanoscale*, vol. 6, no. 9, p. 4915, 2014. [Online]. Available: https://doi.org/10.1039%2Fc3nr06863c

[103] T. Yan, X. Qiao, X. Liu, P. Tan, and X. Zhang, "Photoluminescence properties and exciton dynamics in monolayer WSe_2," *Applied Physics Letters*, vol. 105, no. 10, p. 101901, Sep 2014. [Online]. Available: https://doi.org/10.1063%2F1.4895471

[104] T. Korn, S. Heydrich, M. Hirmer, J. Schmutzler, and C. Schller, "Low-temperature photocarrier dynamics in monolayer MoS_2," *Applied Physics Letters*, vol. 99, no. 10, p. 102109, Sep 2011. [Online]. Available: https://doi.org/10.1063%2F1.3636402

[105] G. Moody, C. K. Dass, K. Hao, C.-H. Chen, L.-J. Li, A. Singh, K. Tran, G. Clark, X. Xu, G. Berghuser, E. Malic, A. Knorr, and X. Li, "Intrinsic homogeneous linewidth and broadening mechanisms of excitons in monolayer transition metal dichalcogenides," *Nature Communications*, vol. 6, p. 8315, Sep 2015. [Online]. Available: https://doi.org/10.1038%2Fncomms9315

[106] H. Wang, C. Zhang, W. Chan, C. Manolatou, S. Tiwari, and F. Rana, "Radiative lifetimes of excitons and trions in monolayers of the metal dichalcogenide MoS_2," *Physical Review*

B, vol. 93, no. 4, Jan 2016. [Online]. Available: https://doi.org/10.1103%2Fphysrevb.93.045407

[107] L. M. Smith, D. R. Wake, J. P. Wolfe, D. Levi, M. V. Klein, J. Klem, T. Henderson, and H. Morkoç, "Picosecond imaging of photoexcited carriers in quantum wells: Anomalous lateral confinement at high densities," *Physical Review B*, vol. 38, no. 8, pp. 5788–5791, Sep 1988. [Online]. Available: https://doi.org/10.1103%2Fphysrevb.38.5788

[108] J. He, D. He, Y. Wang, Q. Cui, M. Z. Bellus, H.-Y. Chiu, and H. Zhao, "Exceptional and anisotropic transport properties of photocarriers in black phosphorus," *ACS Nano*, vol. 9, no. 6, pp. 6436–6442, Jun 2015. [Online]. Available: https://doi.org/10.1021%2Facsnano.5b02104

[109] J. He, D. He, Y. Wang, Q. Cui, F. Ceballos, and H. Zhao, "Spatiotemporal dynamics of excitons in monolayer and bulk WS_2," *Nanoscale*, vol. 7, no. 21, pp. 9526–9531, 2015. [Online]. Available: https://doi.org/10.1039%2Fc5nr00188a

[110] Q. Cui, F. Ceballos, N. Kumar, and H. Zhao, "Transient absorption microscopy of monolayer and bulk WSe_2," *ACS Nano*, vol. 8, no. 3, pp. 2970–2976, Mar 2014. [Online]. Available: https://doi.org/10.1021%2Fnn500277y

[111] B. A. Ruzicka, S. Wang, L. K. Werake, B. Weintrub, K. P. Loh, and H. Zhao, "Hot carrier diffusion in graphene," *Physical Review B*, vol. 82, no. 19, Nov 2010. [Online]. Available: https://doi.org/10.1103%2Fphysrevb.82.195414

[112] R. Wang, B. A. Ruzicka, N. Kumar, M. Z. Bellus, H.-Y. Chiu, and H. Zhao, "Ultrafast and spatially resolved studies of charge carriers in atomically thin molybdenum disulfide," *Physical Review B*, vol. 86, no. 4, Jul 2012. [Online]. Available: https://doi.org/10.1103%2Fphysrevb.86.045406

[113] Q. Cui, J. He, M. Z. Bellus, M. Mirzokarimov, T. Hofmann, H.-Y. Chiu, M. Antonik, D. He, Y. Wang, and H. Zhao, "Transient absorption measurements on anisotropic

monolayer ReS_2," *Small*, vol. 11, no. 41, pp. 5565–5571, Aug 2015. [Online]. Available: https://doi.org/10.1002%2Fsmll.201501668

[114] Q. Cui, A. Lipatov, J. S. Wilt, M. Z. Bellus, X. C. Zeng, J. Wu, A. Sinitskii, and H. Zhao, "Time-resolved measurements of photocarrier dynamics in TiS_3 nanoribbons," *ACS Applied Materials & Interfaces*, vol. 8, no. 28, pp. 18 334–18 338, Jul 2016. [Online]. Available: https://doi.org/10.1021%2Facsami.6b04092

[115] H. Zhao, "Temperature dependence of ambipolar diffusion in silicon on insulator," *Applied Physics Letters*, vol. 92, no. 11, p. 112104, Mar 2008. [Online]. Available: https://doi.org/10.1063%2F1.2898711

[116] B. A. Ruzicka, L. K. Werake, H. Samassekou, and H. Zhao, "Ambipolar diffusion of photoexcited carriers in bulk GaAs," *Applied Physics Letters*, vol. 97, no. 26, p. 262119, Dec 2010. [Online]. Available: https://doi.org/10.1063%2F1.3533664

[117] V. O. zçelik, J. G. Azadani, C. Yang, S. J. Koester, and T. Low, "Band alignment of two-dimensional semiconductors for designing heterostructures with momentum space matching," *Physical Review B*, vol. 94, no. 3, Jul 2016. [Online]. Available: https://doi.org/10.1103%2Fphysrevb.94.035125

[118] S. J. Haigh, A. Gholinia, R. Jalil, S. Romani, L. Britnell, D. C. Elias, K. S. Novoselov, L. A. Ponomarenko, A. K. Geim, and R. Gorbachev, "Cross-sectional imaging of individual layers and buried interfaces of graphene-based heterostructures and superlattices," *Nature Materials*, vol. 11, no. 9, pp. 764–767, Jul 2012. [Online]. Available: http://dx.doi.org/10.1038/nmat3386

[119] P. S. Zory, *Quantum Well Lasers*. Elsevier BV, 1993. [Online]. Available: https://doi.org/10.1016%2Fb978-0-08-051558-8.50005-1

[120] H. Fang, C. Battaglia, C. Carraro, S. Nemsak, B. Ozdol, J. S. Kang, H. A. Bechtel, S. B. Desai, F. Kronast, A. A. Unal, G. Conti, C. Conlon, G. K. Palsson, M. C.

Martin, A. M. Minor, C. S. Fadley, E. Yablonovitch, R. Maboudian, and A. Javey, "Strong interlayer coupling in van der Waals heterostructures built from single-layer chalcogenides," *Proceedings of the National Academy of Sciences*, vol. 111, no. 17, pp. 6198–6202, Apr 2014. [Online]. Available: https://doi.org/10.1073%2Fpnas.1405435111

[121] P. Tonndorf, R. Schmidt, P. Bttger, X. Zhang, J. Brner, A. Liebig, M. Albrecht, C. Kloc, O. Gordan, D. R. T. Zahn, S. M. de Vasconcellos, and R. Bratschitsch, "Photoluminescence emission and raman response of monolayer MoS_2, $MoSe_2$, and WSe_2," *Optics Express*, vol. 21, no. 4, p. 4908, Feb 2013. [Online]. Available: https://doi.org/10.1364%2Foe.21.004908

[122] M. M. Furchi, A. Pospischil, F. Libisch, J. Burgdrfer, and T. Mueller, "Photovoltaic effect in an electrically tunable van der Waals heterojunction," *Nano Letters*, vol. 14, no. 8, pp. 4785–4791, Aug 2014. [Online]. Available: https://doi.org/10.1021%2Fnl501962c

[123] F. Ceballos, M. Z. Bellus, H.-Y. Chiu, and H. Zhao, "Probing charge transfer excitons in a $MoSe_2$–WS_2 van der Waals heterostructure," *Nanoscale*, vol. 7, no. 41, pp. 17 523–17 528, 2015. [Online]. Available: https://doi.org/10.1039%2Fc5nr04723d

[124] N. Peimyoo, J. Shang, C. Cong, X. Shen, X. Wu, E. K. L. Yeow, and T. Yu, "Nonblinking, intense two-dimensional light emitter: Monolayer WS_2 triangles," *ACS Nano*, vol. 7, no. 12, pp. 10 985–10 994, Dec 2013. [Online]. Available: https://doi.org/10.1021%2Fnn4046002

[125] W. Zhao, Z. Ghorannevis, L. Chu, M. Toh, C. Kloc, P.-H. Tan, and G. Eda, "Evolution of electronic structure in atomically thin sheets of WS_2 and WSe_2," *ACS Nano*, vol. 7, no. 1, pp. 791–797, Jan 2013. [Online]. Available: https://doi.org/10.1021%2Fnn305275h

[126] Z. Ye, T. Cao, K. O'Brien, H. Zhu, X. Yin, Y. Wang, S. G. Louie, and X. Zhang, "Probing excitonic dark states in single-layer tungsten disulphide," *Nature*, vol. 513, no. 7517, pp. 214–218, Aug 2014. [Online]. Available: https://doi.org/10.1038%2Fnature13734

[127] H. R. Gutiérrez, N. Perea-López, A. L. Elías, A. Berkdemir, B. Wang, R. Lv, F. López-Urías, V. H. Crespi, H. Terrones, and M. Terrones, "Extraordinary room-temperature photoluminescence in triangular WS_2 monolayers," *Nano Letters*, vol. 13, no. 8, pp. 3447–3454, Aug 2013. [Online]. Available: https://doi.org/10.1021%2Fnl3026357

[128] S. Tongay, J. Zhou, C. Ataca, K. Lo, T. S. Matthews, J. Li, J. C. Grossman, and J. Wu, "Thermally driven crossover from indirect toward direct bandgap in 2D semiconductors: $MoSe_2$ versus MoS_2," *Nano Letters*, vol. 12, no. 11, pp. 5576–5580, Nov 2012. [Online]. Available: https://doi.org/10.1021%2Fnl302584w

[129] Y. Yu, S. Hu, L. Su, L. Huang, Y. Liu, Z. Jin, A. A. Purezky, D. B. Geohegan, K. W. Kim, Y. Zhang, and L. Cao, "Equally efficient interlayer exciton relaxation and improved absorption in epitaxial and nonepitaxial MoS_2/WS_2 heterostructures," *Nano Letters*, vol. 15, no. 1, pp. 486–491, Jan 2015. [Online]. Available: https://doi.org/10.1021%2Fnl5038177

[130] S. Tongay, W. Fan, J. Kang, J. Park, U. Koldemir, J. Suh, D. S. Narang, K. Liu, J. Ji, J. Li, R. Sinclair, and J. Wu, "Tuning interlayer coupling in large-area heterostructures with CVD-grown MoS_2 and WS_2 monolayers," *Nano Letters*, vol. 14, no. 6, pp. 3185–3190, Jun 2014. [Online]. Available: https://doi.org/10.1021%2Fnl500515q

[131] J. Yuan, S. Najmaei, Z. Zhang, J. Zhang, S. Lei, P. M. Ajayan, B. I. Yakobson, and J. Lou, "Photoluminescence quenching and charge transfer in artificial heterostacks of monolayer transition metal dichalcogenides and few-layer black phosphorus," *ACS Nano*, vol. 9, no. 1, pp. 555–563, Jan 2015. [Online]. Available: https://doi.org/10.1021%2Fnn505809d

[132] M. Z. Bellus, F. Ceballos, H.-Y. Chiu, and H. Zhao, "Tightly bound trions in transition metal dichalcogenide heterostructures," *ACS Nano*, vol. 9, no. 6, pp. 6459–6464, Jun 2015. [Online]. Available: http://dx.doi.org/10.1021/acsnano.5b02144

[133] A. Azizi, S. Eichfeld, G. Geschwind, K. Zhang, B. Jiang, D. Mukherjee, L. Hossain, A. F. Piasecki, B. Kabius, J. A. Robinson, and N. Alem, "Freestanding van

der Waals heterostructures of graphene and transition metal dichalcogenides," *ACS Nano*, vol. 9, no. 5, pp. 4882–4890, May 2015. [Online]. Available: https://doi.org/10.1021%2Facsnano.5b01677

[134] J. He, N. Kumar, M. Z. Bellus, H.-Y. Chiu, D. He, Y. Wang, and H. Zhao, "Electron transfer and coupling in graphene–tungsten disulfide van der Waals heterostructures," *Nature Communications*, vol. 5, p. 5622, Nov 2014. [Online]. Available: https://doi.org/10.1038%2Fncomms6622

[135] X. Zhu, N. R. Monahan, Z. Gong, H. Zhu, K. W. Williams, and C. A. Nelson, "Charge transfer excitons at van der Waals interfaces," *Journal of the American Chemical Society*, vol. 137, no. 26, pp. 8313–8320, Jul 2015. [Online]. Available: https://doi.org/10.1021%2Fjacs.5b03141

[136] R. Long and O. V. Prezhdo, "Quantum coherence facilitates efficient charge separation at a MoS_2/$MoSe_2$ van der Waals junction," *Nano Letters*, vol. 16, no. 3, pp. 1996–2003, Mar 2016. [Online]. Available: https://doi.org/10.1021%2Facs.nanolett.5b05264

[137] H. Wang, J. Bang, Y. Sun, L. Liang, D. West, V. Meunier, and S. Zhang, "The role of collective motion in the ultrafast charge transfer in van der Waals heterostructures," *Nature Communications*, vol. 7, p. 11504, May 2016. [Online]. Available: https://doi.org/10.1038%2Fncomms11504

[138] F. Ceballos, M.-G. Ju, S. D. Lane, X. C. Zeng, and H. Zhao, "Highly efficient and anomalous charge transfer in van der Waals trilayer semiconductors," *Nano Letters*, Feb 2017. [Online]. Available: https://doi.org/10.1021%2Facs.nanolett.6b04815

[139] A. V. Akimov and O. V. Prezhdo, "Advanced capabilities of the PYXAID program: Integration schemes, decoherence effects, multiexcitonic states, and field-matter interaction," *Journal of Chemical Theory and Computation*, vol. 10, no. 2, pp. 789–804, Feb 2014. [Online]. Available: https://doi.org/10.1021%2Fct400934c

[140] ——, "The PYXAID program for non-adiabatic molecular dynamics in condensed matter systems," *Journal of Chemical Theory and Computation*, vol. 9, no. 11, pp. 4959–4972, Nov 2013. [Online]. Available: https://doi.org/10.1021%2Fct400641n

[141] Y. Li, A. Chernikov, X. Zhang, A. Rigosi, H. M. Hill, A. M. van der Zande, D. A. Chenet, E.-M. Shih, J. Hone, and T. F. Heinz, "Measurement of the optical dielectric function of monolayer transition-metal dichalcogenides: MoS_2, $MoSe_2$, WS_2, and WSe_2," *Physical Review B*, vol. 90, no. 20, Nov 2014. [Online]. Available: https://doi.org/10.1103%2Fphysrevb.90.205422

[142] A. F. Rigosi, H. M. Hill, Y. Li, A. Chernikov, and T. F. Heinz, "Probing interlayer interactions in transition metal dichalcogenide heterostructures by optical spectroscopy: MoS_2/WS_2 and $MoSe_2$/WSe_2," *Nano Letters*, vol. 15, no. 8, pp. 5033–5038, Aug 2015. [Online]. Available: https://doi.org/10.1021%2Facs.nanolett.5b01055

[143] M. Bernardi, M. Palummo, and J. C. Grossman, "Extraordinary sunlight absorption and one nanometer thick photovoltaics using two-dimensional monolayer materials," *Nano Letters*, vol. 13, no. 8, pp. 3664–3670, Aug 2013. [Online]. Available: https://doi.org/10.1021%2Fnl401544y

[144] A. Vasicek and H. Watney-Kaczer, *Optics of Thin Films*. Amsterdam, 1960.

Appendix A

Sample Fabrication

A.1 Sample Fabrication, Identification, and Annealing Treatment

The monolayers and the multilayer structures were fabricated by mechanically exfoliating TMD bulk crystals purchased from 2D Semiconductors using adhesive tape. A small fraction of the flakes on the tape are then transferred onto a polydimethylsiloxane (PDMS) substrate, for optical inspection, by placing the adhesive tape on it and then peeling it off. The PDMS substrate, already placed on top of a glass slide, is first inspected under a microscope. The monolayers can then be identified by their optical contrast, their photoluminescence, and absorption spectrum. Depending on the type of measurement being carried on the samples, each TMD monolayer was then manually transferred, using a micromanipulator and microscope, from the PDMS substrate onto either a silicon wafer covered with 90 nm of silicon dioxide or quartz substrate. The freshly transferred sample on the new substrate is then thermally annealed at 200 °C for 2 h under a H_2/Ar (20 sccm/100 sccm) environment at a pressure of about 3 Torr in order to clean its surface.

When forming multilayer heterostructures, additional different monolayers need to be fabricated. For example, in order to form a bilayer heterostructure, a new different layer is precisely placed on top of the layer already annealed first layer. The second transfer is more difficult than the first one, since usually, exfoliated monolayer samples are only a few micrometer in diameter in their largest dimension. If the transfer is successful, the newly formed bilayer heterostructure

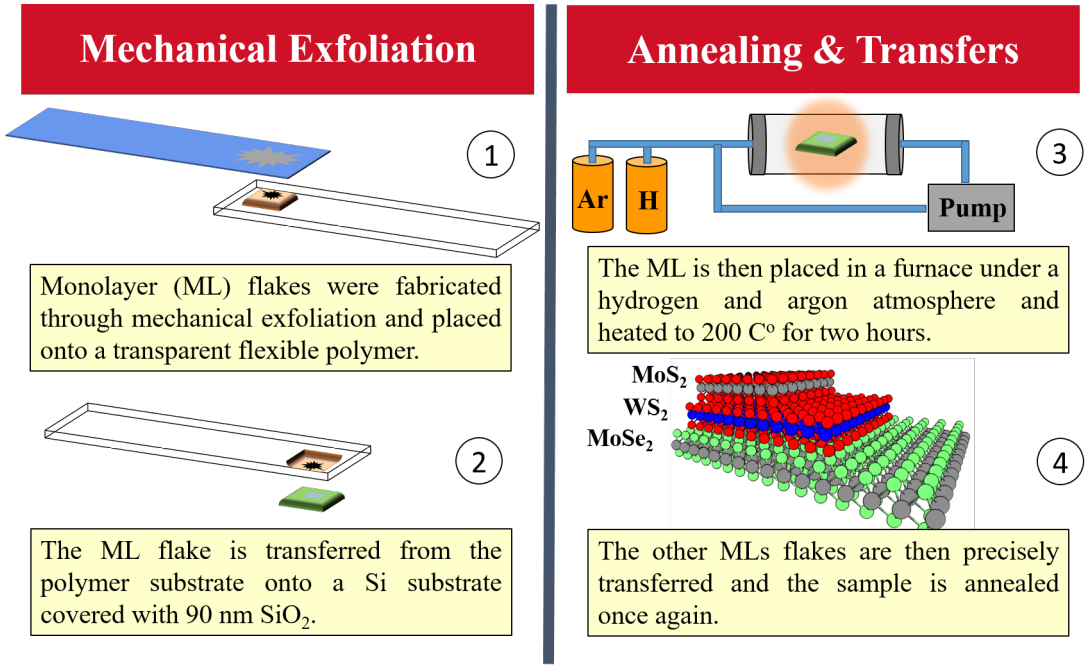

Figure A.1: Schematic of the multilayer sample preparation procedure.

is thermally annealed once more. This time, the annealing procedure cleans the surface of the top layer, the interface between the overlapping region of the two layers, and increases the coupling between the layers. Similarly, samples with three-layers or more are fabricated in the same fashion, with the precise transfer of a new monolayer followed by annealing of the newly formed multilayer sample.

Appendix B

Estimation of Photocarrier Density in Single and Multilayer Structures

B.1 Calculation of Photocarrier Density in Single Layer Materials

We will first calculate the photocarriers density injected when a pulsed beam with intensity I is normally incident on a single layer material. This discussion applies for both bulk and thin film materials. To calculate the injected carriers in each layer, the laser fluence, the energy per unit area each pulse delivers, must first be known. In these experiments, the Ti-sapphire laser generates Gaussian laser pulses at a frequency f_{rep} (Hz) known as the repetition rate of the laser. By measuring the time averaged power P and the repetition rate f_{rep}, the energy each pulse contains can be estimated by :

$$E_{\text{pulse}} = \frac{P}{f_{\text{rep}}}. \tag{B.1.1}$$

Before conducting the pump-probe experiments, the laser spot size was measured by precisely scanning the pump beam across the probe with the use of calibrated picomotors. By doing so, the convolution between the pump and probe beam spatial profiles was obtained. By nothing that the convolution between two Gaussian profiles, f and g, is also Gaussian with a variance equal to the sum of the original variances, the convoluted spatial profile is then fitted to a Gaussian curve from

which we obtained the full width at half maximum, w_{RT}. Since both beams have similar spatial Gaussian profiles, we can assume that the full width at half maximum (FWHM) of the pump, w_{pump}, to be

$$w_{\mathrm{pump}} = \frac{w_{\mathrm{RT}}}{\sqrt{2}}. \tag{B.1.2}$$

The fluence is position dependent. For laser beams with Gaussian profiles, it can be described as:

$$F(r) = F_{\mathrm{peak}} e^{-2r^2/w^2}, \tag{B.1.3}$$

where F_{peak} is the peak fluence, r is the radial distance from the center of the beam, w is the Gaussian beam radius at which the fluence drops to $1/e^2$ of its peak value. By integrating the fluence, $F(r)$, over all space, the energy delivered by each pulse is found to be:

$$E_{\mathrm{pulse}} = F_{\mathrm{peak}} \frac{\pi w^2}{2}, \tag{B.1.4}$$

and therefore

$$F_{\mathrm{peak}} = \frac{2E_{\mathrm{pulse}}}{\pi w^2}. \tag{B.1.5}$$

It can be shown that the FWHM, w_0, is related the width, w, of the Gaussian profile by

$$w = \frac{w_0}{\sqrt{2\ln 2}}. \tag{B.1.6}$$

By using equation B.1.6 and the measured quantities P, f_{rep}, and w_{pump}, equation B.1.5 can be rewritten as

$$F_{\mathrm{peak}} = \frac{8\ln 2}{\pi} \frac{P}{f_{\mathrm{rep}} w_{\mathrm{RT}}^2}. \tag{B.1.7}$$

Most of the time the quantity of interest is the injected carrier density and not the laser fluence. The peak fluence can be converted to the incident number of photons per unit area by diving it by the photon energy $h\nu$, where h is Planck's constant and ν the frequency of the laser (not to be

confused with the repetition rate f_{rep}). From the incident photons, only a fraction of them will be absorbed. By assuming that each photon absorbed creates an excited electron-hole pair, the injected carrier density can be modeled as

$$N = \frac{F_{\text{peak}}}{h\nu}\int_a^b e^{-\alpha z}dz = \frac{F_{\text{peak}}}{h\nu}(e^{-\alpha a} - e^{-\alpha b}). \tag{B.1.8}$$

Here, α is the absorption coefficient of the sample, z is the direction the beam is propagating, a the position where the layer begins, and b the end of the layer. For each ML, we used the α values reported[141] for the corresponding incident pump photon energy.

B.2 Calculation of Photocarrier Density in Multilayer Samples

In the case of multilayer structures, the number of incident photons per unit area is not the same for different layers since light reflects at the interfaces formed between dissimilar materials and is also absorbed by the layers. Therefore, in order to correctly calculate the injected carrier density in each layer, these effects need to be accounted for. Our analysis will be constraint for light that is normally incident on the sample, which is the case in our experiments.

B.2.1 Thin Film Sample on a Transparent Thick Substrate

Consider a normally incident monochromatic beam of light with wavelength λ incident on a semi-infinite homogenous thin film placed on a thick (infinite) transparent substrate. The thin film of thickness d is considered thin if $d \ll \lambda$. Our experiments usually are conducted with wavelengths greater than 400 nm and the 2D samples that we study are about 1 nm thick. Even if we stack together four different monolayers (MLs), the thickness of the multilayer sample is at most 4 nm; therefore, this condition is always met. For the purpose of illustration, we will depict the beam of light as being incident on the sample at an angle θ, but it is important to remember that the equations derived will be for a beam of light that is normally incident on the thin film.

When a beam of intensity I_0 is incident on a thin film placed on a thick substrate as shown in

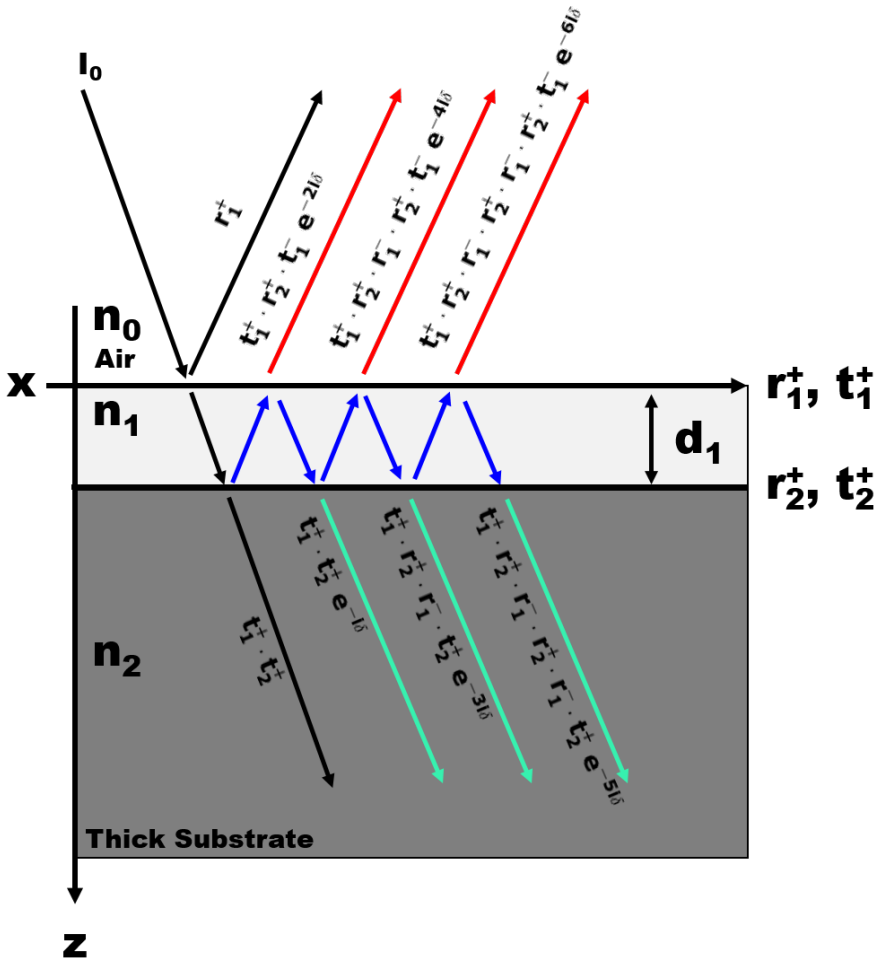

Figure B.1: Schematic of the multiple reflections that occur when light is incident on a thin film placed on a thick substrate.

Figure B.1, the incident beam of light reflects, refracts, and transmits at the first interface. Let us first consider the amount of light that is reflected back into the air in this system, (red arrows in Figure B.1). We define the positive z as the direction going into the thick substrate and the positive x direction to be parallel to the surface of the thin film, as shown in Figure B.1. The complex index of refraction of medium 0 and medium 1 will be denoted by $\tilde{n}_0$ and $\tilde{n}_1$. In our discussion, the complex index of refraction will equal $n - ik$, where the n is simply the index of refraction of the material and k is known as the extinction coefficient, which characterizes the amount of light a material absorbs. Just as the index of refraction of a material depends on the incident wavelength so does the extinction coefficient. For the sake of simplicity, we will continue our discussion by

assuming that the complex index of refraction is only real; however, the derived equations will remain valid and wont change form even when the index of refraction is complex. The index of refraction of air is denoted by the zero subscript, that of the thin film by the one subscript, and that of the thick substrate by the number three. To calculate the amount of light that gets reflected and transmitted on the different interfaces, we use Fresnel equations at normal incidence which give the Fresnel reflection and transmission coefficients between two different media. When light is normally incident from medium 0 to medium 1, the Fresnel coefficients are

$$r_1^+ = \frac{n_1 - n_0}{n_0 + n_1} \quad \& \quad t_1^+ = \frac{2n_0}{n_0 + n_1} \, . \tag{B.2.9}$$

Here, the positive sign in the superscript indicates the direction in which light is traveling. By definition, the positive z axis goes into the thick substrate. Fresnel equations when light is incident from medium 1 to medium 2 are

$$r_2^+ = \frac{n_2 - n_1}{n_1 + n_2} \quad \& \quad t_2^+ = \frac{2n_1}{n_1 + n_2} \, . \tag{B.2.10}$$

As indicated by the blue arrows in Figure B.1, the fraction of light that transmits into the thin film will experience an infinite number of reflections within the thin film. Each time the beam inside the thin film encounters either the first or the second interface, a portion of this beam will reflected and transmitted. For completion, we will note that when light is incident from medium 1 into medium 0, the Fresnel equations will be,

$$r_1^- = \frac{n_1 - n_0}{n_1 + n_2} \quad \& \quad t_1^- = \frac{2n_1}{n_1 + n_2} \, . \tag{B.2.11}$$

The negative sign on the subscript denotes that the light is traveling away from the thick substrate. By summing the total number of reflections that go into air from this system, we calculate the

amplitude reflection coefficient to be, noted by the red arrows in Figure B.1,

$$\begin{aligned} r^+ &= r_1^+ + t_1^+ \cdot r_2^+ \cdot t_1^- \cdot e^{-2i\delta} \\ &\quad + t_1^+ \cdot r_2^+ \cdot r_1^- \cdot r_2^+ \cdot t_1^- \cdot e^{-4i\delta} \\ &\quad + t_1^+ \cdot r_2^+ \cdot r_1^- \cdot r_2^+ \cdot r_1^- \cdot r_2^+ \cdot t_1^- \cdot e^{-6i\delta} \ ... \\ &= r_1^+ + r_2^+ t_1^+ t_1^- e^{-2i\delta} \sum_{n=0}^{\infty} (r_2^+ r_1^- e^{-2i\delta})^n \\ &= r_1^+ + \frac{r_2^+ t_1^+ t_1^- \ e^{-2i\delta}}{1 - r_2^+ r_1^- \ e^{-2i\delta}} \end{aligned} \tag{B.2.12}$$

This was done by first rearranging all the terms (except the first term) into an infinite sum and noting that the series is a geometric series. In equation B.2.12, a phase 2δ is acquired for every round trip light travels in the thin film of thickness d_1 where

$$\delta = \frac{2\pi}{\lambda} n_1 d_1. \tag{B.2.13}$$

Note that

$$t_1^+ t_1^- = 1 - r_1^{+2} \qquad \& \qquad r_1^- = -r_1^+ \tag{B.2.14}$$

so that the amplitude reflection coefficient, equation B.2.12 can be rewritten as

$$r^+ = \frac{r_1^+ + r_2^+ e^{-2i\delta}}{1 + r_2^+ r_1^+ e^{-2i\delta}} \ . \tag{B.2.15}$$

Similarly the amplitude of the transmission coefficient is

$$\begin{aligned} t^+ &= t_1^+ \cdot t_2^+ \cdot e^{-i\delta} + t_1^+ \cdot r_2^+ \cdot r_1^- \cdot t_2^+ \cdot e^{-3i\delta} \\ &\quad + t_1^+ \cdot r_2^+ \cdot r_1^- \cdot r_2^+ \cdot r_1^- \cdot t_2^+ \cdot e^{-5i\delta} + ... \end{aligned} \tag{B.2.16}$$

which can be reduce to

$$\begin{aligned} t^+ &= \frac{t_1^+ t_2^+ e^{-i\delta}}{1 - r_1^- r_2^+ e^{-2i\delta}} \\ &= \frac{t_1^+ t_2^+ e^{-i\delta}}{1 + r_1^+ r_2^+ e^{-2i\delta}} \end{aligned} \tag{B.2.17}$$

Finally, to calculate the intensity reflection and transmission coefficient (the reflectance and transmittance)

$$R = \frac{I_r}{I_0} = (r^+)^2 \qquad \& \qquad T = \frac{I_t}{I_0} = \frac{n_2}{n_0}(t^+)^2 \,, \tag{B.2.18}$$

where I_r and I_t are the reflected and transmitted intensities.

To calculate the intensity of the field that goes into the thin film, we simply calculate $(1-R)$. Therefore, the laser fluence that transmits into a thin film on a thick substrate is

$$F_{\text{peak}} = \frac{8\ln 2}{\pi} \frac{P}{f_{\text{rep}} w_{\text{RT}}^2} (1-R) \,. \tag{B.2.19}$$

Note that, we did not use T which is the intensity that gets transmitted into the thick substrate. For WS_2, MoS_2, WSe_2, and MoS_2 MLs, R is between 1-5% in the visible spectrum.

B.2.2 Multiple Thin Films on a Transparent Thick Substrate

If we now consider two thin films on a thick substrate, the analysis becomes more complicated. That is because an infinite number of reflections occur within each thin film. Each one of these reflections when they encounter an interface splits into two beams, a refracted and reflected beam. Figure B.2 depicts the reflections that occur in a two thin film system. It does not show the reflections in film 1 that transmit into the second thin film or the reflections in the second film that transmit into the first. However, these need to be taken into account in order to correctly calculate R and T.

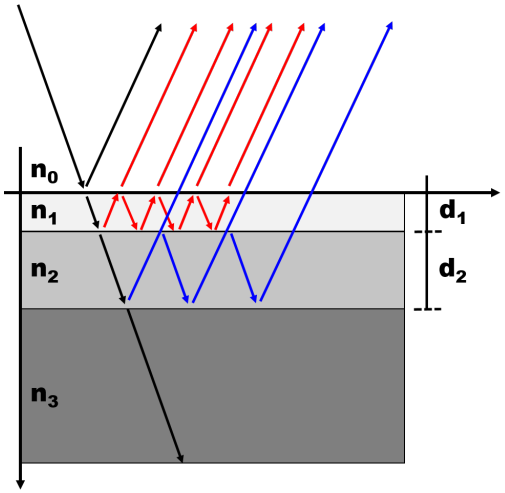

Figure B.2: Schematic of light being reflected from a two thin film system.

To calculate the reflection and transmission coefficients for a k thin film system, we used Rouard's method, where an iterative approach is implemented.[144] See Figure B.3 for schematic representation of light being reflected from a k thin film system. All the necessary notation required for this derivation is noted in that figure. We enumerate the parameters that characterize the k thin film system as follows:

- The index of refraction of air is denoted as n_0, the first thin film as n_1, the second thin film n_2, ..., the kth thin film n_k, and the thick substrate as n_{k+1}.

- The thickness of the first thin film is denoted as d_1, the second thin film d_2, ..., the kth thin film d_k.

- Path difference for a round trip in the first thin film is denoted as x_1, the second thin film x_2, ..., the kth thin film x_k. Here, the path difference is defined as $x_k = 2n_k d_k$.

- The Fresnel amplitude coefficients at the first boundary (between air and film 1) are denoted as r_1^+ and t_1^+, the second boundary (between film 1 and film 2) r_2^+ and t_2^+, ..., the kth boundary (between film $k-1$ and film k) r_k^+ and t_k^+, and the $k+1$ boundary (between film k and thick substrate) r_{k+1}^+ and t_{k+1}^+.

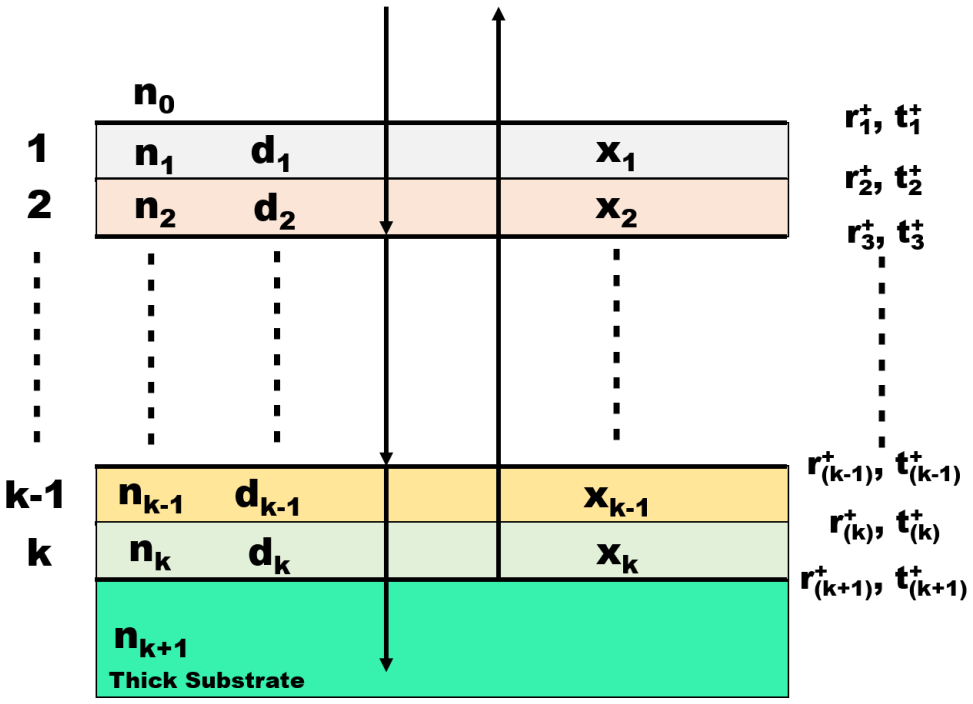

Figure B.3: Schematic of light being reflected from a k thin film system.

- The phase difference acquired for every round trip in film 1 is $\delta_1 = \frac{2\pi}{\lambda}x_1$, in film 2 this is $\delta_2 = \frac{2\pi}{\lambda}x_2$, ..., and in the kth film this is $\delta_k = \frac{2\pi}{\lambda}x_k$.

The concept behind Rouard's method, is to first consider only the kth thin film and the thick substrate and calculate the amplitude reflection and transmission coefficients using equation B.2.15 and B.2.17, respectively. This two complex numbers in polar form, $\bar{r}_k e^{i\bar{\delta}_k}$ and $\bar{t}_k e^{i\bar{\phi}_k}$, will describe the way light reflects and transmits when it is incident on the kth film and thick substrate. Rouard showed that the kth thin film system on the thick substrate is equivalent to one with the $k-1$ thin films plus the additional fictitious interface described by $\bar{r}_k e^{i\bar{\delta}_k}$ and $\bar{t}_k e^{i\bar{\phi}_k}$. Following this same logic, the $k-1$ thin film and the fictitious interface could be replace with new fictitious interface described by two new complex numbers. By continuing in this way, the kth thin film system can be reduced to one where the first thin film is place on top of the last emerging fictitious interface; therefore, allowing us to calculate the amplitude reflection and transmission coefficients r_k^+ and t_k^+ for the whole system.

We will first show how to obtain reflection amplitude r^+ for the kth thin film system. The

reflection from the last two interfaces r_k^+ and r_{k+1}^+, calculated using equation B.2.15, is

$$\bar{r}_k e^{i\bar{\delta}_k} = \frac{r_k^+ + r_{k+1}^+ e^{-i\delta_k}}{1 + r_k^+ r_{k+1}^+ e^{-i\delta_k}} \,. \tag{B.2.20}$$

To get the reflection from the $k-1$ interface and the new fictitious interface, described by equation B.2.20, we use again equation B.2.15 as follows

$$\bar{r}_{k-1} e^{i\bar{\delta}_{k-1}} = \frac{r_{k-1}^+ + \bar{r}_k e^{i\bar{\delta}_k} e^{-i\delta_{k-1}}}{1 + r_{k-1}^+ \bar{r}_k e^{i\bar{\delta}_k} e^{-i\delta_{k-1}}} \,. \tag{B.2.21}$$

We continue in this way, calculating the different reflection amplitude coefficients until we reach the first interface r_1^+. The reflection of light from the kth film system will then be

$$r^+ e^{i\delta} = \bar{r}_1 e^{i\bar{\delta}_1} = \frac{r_1^+ + \bar{r}_2 e^{i\bar{\delta}_2} e^{-i\delta_1}}{1 + r_1^+ \bar{r}_2 e^{i\bar{\delta}_2} e^{-i\delta_1}} \,. \tag{B.2.22}$$

To calculate the intensity reflection coefficient for the kth thin film system on a thick transparent substrate, equation B.2.22 is multiplied by its complex conjugate

$$R = (r^+ e^{i\delta}) \cdot (r^+ e^{i\delta})^* = (r^+ e^{i\delta}) \cdot (r^+ e^{-i\delta}) = (r^+)^2 \,. \tag{B.2.23}$$

The transmission coefficient t^+ for the kth thin film system is calculated with equation B.2.17 using the same train of logic. In the case none of the layers are absorbing, the intensity of light that transmits into the thick substrate and consequently into each thin film is $T = 1 - R$. To calculate the intensity absorbed by each thin film, we use the energy conservation relation $1 = T + R + A$, where T is the intensity that transmit through the kth thin film system, R the reflected intensity from the kth thin film system, and A the intensity absorbed by the k thin films. For example, for a 4-thin film system we calculate R and T from which A follows, as shown in Figure B.4. Therefore, we can determine the absorption from each film as follows:

- The intensity absorbed by thin film 1 will be $\Gamma_1 = A_4 - A_3$.

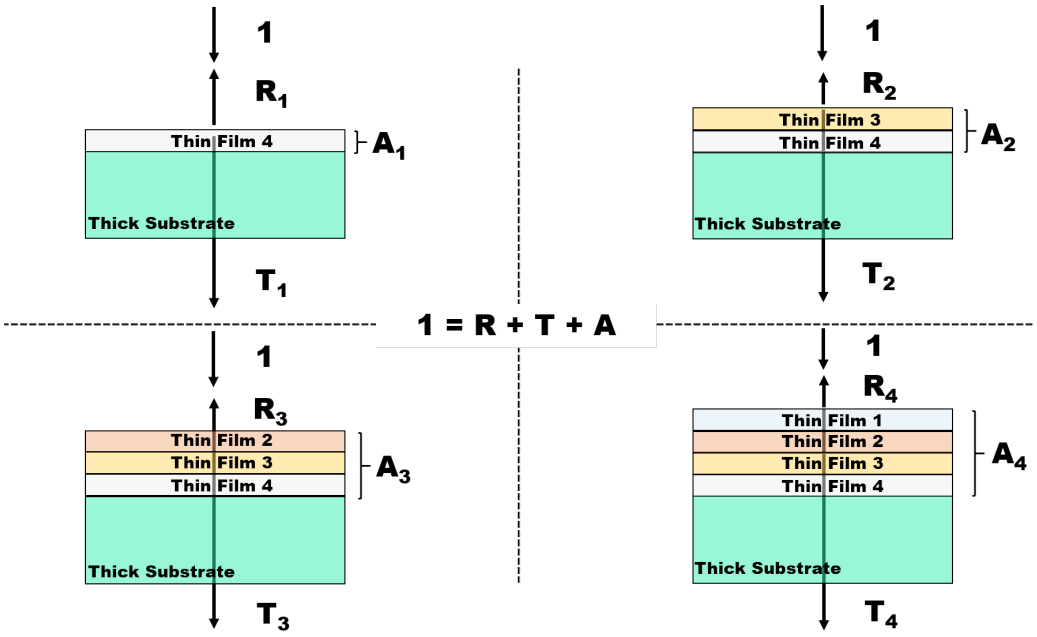

Figure B.4: Schematic of the calculations necessary to determined the fraction of absorbed intensity by each layer for a 4-layer thin film system.

- The intensity absorbed by thin film 2 will be $\Gamma_2 = A_3 - A_2$.
- The intensity absorbed by thin film 3 will be $\Gamma_3 = A_2 - A_1$.
- The intensity absorbed by thin film 4 will be $\Gamma_4 = A_1$.

Knowing all these, we can then calculate the intensity that transmits into each layer. For example, for a 4-layer thin film system the intensity at each layer is:

- The intensity on thin film 1 is $I_1 = 1 - R$, where R is the intensity reflected by the 4-layer thin film system.
- The intensity on thin film 2 is $I_2 = I_1 - \Gamma_1$, since Γ_1 is the amount of intensity absorbed by the first thin film.
- Similarly, the intensity on thin film 3 is $I_3 = I_2 - \Gamma_2$.
- The intensity on thin film 4 is $I_4 = I_3 - \Gamma_3$.
- Finally, the intensity that transmits into the thick substrate is $I_5 = I_4 - \Gamma_4$.

Notice, that I_n is simply the fraction of the intensity that gets transmitted into each layer and is a dimensionless number. Therefore, the injected photocarrier density on each layer is

$$N_i = \frac{F_{\text{peak}}}{h\nu} \cdot I_i \cdot \int_{a_i}^{b_i} e^{-\alpha_i z} dz = \frac{F_{\text{peak}} \cdot I_i}{h\nu} (e^{-\alpha_i a_i} - e^{-\alpha_i b_i}), \tag{B.2.24}$$

where i denotes the layer, $a_i = 0$, b_i is the thickness of the ith layer in cm, and α_i is the absorption coefficient of the ith layer in units of cm^{-1}.

Appendix C

Instrumental Response Time

The instrumental response time of our system determines the time resolution on which we carry out the experiments. Events that happen at a time scale shorter than our instrumental response time, can not be time-resolved. Since the dynamics of the photocarriers in the samples that we study happen in an ultrafast time scale, is important to understand the limitation of our instruments in order to interpret correctly the data collected.

To determine the instrumental response time, we utilize the the rising part from a differential reflection, $\Delta R/R_0$, signal obtained from monitoring the exciton population in a WSe_2 ML after a 2.00 eV pump pulse injects electron-hole pairs into it, black squares in Figure C.1. We assume that the response time of the sample is instantaneous. In the case that the pump and probe are infinitely narrow, the instrumental response would be a step function that jumps to its maximum value at zero delay. As the pump and probe pulses acquire a finite width, the response function evolves to one that quickly rises to its maximum value within the pulse width. To demonstrate this effect, the integral of a Gaussian function with different full widths at half maximum are shown as the solid curves in Figure C.1. From this it is clear that the pump-probe cross correlation width is 0.35 ps, red curve. That translates to pulse widths of 0.25 ps for each pulse, using 0.35/1.414. The sample response cannot be instantaneous, therefore, this is actually the upper limit of the pulse width.

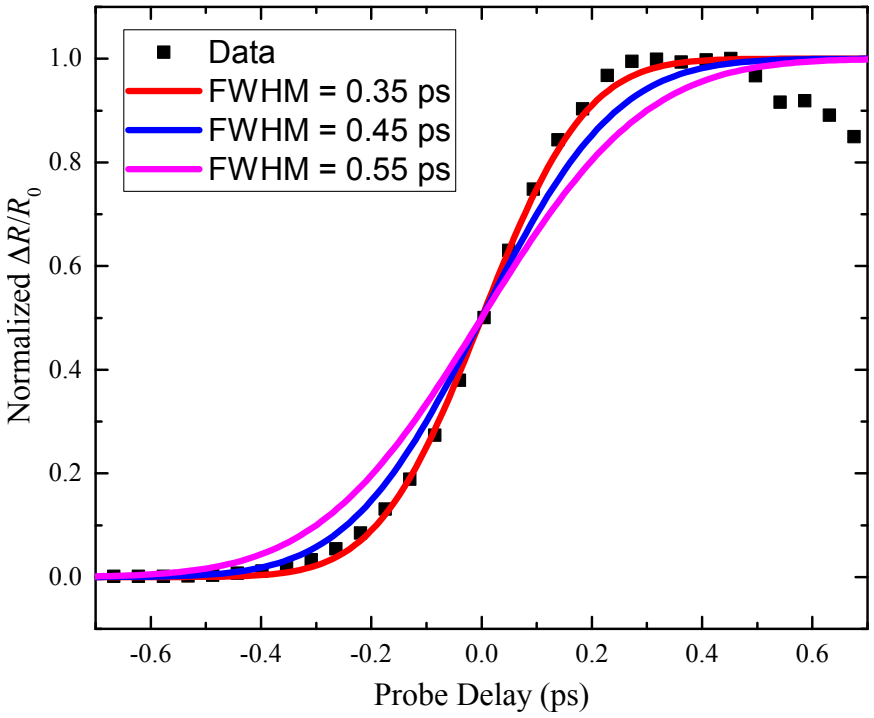

Figure C.1: Calculation of the pump–probe cross correlation function.